U.PORTO

FEUP FACULDADE DE ENGENHARIA
UNIVERSIDADE DO PORTO

Application of open-source software in the design of microfluidic devices for controlled deformation of biomolecules

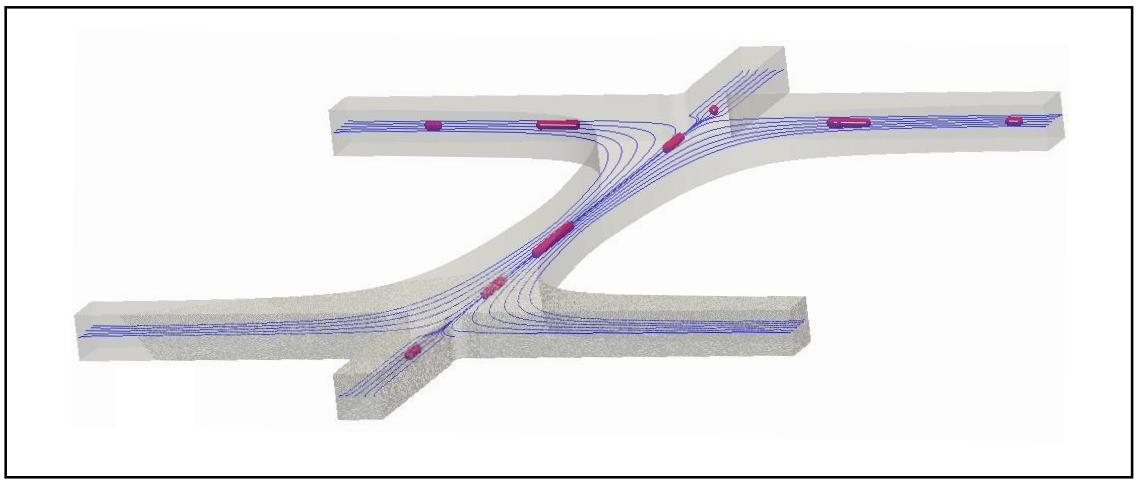

Dissertation for Master Degree in Bioengineering – Major in Biological Engineering

by

Francisco Manuel Pinheiro Pimenta

Supervisor: Dr Manuel António Moreira Alves
Co-supervisor: Dr Renato Luís Gomes de Sousa

Porto, June 2014

Dissertation submitted to obtain the Master degree in Bioengineering

Supervisor: _____

(Manuel Alves)

Co-supervisor: _____

(Renato Sousa)

Abstract

Microfluidic devices that are able to impose a strong extensional flow find application in molecular stretching, rheometry, rheological studies and cellular classification. However, a major drawback of classical devices is the heterogeneity of the extensional field generated, as well as the reduced length along which the extensional flow is imposed.

In the present work, the shape of a flow-focusing device was optimized in order to produce a homogeneous extensional flow field in a wide region. The fully-automatic numerical optimization routine was exclusively based on open-source software, namely: a mesh/geometry builder (Salome), a finite-volume solver (OpenFOAM) and a free-derivative direct search optimization algorithm (NOMAD). The optimization was tested for different velocity ratios between the lateral and central inlet streams (*VR*) and two distinct cost functions were analyzed. Furthermore, both two-dimensional (2D, corresponding to a channel with very high aspect ratio) and three-dimensional (3D) configurations were optimized. For 3D configurations, the optimization was tested for four aspect ratios (*AR* = 0.5, 1, 2 and 4), defined as the ratio between the inlet/outlet arms depth and their width. Devices with different optimized lengths in the region of constant extensional rate were also considered corresponding to 1, 2, 5 and 7 channel widths.

The optimized devices were able to impose a homogeneous extensional flow field for Reynolds number (*Re*) below 10 and *VR* > 5, both in 2D and 3D configurations. The simulated velocity profiles at the centerline were successfully validated through micro-Particle Image Velocimetry (μ-PIV) experiments for a set of selected geometries. Additionally, the numerically optimized shapes were also compared to the ones obtained through an analytical solution derived from the fully-developed velocity profile in a rectangular channel. The extensional flow was found to be more homogeneous for the numerically optimized devices.

Viscoelastic flow simulations were performed for a 2D optimized geometry using the Oldroyd-B constitutive model. The deformation rate plateau in the extensional region qualitatively remained unchanged for Weissenberg number (*We*) in the range 0.1–0.5, showing the potential use of the device as a micro-rheometer.

The applicability of the optimized devices to stretch macromolecules was also assessed through Brownian dynamics simulations, using λ-DNA as a model molecule, which was modeled as a worm-like chain (bead-spring model). Preliminary results show that the extension obtained in the optimized device is close to that achieved in a theoretical homogeneous flow

field, although dependent on the amount of Hencky strain imposed, which can be easily tuned varying *VR*. In addition, the advantage of a wide and homogeneous extensional region was demonstrated by comparing with the maximum stretch achieved in a standard (non-optimized) flow-focusing device.

Keywords: *microfluidics, flow-focusing device, homogeneous extension, shape optimization.*

Resumo

Os dispositivos microfluídicos que criam um escoamento com forte caráter extensional são aplicados no estiramento de moléculas, em reometria, em estudos reológicos e na classificação de células. Contudo, o escoamento extensional nos dispositivos standard não é homogéneo e encontra-se restrito a uma pequena área do escoamento.

Neste trabalho efetuou-se a otimização de dispositivos microfluídicos para focalização do escoamento (denominado na literatura inglesa por *Flow-focusing device*, FFD) que teve por objetivo aumentar a homogeneidade e a área do escoamento extensional no dispositivo. O processo automatizado de otimização numérica baseou-se exclusivamente em *software* de código-aberto: um gerador de geometria e malha (Salome), um algoritmo baseado na metodologia de volumes finitos para resolução do escoamento (OpenFOAM) e um algoritmo de otimização (NOMAD). A otimização foi testada para diferentes rácios de velocidade (*VR*) entre as correntes de entrada laterais e a corrente central, utilizando duas funções objetivo distintas. Adicionalmente, foram consideradas configurações bidimensionais (2D, correspondentes a um rácio muito elevado entre a profundidade e a largura do canal), bem como configurações tridimensionais (3D). Para as últimas, a otimização foi realizada a diferentes valores de rácio entre a profundidade e a largura do canal (*AR* = 0.5, 1, 2 e 4), considerando comprimentos distintos da área com escoamento extensional homogéneo correspondendo a 1, 2, 5 e 7 larguras do canal.

Os dispositivos otimizados apresentam um escoamento extensional homogéneo para números de Reynolds (*Re*) inferiores a 10 e $VR > 5$, nas configurações 2D e 3D. Os perfis de velocidade simulados ao longo do eixo central foram confirmados experimentalmente através da técnica ótica de *micro-Particle Image Velocimetry* (μ-PIV). Adicionalmente, realizou-se uma comparação entre os dispositivos otimizados numericamente e dispositivos cuja forma ideal resultou de uma expressão derivada a partir do perfil de velocidades em escoamento desenvolvido, num canal retangular. O escoamento extensional apresentou maior homogeneidade no caso dos dispositivos otimizados numericamente.

O comportamento dos dipositivos otimizados foi também testado em escoamentos de fluídos viscoelásticos, recorrendo ao modelo Oldroyd-B. O patamar da taxa de deformação manteve-se qualitativamente idêntico ao observado para os fluídos Newtonianos, na gama de números de Weissenberg (*We*) entre 0.1 e 0.5, demonstrando a potencial utilização dos dispositivos como micro-reómetros.

A aplicabilidade dos dispositivos otimizados para o estiramento de moléculas foi testada através de simulações de dinâmica Browniana, utilizando λ-ADN como modelo molecular, neste caso simulado através de um modelo de molas-esferas. A extensão molecular prevista no dispositivo otimizado revelou-se próxima daquela teoricamente prevista num campo extensional perfeitamente homogéneo, embora dependente da deformação acumulada, a qual é facilmente controlada no dispositivo através do parâmetro *VR*. Para além disso, as vantagens decorrentes de um campo extensional homogéneo e alargado foram demonstradas por comparação da extensão máxima conseguida nos dispositivos otimizados e num dispositivo standard (não otimizado).

Palavras-chave: *microfluídica, campo extensional homogéneo, otimização geométrica.*

Table of contents

List of figures

List of tables

List of symbols and abbreviations

Symbol	SI Unit	Description
A	m^2	Parameter of the exponential fit
b	$m.s^{-1}$	y-intercept of the linear regression
C	–	Constraints
f_{cost}	$m^2.s^{-2}$	Cost function
h	m	Channel height
K	–	Centerline to average velocity ratio
k_B	$m^2.kg.s^{-2}.K^{-1}$	Boltzmann constant
l	m	Optimized region length
L	m	Molecule length
L_0	m	Molecule length at equilibrium
L_C	m	Contour length
L_S	m	Maximum extension of a spring
m	s^{-1}	Slope of the linear regression
N_b	–	Number of beads
N_s	–	Number of springs
p	Pa	Pressure
Q	$m^3.s^{-1}$	Flow rate
r	m	Design point radius
r_b	m	Bead radius
T	K	Absolute temperature
t	s	Time
U	–	Normalized velocity
v	m^3	Excluded volume potential parameter
w	m	FFD channel width
w_c	m	Channel contraction width
w_d	m	Channel width downstream of the contraction
w_u	m	Channel width upstream of the contraction
Δt	s	Discrete Eulerian time-step

Greek symbols:

β	–	Solvent viscosity ratio
ε	–	Hencky/accumulated strain
$\dot{\varepsilon}$	s^{-1}	Deformation rate
$\dot{E}$	–	Normalized deformation rate
ζ	$kg.s^{-1}$	Drag coefficient
θ	rad	Design point angle
λ_p	m	Persistence length
μ	Pa.s	Dynamic shear viscosity
μ_e	Pa.s	Extensional viscosity
μ_p	Pa.s	Polymer viscosity
μ_s	Pa.s	Solvent viscosity
ξ	–	Flow type parameter
ρ	$kg.m^{-3}$	Fluid density
τ	s	Relaxation time
χ	m	Upper bound for design parameters
ψ	m	Lower bound for design parameters

Vectors and tensors:

$\mathbf{D}$	s^{-1}	Deformation rate tensor
$\mathbf{F}^B$	N	Brownian force
$\mathbf{F}^D$	N	Drag force
$\mathbf{F}^{EV}$	N	Excluded volume force
$\mathbf{F}^{HI}$	N	Hydrodynamic force
$\mathbf{f}_{ij}^S$	N	Spring force between beads *i* and *j*
$\mathbf{F}^S$	N	Total spring force on a bead
$\mathbf{S}$	–	Random vector
$\mathbf{u}$	$m.s^{-1}$	Velocity vector
$\mathbf{X}$	m	Inter-bead connection vector
$\mathbf{x}$	m	Spatial position vector
$\boldsymbol{\sigma}$	Pa	Extra-stress tensor
$\boldsymbol{\Omega}$	s^{-1}	Vorticity tensor

Dimensionless groups:

AR	–	Channel aspect ratio
De	–	Deborah number
El	–	Elasticity number
Re	–	Reynolds number
VR	–	Velocity ratio
We	–	Weissenberg number

Abbreviations	**Definition**
CaBER	Capillary Breakup Extensional Rheometer
DLA	Direct Linear Analysis
DNA	Deoxyribonucleic acid
FFD	Flow-Focusing Device(s)
FiSER	Filament Stretching Extensional Rheometer
MADS	Mesh Adaptive Direct Search
NOMAD	Nonlinear Optimization by Mesh Adaptive Direct Search (software)
PDMS	Polydimethylsiloxane
PIV	Particle Image Velocimetry
UCM	Upper-convected Maxwell

1 – Introduction

1.1 – Motivation and thesis outline

In the last years, microfluidics has attracted the attention of the scientific community from many diversified fields. Furthermore, this area of research has successfully evolved from academia to the industry, which is confirmed by the increasing number of commercial microfluidic-based applications and devices. Several factors contributed to this interest, among which the small volume of fluids required and the particular behavior (inertial, diffusive, elastic, …) of the flow at the micro-scale. Although not being an immature science front, microfluidics still faces many challenges, both at the experimental and theoretical levels. One important challenge is the increase of the effectiveness and efficiency of microfluidic devices by optimizing its design.

This work presents an optimization procedure applied to a standard microfluidic device aiming to produce a homogeneous extensional flow in an wide region, which finds applications in rheological studies, molecular stretching (at single-molecule level), cell mechanics studies, droplet deformation, among others. In addition to the design strategy, an application of the optimized device is also presented, as well the experimental confirmation of the simulation results.

In the remainder of the "Introduction" section, several microfluidic geometries that create an extensional flow are reviewed in the context of a specific application. This is followed by the description of some design optimization cases that were successfully applied to microfluidic devices. The section ends with the formulation of the problem addressed in this work.

The "Materials and Methods" section describes the set of computational and experimental techniques that were adopted in order to optimize and test the microfluidic device. The results that were obtained are presented in the "Results and discussion" section. Lastly, a brief conclusion is presented, which summarizes relevant results and the suggestions for further work.

1.2 – Microfluidic devices for extensional flow

In fluid mechanics there are two essential and opposite types of flows, from a rheological perspective: rotational and extensional flows. In between these two extremes, there are shear flows, Figure 1.1, which are also very important in rheometry.

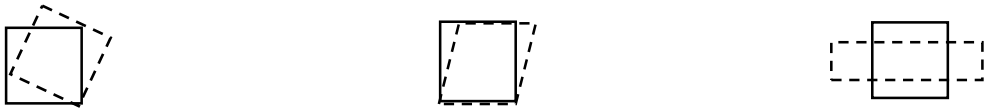

Rotational flow *Shear flow* *Extensional flow*

Figure 1.1 – 2D element of fluid in different types of flow (solid lines – initial form; dashed lines – final form).

The different types of flow arise as a consequence of velocity gradients. Indeed, an extensional flow exists when there is a velocity gradient in the direction of the flow, while shear flows occur when there is a velocity gradient normal to the flow direction, such as in a steady pipe flow, where the velocity gradient is primarily due to the fluid viscosity. In order to identify which type of flow is predominant in a given situation, the dimensionless flow-type parameter, ξ, can be used (Lee *et al*., 2007):

$$\xi = \frac{|\mathbf{D}| - |\mathbf{\Omega}|}{|\mathbf{D}| + |\mathbf{\Omega}|} \tag{1.1}$$

where $\mathbf{D} = \frac{1}{2}\left[\nabla\mathbf{u} + (\nabla\mathbf{u})^{\mathrm{T}}\right]$ is the deformation rate tensor (**u** is the velocity vector) and $\mathbf{\Omega} = \frac{1}{2}\left[\nabla\mathbf{u} - (\nabla\mathbf{u})^{\mathrm{T}}\right]$ is the vorticity tensor. A rotational flow is characterized by ξ = -1 (no extensional deformation, |**D**| = 0), while an extensional flow corresponds to ξ = +1 (no rotation, hence **D** is a traceless diagonal tensor).

The focus of the present work is on extension-dominated flows. This type of flow assumes a recognized importance when polymers and/or microscopic entities like cells are present. In joints, the synovial fluid (with a high concentration of hyaluronic acid) is compressed between both bones of the articulation in an extensional-like flow (Haward *et al*., 2013a). The blood circulation also has an important extensional component, for instance in stenosis structures (Tovar-Lopez *et al*., 2010). Moving to a completely different field, extensional flow plays a key role in jet pointers, which is reflected on the printing quality (Hoath *et al*., 2014). In addition, different microfluidic devices were specifically designed in order to produce extensional flows, with several purposes. Among them, three groups are distinguished and discussed in the following sections: devices for rheological studies, devices for molecular stretching and devices for the deformation of biological cells. Note that these groups are not mutually exclusive, since the same device may be suitable for multiple purposes.

1.2.1 – Rheological studies

The extensional viscosity is complementary to the shear viscosity when characterizing a material. However, the extensional viscosity is significantly more difficult to measure than shear viscosity. Some reasons may be pointed that support this fact: (1) difficulty in the generation of purely extensional flows; (2) dependence of the extensional viscosity on both strain rate and accumulated strain; (3) the low relaxation times (< 1 ms) of some dilute solutions requires an extremely high strain rate to be applied in order to effectively stretch the molecules ($We = \tau\dot{\varepsilon} > 0.5$, where *We* is the Weissenberg number, τ is the relaxation time of the fluid and $\dot{\varepsilon}$ the deformation rate), which usually increases inertial effects (Haward & McKinley, 2013b). Given these difficulties, microfluidic devices arise as a very promising solution for extensional rheometry.

Microfluidic devices that impose an extensional flow have been widely used in the rheological study of complex (non-Newtonian, namely viscoelastic) fluids. Such devices take the advantage of a high Elasticity number ($El = De/Re$, where *De* is the Deborah number and *Re* is the Reynolds number), which enhances the elastic behavior, while keeping a low Reynolds number flow, which minimizes inertial effects. Thus, fluids with a low viscosity and relaxation time may be characterized in these devices, which would be challenging in macroscale rheometers like the CaBER™ (Capillary Breakup Extensional Rheometer) or FiSER™ (Filament Stretching Extensional Rheometer) devices. Although the comparison between rheometers at different scales is out the scope of this work, it should be noted that devices like the CaBER™ and FiSER™ are able to produce an uniaxial extension with low shear due to the absence of solid surfaces in contact with fluid (the free surface may be, however, a source of instability, Minoshima & White, 1986), while the extension in microfluidic devices is planar (with few exceptions) and the wall shear cannot be neglected in most cases.

From a rheological perspective, two aspects may be accessed in extensional flows: the extensional viscosity (and its dependence on the deformation rate, $\dot{\varepsilon}$, and on the Hencky strain, $\varepsilon = \dot{\varepsilon}t$) and development of (inertio-)elastic instabilities. Some illustrative examples are briefly reviewed in the following paragraphs. It should be noted that these studies on extensional flows are used not only for experimental purposes, but also to test (verify) the predictive capacity of computational fluid models (see for instance, Schoonen *et al*., 1998).

Stagnation-point microfluidic devices were successfully used for the measurement of the extensional viscosity and in the study of flow instabilities. The cross-slot device, composed of two opposite incoming streams with two laterally opposed outlets normal to the inlet

channels, Figure 1.2(a), is able to retain molecules at its stagnation point (with zero velocity, but finite and non-zero strain rate, controlled by the flow rate) for a long time. This feature allows molecules to accumulate a high Hencky strain, which is linearly proportional to the time they remain at the stagnation point. Auhl *et al.* (2011) expressly took advantage of the high accumulated strain to evaluate the steady-state extensional behavior of polymer melts and to test the predictive capability of material models. However, a major drawback of this device is the reduced area where the strain rate is constant, which is nearly limited to one channel width (see for instance, Haward *et al*., 2012a). In order to circumvent this limitation, Alves (2008) used a numerical optimization procedure that increased the constant strain rate region to 7.5 channel widths, either side of the stagnation point, in a 2D cross-slot, Figure 1.2(b). More recently, the same process was extended to a 3D configuration of the cross-slot (Galindo-Rosales *et al.*, 2014). Haward *et al.* (2012b) tested the 2D shape-optimized cross-slot as an extensional rheometer for dilute polyethylene oxide solutions for deformation rates in the range 26–435 s^{-1}. Both the measurements of birefringence and pressure drop were self-consistent and in good agreement with theoretical models. The same optimized cross-slot was also used to investigate elastic instabilities, which are important to determine the operational limits of the device (Haward & McKinley, 2013b). Two major advantages of the optimized device are the wide region available to measurements and the reduction of the shear stress in the vicinity of the centerline due to a lubricating film of fluid in the corners of the device and to the increased distance of corners to the stagnation point. The standard (perpendicular channels) cross-slot was also used in the study of elastic instabilities of wormlike micellar solutions (Dubash *et al*., 2012; Haward *et al*., 2012a) and other complex fluids (Puangkird *et al*., 2009; Rocha *et al*., 2009; Schoonen *et al*., 1998), both using experimental and computational approaches. The shape of this device is particularly suitable to the study of elastic instabilities due to the flow curvature around its corners and to the large normal stress difference that is developed. Other stagnation-point devices exist, as the four-roll mill device, Figure 1.2(c), and T-junctions (a bifurcating channel), Figure 1.2(d). The four-roll mill device has the notable capacity to alternate between rotational, shear and extensional flows, through the simple control of the flow rates through its four inlets and four outlets, in the microfluidic configuration proposed by Lee *et al*. (2007).

Flow-focusing devices (FFD) have received less attention than cross-slot for rheological studies. These devices are similar to a cross-slot in the number and configuration of channels. However, while in the cross-slot there are two inlets and two outlet streams, in a

FFD there are three inlets and one outlet stream, Figure 1.2(e). This allows the compression and alignment of one stream due to the squeezing effect of the other two. Unlike in cross-slot devices, there is no stagnation point in a FFD and, consequently, the Hencky strain has a limited value, which depends on the flow rate ratio between the side and central streams ($\varepsilon = \ln(2VR + 1)$ for a FFD whose arms have the same width; VR is the side-to-central velocity ratio). Thus, steady-state elongation will only conditionally occur. Arratia *et al.* (2008) used a FFD to estimate the extensional viscosity of a dilute polymer solution based on the thinning of a (2D) filament. This method takes the advantage of reduced shear due to the lubricating effect of lateral streams, since two immiscible fluids were used in experiments, although the extensional region is still restricted to about one channel width. Oliveira *et al.* (2009) computationally studied the development of purely elastic instabilities in a FFD. To the best knowledge of the author, no optimization procedure was explicitly applied on this device in order to increase its performance for rheological studies. The major shape modifications performed on this geometry were made in the context of droplet generation, a field where FFD are widely used (Chae *et al*., 2009; Roberts *et al*., 2012; Teh *et al*., 2008).

The last class of microfluidic devices reviewed in this section includes contraction /expansion microchannels. As depicted in Figure 1.2(f), these devices comprise a straight channel with a contraction that is responsible for the fluid acceleration in the flow direction. This contraction can assume several shapes and it may be followed by an abrupt or smooth expansion (which may be linked through a straight channel region, as in Oliveira *et al*., 2008). The extensional deformation profile depends both on the flow rate and on the contraction shape (Sousa *et al*., 2011). The accumulated (Hencky) strain is related with the aperture of the contraction relative to the upstream channel width: $\varepsilon = \ln(w_u/w_c)$, where w_u is the upstream channel width and w_c is the contraction width. Hyperbolic contractions were specifically designed (based on the simple proposition that if the contraction cross-sectional area decreases inversely proportional to the axial position, then the extension rate will be constant, Ober *et al*., 2013, although some deviation was observed due to shear effects at the walls) to achieve a constant strain rate profile (Campo-Deaño *et al*., 2011; Ober *et al*., 2013). Such hyperbolic contractions were reasonably accurate as extensional rheometers up to extensional rates of 10^3 s^{-1}, when combined with optical (birefringence) and pressure drop measurements (Ober *et al*., 2013). However, the imposition of a high Hencky strain requires a large difference between the contraction and upstream channel widths, which may be problematic for standard PDMS (polydimethylsiloxane) devices (in Ober *et al*., 2013 the Hencky strain was only $\varepsilon = 2$, for a

width ratio of 7.4). A slightly different application for hyperbolic contractions was found by Campo-Deaño *et al*. (2011), allowing to the measurement of the relaxation time of Boger fluids based on the self-similar vortex growth upstream the contraction for different viscoelastic fluids. Sousa *et al.* (2011) have demonstrated the importance of extensional rheology of blood analogues, validating their flow through differently shaped microcontractions. As in cross-slot and FFD, elastic instabilities were also analyzed in contraction/expansion devices (Oliveira *et al*., 2008).

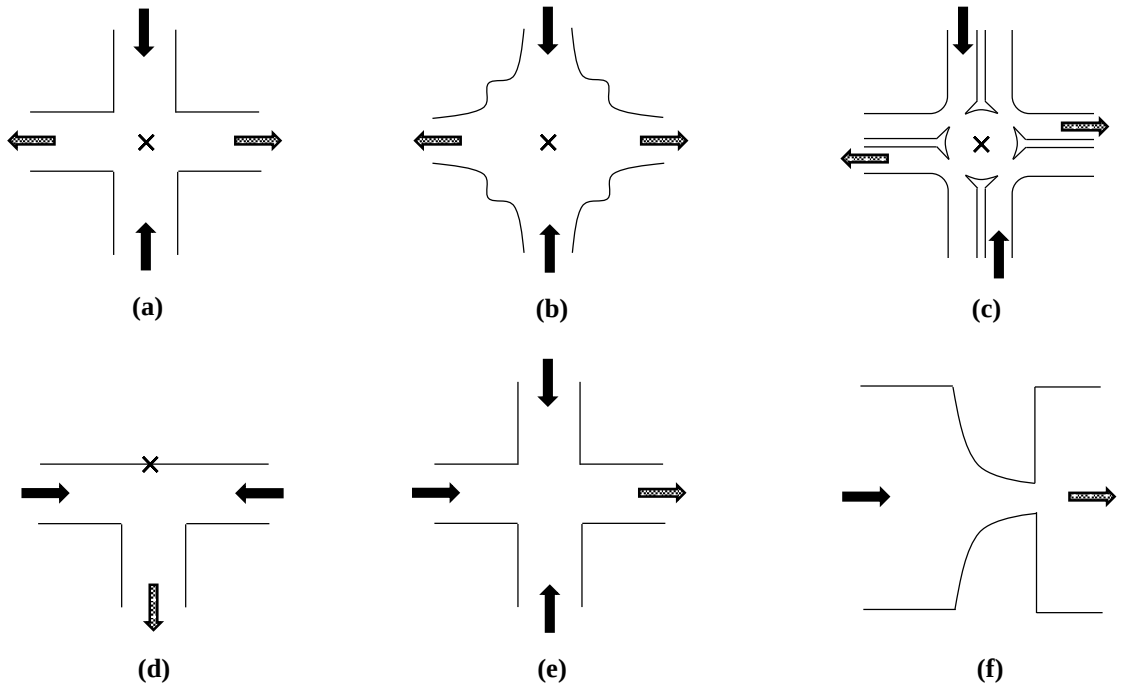

Figure 1.2 – Schematic representation (top view) of microfluidic devices applied in the study of rheological properties of complex fluids in extension-dominated flows: (a) – standard cross-slot; (b) – optimized cross-slot (Alves, 2008); (c) – four-roll mill device (Lee *et al.*, 2007); (d) – T-junction; (e) – flow-focusing device; (f) – contraction/expansion. In devices (a)-(d), the cross locates the stagnation point.

Based on the previous discussion on microfluidic devices suitable for rheological studies in extension-dominated flows, some relevant characteristics of such an idealized device are identified: (1) produce a homogeneous extensional flow (shear-free), which should be *Re* (inertia) independent; (2) keep the deformation rate constant over an extended region, suitable for measurements using optical techniques; (3) able to analyze fluids in a wide range of viscosities and relaxation times (mostly critical for low viscosity fluids); (4) easily control the deformation rate and Hencky strain; (5) easy fabrication and operation, at a low-cost.

The reader interested on extensional micro-rheometers is directed to recent reviews on this subject (Galindo-Rosales *et al.*, 2013; Pipe & McKinley, 2009).

1.2.2 – Stretching of macromolecules (single-molecule level)

The molecular stretching performed by extensional flows finds several applications other than pure rheological studies, which are briefly discussed in this section. Without surprise, microfluidic devices employed in these types of applications are very similar to those discussed previously.

Chan *et al.* (2004) proposed the DLA (Direct Linear Analysis) method to rapidly accomplish the mapping of DNA (Deoxyribonucleic acid) molecules. This technology, actually traded by PathoGenetix^{TM}, is based on DNA labeling by fluorescent markers, which bind to specific sites of the molecule where a given base pair sequence exists. The result is a barcode like pattern that is specie-dependent and that allows (fast) microbial genotyping without nucleotide sequencing. In order to guarantee the method reproducibility, DNA molecules must be probed in a stretched state (Chan *et al.*, 2004). This task was accomplished, in the original configuration (Chan *et al.*, 2004), by an array of obstacles followed by a microfluidic contraction to impose an extensional and confined (1 μm deep channels) flow that unraveled DNA molecules. A subsequent study was published by the same group where several configurations were tested for the microcontraction (Larson *et al.*, 2006). The geometries which imposed a constant deformation rate and linear increasing deformation rate gave the best results, since they were able to deliver a DNA population in a highly stretched state (averaged extension up to 87 % of λ-DNA contour length, although for $De > 50$), with a relatively low dispersion in the length distribution function. The DNA stretching device was further modified by the same group to a microcontraction followed by a FFD fused with another microcontraction (Krogmeier *et al.*, 2007). It should be noted that in applications such as DLA and general sequencing techniques, the throughput of the method is of high concern.

A DLA-related DNA mapping was investigated by Dylla-Spears *et al.* (2009). In this method, a standard cross-slot device is used to trap DNA molecules previously mixed with sequence-specific markers. The molecular extension has shown to be a critical factor in the accuracy and resolution of the method, since the markers position (and inter-markers distance) is not fixed between different assays unless DNA molecules keep their full extension. In this way, the cross-slot device is even more suitable than the microcontraction in DLA, since it potentially allows a steady stretched state due to its stagnation point. Indeed, the method resolution was higher than that reported in DLA and the same degree of extension was achieved at a lower *De* (88 % of λ-DNA contour length, at $De = 3.9$) (Dylla-Spears *et al.*, 2009). However, the stagnation point also represents a throughput decrease.

The theoretical background in the design of techniques for molecular stretching, as in the two cited examples, is primarily based on single-molecule studies. Such studies aim to explore the molecular behavior in diversified flow conditions. Extensional flows are of great importance for this purpose. Cross-slot devices (Hsieh *et al.*, 2007; Perkins *et al*., 1997; Schroeder *et al*., 2003; Smith & Chu, 1998), FFD (Wong *et al.*, 2003), T-junctions (Tang & Doyle, 2007) and contraction/expansion devices (Chuncheng & Qianqian, 2009; Hsieh *et al.*, 2011; Huang *et al.*, 2014; Randall *et al*., 2006) were used both in experimental and theoretical studies. It should be noted that, due to the electric charge of DNA molecules, the motion force may be provided by an electrical field, as well by an imposed pressure gradient. The former has proved to be especially advantageous over the second owing to the symmetry of the velocity gradient (hence, with irrotational components even near the walls) and to the quadratic decay of field disturbances (Randall & Doyle, 2005).

A note about DNA stretching techniques should be made at this point. There are several other methods, in addition to extensional flow devices, to stretch individual molecules: optical tweezers (Wang *et al*., 1997), flow past an array of obstacles (Teclemariam *et al*., 2007), oscillatory flow fields (Jo *et al*., 2009), flow past tethered DNA (Ferree & Blanch, 2003), thermo-electrophoresis (Hsieh *et al*., 2013) and functionalized surfaces (Liu *et al.*, 2014). However, throughput, among other aspects, is generally an issue in these methods, although this obviously will depend on the specific application.

As in the previous section, the discussion about microfluidic devices that aim to stretch DNA in extensional flows ends with the idealized characteristics of such a device intended to deliver stretched DNA to a downstream analytical process. The characteristics are the same as those mentioned in the previous section, to which it should be added the ability to achieve high throughputs. Note that, while for rheological studies it is important to generate pure extensional flows, for DNA stretching this condition is not so strict. The only requirement is the delivery of a homogeneously stretched population of DNA molecules to ensure the reproducibility of the analytical procedure that follows the stretching event. However, since the presence of shear forces may increase the dispersion of stretched states (Larson *et al*., 2006), then homogeneous extensional flows are also desirable in such applications.

1.2.3 – Other applications

Extensional flows are also of interest in the study of mechanical properties of biological cells. Yaginuma *et al.* (2013) assessed the rigidity of red blood cells in a hyperbolic

contraction device, highlighting its potential for diagnosis purposes. Also inspired on cell deformability, Gosset *et al.* (2012) proposed a mechanical phenotyping technique that includes a stagnation point geometry. More precisely, biological cells are focused and directed to a cross-slot device, where they are imaged in a stretched state. This technique proved to be able to distinguish between healthy and cancerous cells based on the differences of extensibility.

1.3 –Optimization of microfluidic devices

An optimization problem may be conceptually formulated as a problem where the objective is to find the set of parameters $r = \{r_1, ..., r_n\}$, eventually delimited between a lower $\psi = \{ \psi_1, ..., \psi_n\}$ and upper bound $\chi = \{ \chi_1, ..., \chi_n\}$ – box constraints –, that minimizes, global or locally, a cost function $f_{cost}(r_1, ..., r_n)$, subjected to a set of linear/non-linear $C(r)$ constraints:

$$\min(f_{cost}(r_1,...,r_n)) \ : C_1(r) \le k_1 \wedge ... \wedge C_m(r) \le k_m \ , \{\psi_1,...,\psi_n\} \le \{r_1,...,r_n\} \le \{\chi_1,...,\chi_n\} \quad (1.2)$$

There are several algorithms that could be used to find the optimal solution of the problem and it is common to distinguish between gradient-based methods and free-derivative methods. Gradient-based methods rely on the direct computation (analytical or numerically) of the derivative (first and/or higher order) of the cost function, since it is well known that the derivative of a function at a minimum is zero (applied, for instance, in Newton's method) and, also, that the derivative/gradient of a function points to the direction of maximal change (applied, for instance, in the gradient descent method). However, the cost function is not always continuously differentiable and computing its derivative could be expensive, complex or inaccurate (due to noise) in real engineering problems. Free-derivative algorithms arise as a robust alternative for these situations, though at the cost of a slower convergence to the optimal solution.

Rios & Sahinidis (2013) further classified free-derivative algorithms with respect to three criteria: direct *vs.* model-based; local *vs.* global; stochastic *vs.* deterministic. Direct methods perform a sampling procedure of the cost function at a given set of points, which are updated in the next iteration after defining the searching direction and the step length. On the other side, model-based methods evaluate the cost function in order to adjust a simple, but accurate model (usually a second-order polynomial) to the cost function. This allows the computation of the searching direction from the model. The difference between local and global methods is based on its capacity to escape local minima and the classification of a method as deterministic or stochastic depends on the respective randomness. In brief, these methods differ in the way they use the current set of design parameters to generate the next guess and it is not

possible to point the best algorithm, since it will always depend on the specific problem. The reader interested on free-derivative optimization algorithms, as well on their implementation on available software and relative performance, is directed to Kramer *et al.* (2011), Moré & Wild (2009) and Rios & Sahinidis (2013).

From a practical perspective, optimization routines are of common practice in fluid and solid dynamics processes. A classical and well-known problem is the drag reduction of vehicles through shape modifications, as an attempt to decrease the fuel consumption (Muyl *et al.*, 2004; Song *et al.*, 2012). Of particular importance for the present work is the optimization of microfluidic devices and illustrative examples of such cases are presented in what follows.

Mixing two or more fluids at the micro-scale is a great challenge, since low *Re* flows avoid turbulence effects that promote the mixing of fluids. Shuttleworth *et al.* (2011) addressed this problem through the shape optimization of a set of electrically conductive posts in an induced charge electro-osmosis process. The asymmetric vortex structures that arise near posts, due to the charge balance in the respective double layer, increase the interfacial area between fluids. Thus, a good inter-dispersion of fluids was achieved without diluting the mixture, since the device can operate as a static mixer, with a constant volume of fluid. The optimization routine was performed with a parallel free-derivative direct local search algorithm that directly sampled the cost function (level of heterogeneity in the mixture concentration) according to a direction and step length, as explained previously for direct methods. In this case, the design parameters controlled both the shape and location of posts.

The work of Ivorra *et al.* (2006) was related with the same mixing phenomena. More specifically, the authors aimed to minimize the mixing time of a protein solution in a FFD, since this is crucial in the study of fast folding events that occur with these biomolecules. The objective – minimization of the mixing time – was accomplished through the parameterization of the FFD corners (shape optimization). Two algorithms were tested by the authors, namely a stochastic genetic algorithm and a semi-deterministic algorithm, where the gradient of the cost function was computed based on the physical equations. The mixing time was successfully decreased to less than 50 % of its initial value.

In section 1.2.1, a reference was made to an optimized cross-slot device designed by Alves (2008), Figure 1.2(b), which has a wider region of constant deformation rate. The optimization was also performed at the parameterized corner of the device and a free-derivative local model-based search algorithm was employed to find a minimum of the cost function.

A different approach was presented by Jensen *et al*. (2012) who designed a microfluidic viscoelastic rectifier using topological optimization. This method attributes to each cell in the computational domain a coefficient that represents a virtual porosity. Depending on the porosity value, a cell may behave as a void, with fluid flow, or as a solid, with nearly no-slip conditions. The porosity coefficient is incorporated in the Navier-Stokes equations and a posterior sensitivity analysis (gradient-based) identifies the contribution of each cell to the minimization of the cost function. As a result, the optimization is applied on the whole computational domain, so that the number of design variables depends on the level of discretization of the initial geometry, in the region to be optimized.

1.4 – Problem formulation

At this point, it is clear that the same microfluidic device may be suitable for several applications, although there is not a device that performs ideally in all applications. Flow-focusing devices are particularly interesting from this perspective. Indeed, these devices meet almost all the idealized characteristics enumerated for the two applications previously described. Furthermore, the throughput is higher than in stagnation point devices (although at the cost of a lower Hencky strain) and higher Hencky strains are more easily reached/controlled than in contraction/expansion devices. Still, a major drawback of standard FFD is their limited region of extensional flow, which is not perfectly homogeneous.

In order to solve this problem, a design optimization can be used. This task could be accomplished based on the same approach as in Ober *et al*. (2013) applied to a contraction/expansion geometry (see section 1.2.1). Nevertheless, entry effects are important when the geometry becomes abrupt and this reason may explain the non-ideal behavior observed by Ober *et al*. (2013). A more robust approach would be a numerical shape optimization, as in Alves (2008), and this was in fact the strategy adopted for this work. Topological optimization would also be a valid alternative and it is left as a suggestion for a future work. For the solution of this problem, another challenge was set: to use only open-source software. Although this was not a major goal, it demonstrates that the type of approach here presented is free of costs in what concerns software licensing.

In the next section, the strategy adopted is explained, as well as the experimental procedure to validate the simulated results of the final optimized shape. Additionally, Brownian dynamics simulations were performed to evaluate the potential of the optimized devices in the extension of DNA molecules and the model employed is also described in the next section.

Before proceeding further, a citation of Binding & Walters (1988) is here reproduced about the task of designing devices for pure extensional flows: "Generating a purely extensional flow in the case of mobile liquids is virtually impossible. The most that one can hope to do is to generate flows with a high extensional component and to interpret the data in a way which (hopefully) captures that extensional component in a convenient and consistent way through a suitably defined extensional viscosity and strain rate. The philosophy is not without its difficulties and is somewhat controversial. However, given the practical importance of the subject and the expectation that there will be at least semi-quantitative predictive capacity, it is our contention that the pursuit is eminently worthwhile, especially since there is no alternative if one requires some indication of the extensional viscosity levels in the flow of non-Newtonian elastic liquids".

2 – Materials and methods

2.1 – Shape optimization routine

Figure 2.1 presents a schematic representation of the general procedure that was implemented to optimize the FFD.

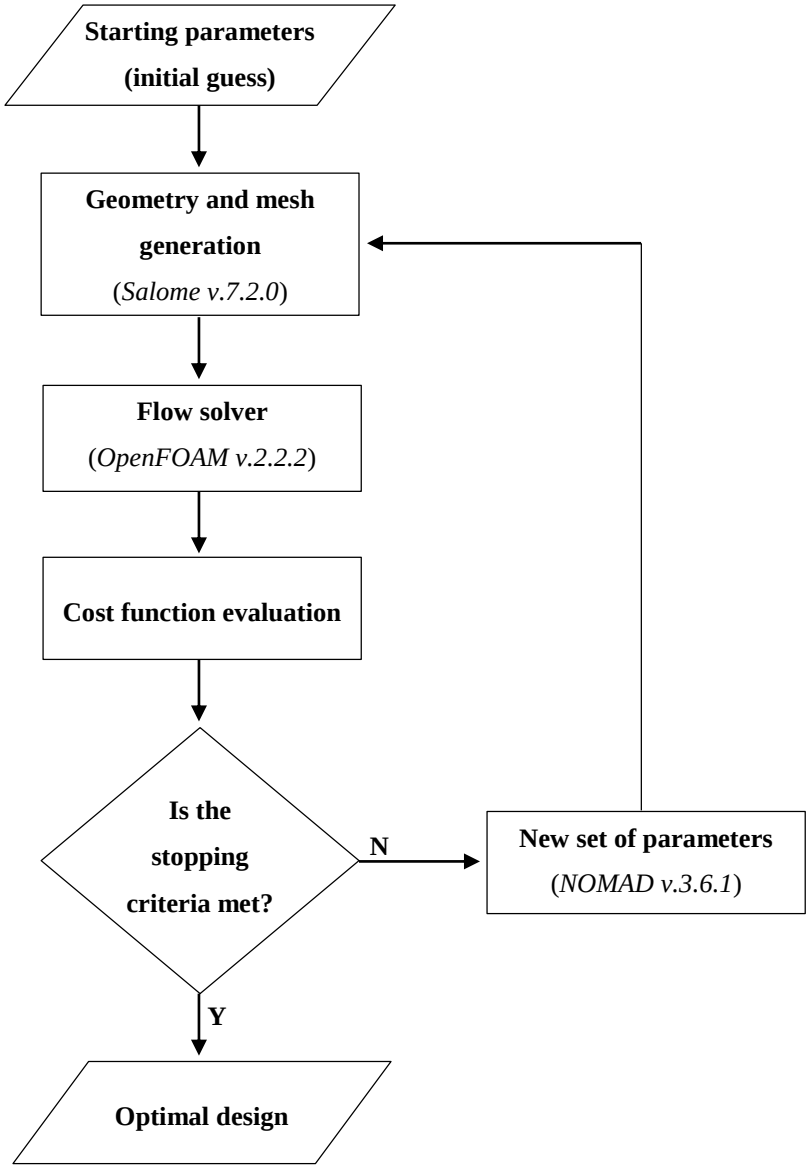

Figure 2.1 – Flowchart of the shape optimization routine. Words in italic identify the open-source software that was used in the corresponding task.

Briefly, the standard, non-optimized FFD, was parameterized on its corners and meshed on Salome-platform v.7.2.0 (Ribes & Caremoli, 2007). This was fed as input to OpenFOAM v.2.2.2 (*www.openfoam.org*) which was used to compute the flow field. Next, the velocity was sampled at the centerline of the geometry and the cost function was computed.

The new set of parameters, for the next iteration, was determined by the optimization algorithm coded in NOMAD v.3.6.1 (Audet *et al*., 2009; Le Digabel, 2011) and the cycle was repeated until the established convergence criteria was met. Each step of the flowchart is described in detail below.

2.1.1 – Geometry/mesh generation

The standard FFD geometry was parameterized on its corners through two Bézier curves, as depicted in Figure 2.2.

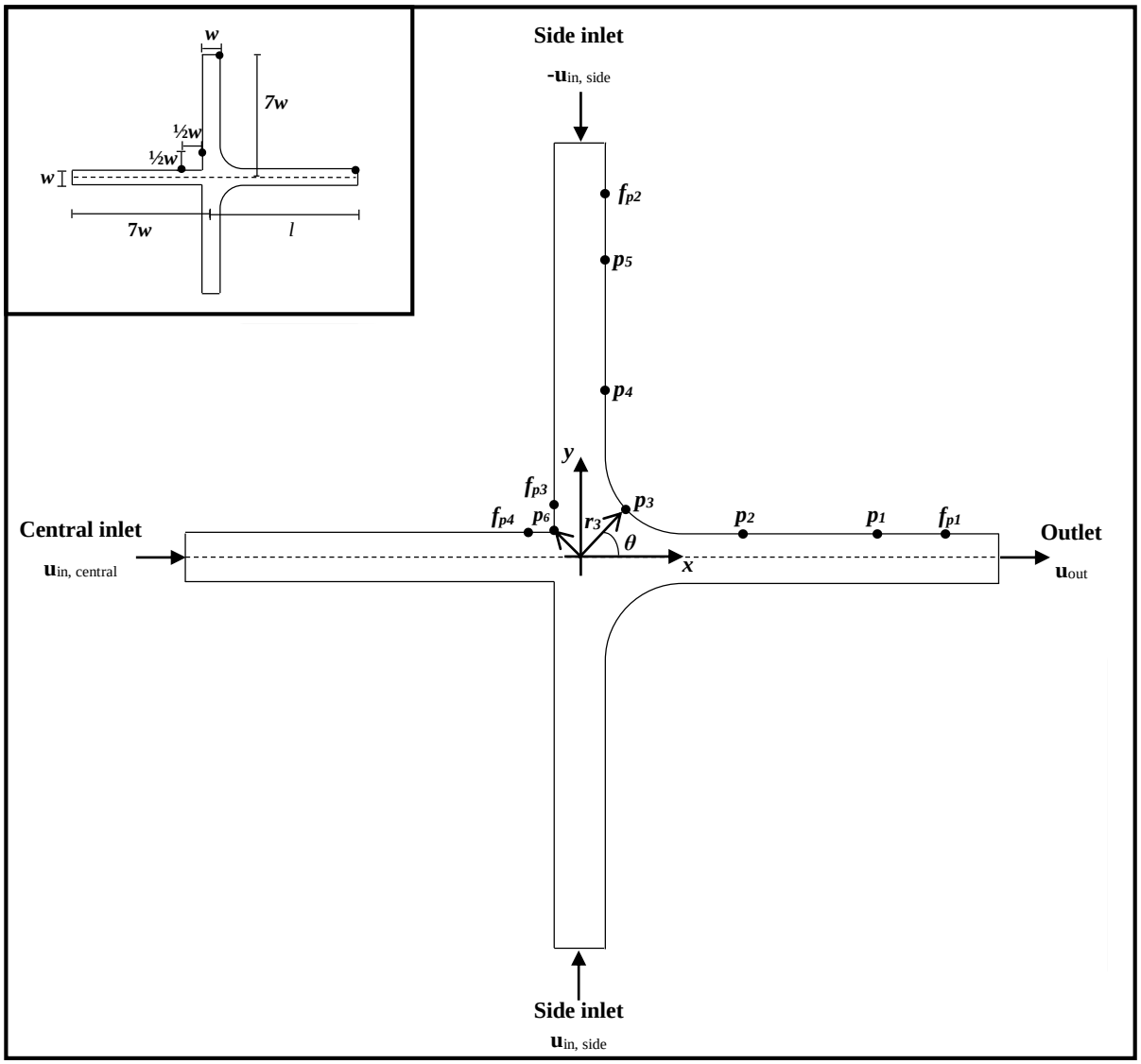

Figure 2.2 – Schematic representation of the FFD base plane in its initial (non-optimized) configuration. The location of each design point, p_1 to p_6, is represented by its distance from the origin (r_n) and the angle relative to the *x*-axis (θ). Points denoted as *fp* are fixed and delimitate the optimization region (the cross-sectional area of the channel is constant beyond those points). The dashed line is an axis of symmetry for the base plane. The inset scheme shows the dimensions of the FFD (*w* is the channel width and it is equal for the four arms), where the four dots represent fixed points (*fp*) in the main figure (points p_1 to p_5 are equally separated by the same angle; point p_6 is at an angle $\theta = 3\pi/4$ rad).

Five points (p_1 to p_5) control the shape of the downstream corner, through their distance r_n to the origin (θ angles were kept fixed), while only one parameter (r_6) was allowed in the upstream corner. The upstream corner was only parameterized in order to obtain a rounded edge, since sharp edges are more prone to trigger instabilities in viscoelastic flows – the cost function was practically insensible to this parameter. Note that all the dimensions of the geometry are defined as a function of the channel width.

The FFD was optimized both in 2D and 3D configurations, since each one is more suitable for a given application. For instance, a 2D configuration is preferred for rheological studies because the high aspect ratio reduces wall effects in birefringence measurements. On the other side, 3D geometries are more amenable to be produced by PDMS micro-molding, which is a popular technique due to its low-cost and simplicity. Additionally, 3D configurations were optimized for four different values of the l parameter (length of the extensional region, Figure 2.2), at a fixed aspect ratio, where the aspect ratio is the height to width ratio: $AR = h/w$, and for four different values of AR, at a fixed optimized length (l). Those conditions are summarized in Table 2.1.

Table 2.1 – Geometric parameters of the optimized devices (the geometry identifier is used in order to facilitate the identification of a given device; w – FFD channel width; w_c – contraction width in the expansion device). The aspect ratio for the 2D device is not presented since this was not relevant for the flow solver.

Configuration	**Geometry identifier**	**Aspect ratio (*AR*)**	**Optimized region length (*l*)**
2D	2D_7w	-	7*w*
3D	3D_AR1_1w	1	1*w*
	3D_AR1_2.5w		2.5*w*
	3D_AR1_5w		5*w*
	3D_AR0.5_7w	0.5	7*w*
	3D_AR1_7w	1	
	3D_AR2_7w	2	
	3D_AR4_7w	4	
	3D_AR1_exp	1	7w_c

Since the forced relaxation of highly stretched molecules may be also useful (and has received less attention than the extension), an expansion geometry was optimized for this purpose, Figure 2.3, which can be coupled at the outlet of a FFD. For this case, only one 3D configuration was optimized, at $AR = 1$, Table 2.1. Note that the final optimized shape could also be used as a contraction, in the same way the FFD may be used as an expansion by reversing the flow direction.

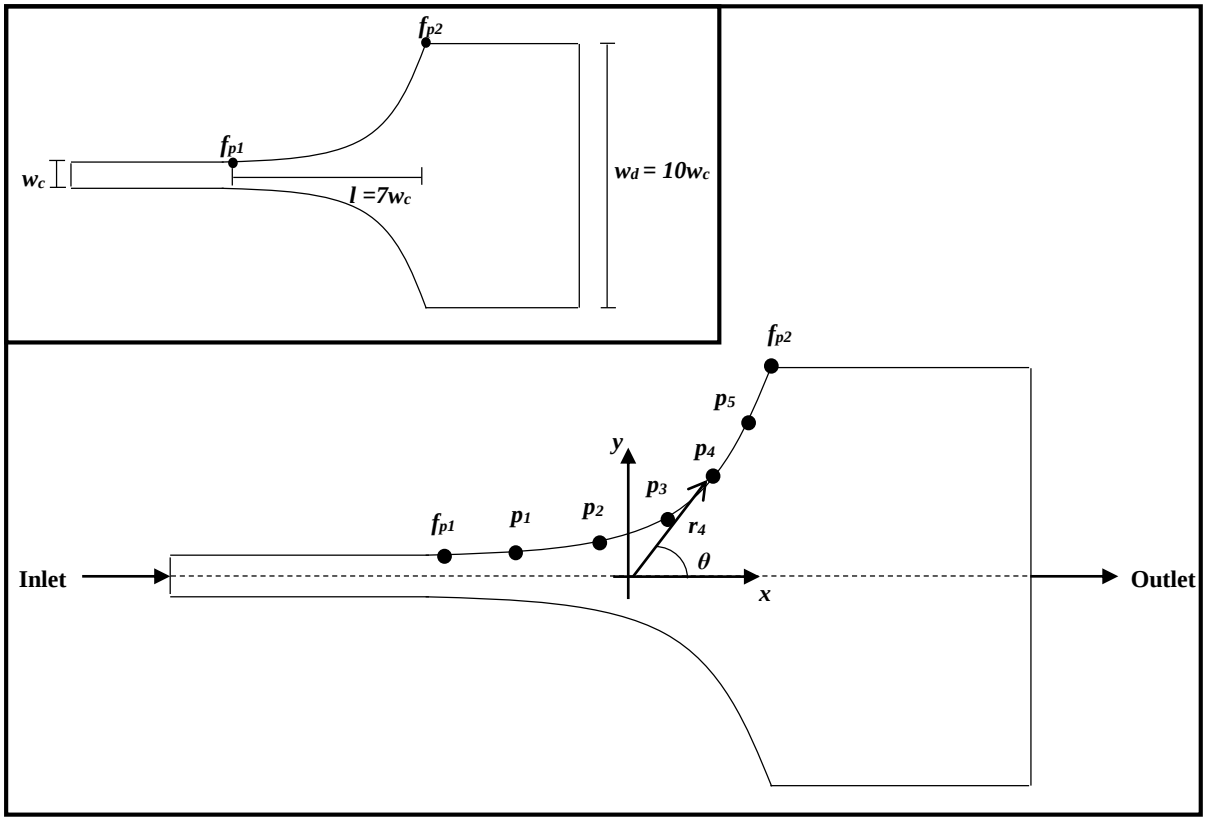

Figure 2.3 – Schematic representation of the expansion base plane in its initial (non-optimized) configuration. The location of each design point, p_1 to p_5, is represented by its distance from the origin (r_n) and the angle relative to the x-axis (θ). Points denoted as *fp* are fixed and delimitate the optimization region (the cross-sectional area of the channel is constant beyond those points). The dashed line is an axis of symmetry for the base plane. The inset scheme shows the dimensions of the expansion: both the optimized length (l) and the downstream channel width (w_d) are expressed as functions of the channel contraction width (w_c). Points p_1 to p_5 are equally spaced by the same (fixed) angle.

The Salome platform was selected as the geometry/mesh generator software, since it allows the construction of unstructured meshes. This type of meshes are more flexible than structured ones, although being also computationally more expansive. Note that in the present work, a new mesh was generated at each optimization iteration. Other authors only deformed a fixed mesh (Alves, 2008), although this procedure applied in the present work (on structured meshes) led to highly skew and heterogeneous meshes that compromised the convergence of the flow solver. Furthermore, the mesh generation was not the time limiting step in the optimization cycle.

In order to keep the mesh resolution constant, independently of the geometrical shape, the parameter that was specified in the mesh builder was the minimal/maximal cell size. Reference values of $w/30$ and $w/20$ for the minimal and maximal cell lengths (in all space dimensions, except in the z direction for the 2D dimensional case), respectively, were used,

based on a preliminary mesh independency study. The mixing of quadrangles with triangles was allowed, resulting in hexahedra-dominant meshes (Figure A.1).

2.1.2 – Flow solver

OpenFOAM, an open-source CFD software, was a straightforward choice to solve the flow field based on its applicability to viscoelastic fluids and high accuracy and stability. OpenFOAM is a finite volume C++ based CFD code that has a set of built-in solvers and also allows for the user to modify existing solvers or create its own solver. It offers several numerical schemes and, importantly, it handles unstructured meshes.

The built-in *simpleFoam* solver was directly used (after switching-off turbulence models) due to the flow characteristics: Newtonian and incompressible fluid, laminar and isothermal steady-state flow. This solver provides a solution for the steady-state Navier-Stokes equations:

$$\nabla \cdot \mathbf{u} = 0 \tag{2.1}$$

$$\rho \nabla \cdot \mathbf{uu} = -\nabla p + \mu \nabla^2 \mathbf{u} \tag{2.2}$$

Equation (2.1) represents the mass conservation (continuity equation), while (2.2) is the momentum conservation equation, where μ represents the fluid dynamic viscosity, ρ the fluid density and p the pressure. Field interpolations were performed through a standard central differencing scheme.

Boundary conditions were defined as follows. A fixed uniform velocity was assigned to all three inlets and a zero relative pressure was fixed at the outlet (while keeping a zero velocity gradient). To ensure the complete development of the flow at the entry to the optimized region and to avoid boundary perturbations at the outlet, both side channels and the outlet channel were extended 3 channel widths beyond the fixed points. In order to minimize inertial effects, *Re* at the outlet (here defined as $Re = \rho|\bar{\mathbf{u}}_{out}|w/\mu$, where $|\bar{\mathbf{u}}_{out}|$ is the average superficial velocity at the outlet) was kept below 1 (typically, $Re = 0.4$). An important variable to consider in the FFD is the velocity ratio between inlet streams, here defined as $VR = |\mathbf{u}_{in,\ side}|/|\mathbf{u}_{in,\ central}|$. Two different *VR* were tested in the optimization of the 2D_7w geometry: $VR = 10$ and 100. Note that while *Re* controls the total inflow (sides + central), it is the *VR* that determines the distribution of this flow between inlets ($|\bar{\mathbf{u}}_{out}| = \mu Re/(\rho w) = |\mathbf{u}_{in,\ side}|\ (2 + 1/VR)$). The no-slip condition was imposed on walls through a zero velocity on it and, in 2D geometries, the top and bottom planes were considered as empties. Due to the symmetry of the FFD on the O*xz* plane, only half of the geometry was solved. In the case of the expansion geometry, *Re* is the

sole flow parameter and was also kept below 1. The inlet, outlet and wall boundaries were treated in the same way as for the FFD.

Pressure and velocity relaxation factors were 0.3 and 0.7, respectively. Unless otherwise stated, standard residuals of 10^{-6} were used, for both velocity and pressure, as a criterion of solver convergence.

2.1.3 – Optimization algorithm

The cost function should be formulated in order to achieve a constant deformation rate along the *l* length, since this is the definition here adopted for a homogeneous extensional flow. Two cost functions were tested in the optimization of geometry 2D_7w and the best one was employed in the optimization of 3D geometries. In the first approach, the cost function, f_{cost}, comprised the squared residuals sum of the *x*-velocity component at the centerline:

$$f_{cost} = \sum_{i=1}^{np} \left[u_{x,cl}(x_i) - (mx_i - b) \right]^2 \quad , 0 < x_i < 7w \tag{2.3}$$

where $u_{x,cl}$ is the *x*-velocity component sampled at the centerline of the device ($y = 0$, $z = h/2$) and *m* and *b* represent the slope and *y*-intercept, respectively, of the linear regression that was fit to the *np* sampled points. Note that if $u_{x,cl} = f(x)$ is a linear function, then its derivative, which by definition corresponds to the deformation rate in the flow direction, is a constant value. The second cost function is similar to that used by Alves (2008) and it is based on a target profile:

$$f_{cost} = \sum_{i=1}^{np} \left[u_{x,cl}(x_i) - u_{x,tar}(x_i) \right]^2 \quad , -1.5w < x_i < 7.5w \tag{2.4}$$

$$u_{x,tar}(x_i) = \begin{cases} K \left| \mathbf{u}_{in,central} \right| \ , \ x_i < 0 \\ K \dfrac{2 \left| \mathbf{u}_{in,side} \right|}{l} x_i + K \left| \mathbf{u}_{in,central} \right| \ , \ 0 \le x_i < 7w \\ K \left(2 \left| \mathbf{u}_{in,side} \right| + \left| \mathbf{u}_{in,central} \right| \right) \ , \ x_i \ge 7w \end{cases} \tag{2.5}$$

In Eq. (2.4), $u_{x,tar}$ is the velocity profile desired at the centerline, which is a branched function (Eq. 2.5). Indeed, outside the optimized region, the velocity at the centerline is simply *K* times the average velocity in the channel, where *K* is a constant that correlates the average channel velocity with the velocity at the centerline (an expression for *K* is presented in Appendix B). Inside the optimized region, the theoretical velocity profile is set to a straight line, constructed from its extreme points, where the velocity is fixed by the channel cross-sectional area. Note that both cost functions force the linear profile to begin at $x = 0$, which is slightly downstream the entry to the flow-focusing region ($x = -w/2$). Although this conducted to a late

velocity rise, better results were obtained due to the smoother transition in the velocity profile. For the expansion geometry, only the cost function with better results for the FFD was used (with the required modifications in the function parameters to adapt it to the corresponding geometry). A schematic representation of both cost functions is depicted in Figure 2.4.

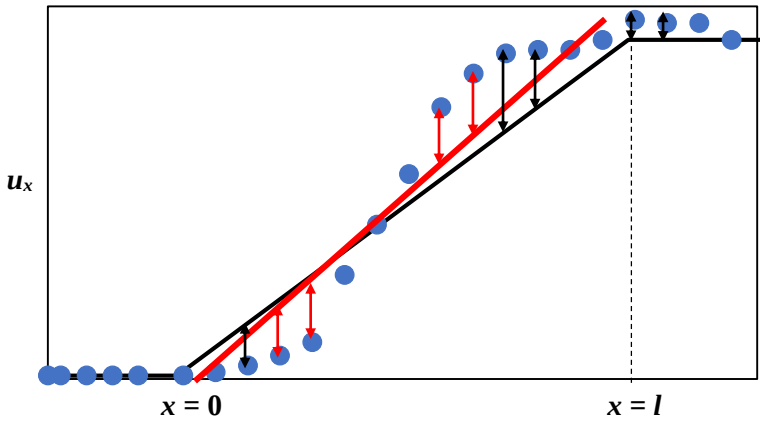

Figure 2.4 – Schematic representation of the two cost functions. If the points represent the sampled velocity profile in a geometry, at a given iteration of the optimization cycle, then the residuals minimization cost function starts to fit a linear function to those points (red line) and minimizes the residuals of that fitting procedure (red arrows). On the other hand, the profile fitting cost function tries to minimize the distance of those points to a target profile represented by the black line (black arrows denote this distance). The first cost function only has effect inside the optimization length, while the other one also has influence outside this region. Only a restricted number of arrows (distances) was represented for illustrative purposes.

NOMAD software was selected to minimize the cost function. It is an implementation of the MADS (Mesh Adaptive Direct Search) algorithm (Audet *et al.*, 2009; Le Digabel, 2011), thus being a free-derivative optimizer. The algorithm is composed of two steps that sample the cost function in a mesh predefined by the searching directions. The mesh is coarsened whenever an iteration finds a lower value of the cost function, while it is refined near actual parameters otherwise, until the searching radius drops below a user-defined threshold. Global convergence is not warranted, but NOMAD can optionally perform a metaheuristic search in order to avoid local minima. This search has a stochastic component since it is a random jump to a new mesh location, from which the main algorithm further proceeds, in the hope to find a better (different) solution than the previous one. The maximum number of such jumps is user-defined. In the present work, NOMAD was stopped and considered to achieve convergence when the searching radius dropped below 1 μm. The metaheuristic search was also enabled and limited to 20 % of the total number of cost function evaluations. The required number of iterations to achieve convergence was geometry-dependent, although most cases converged within 500-1000 NOMAD iterations.

2.2 – Viscoelastic flow simulations

Since the extensional flow in a FFD is suitable to study complex fluids, the optimized device (2D_7w) was tested for viscoelastic flows. Simulations were also conducted in OpenFOAM, since a recent solver for viscoelastic fluids was made available (Favero *et al.*, 2010). The Oldroyd-B constitutive equation was selected to model the viscoelastic behavior:

$$\boldsymbol{\sigma} + \tau \overset{\nabla}{\boldsymbol{\sigma}} = 2\mu_p \mathbf{D} \tag{2.6}$$

where $\boldsymbol{\sigma}$ is the extra-stress tensor, $\overset{\nabla}{\boldsymbol{\sigma}}$ denotes the upper-convected derivative of $\boldsymbol{\sigma}$ (defined as: $\overset{\nabla}{\boldsymbol{\sigma}} = \frac{\partial \boldsymbol{\sigma}}{\partial t} + \mathbf{u} \cdot \nabla \boldsymbol{\sigma} - \nabla \mathbf{u} \boldsymbol{\sigma} - \boldsymbol{\sigma} \nabla \mathbf{u}^{\mathrm{T}}$), τ is the relaxation time of the polymer, μ_p is the polymeric viscosity and $\mathbf{D}$ is the deformation rate tensor. In this case, the momentum equation is given as:

$$\rho \nabla \cdot \mathbf{u}\mathbf{u} = -\nabla p + \mu_s \nabla^2 \mathbf{u} + \nabla \cdot \boldsymbol{\sigma} \tag{2.7}$$

where μ_s is the solvent viscosity. In order to simulate a Boger fluid, which is a viscoelastic fluid with constant shear viscosity, the solvent viscosity ratio, defined as: $\beta = \mu_s / (\mu_p + \mu_s)$, was set to $\beta = 8/9$, with $\mu_s = 0.001$ Pa.s for water as the solvent. The flow strength, characterized by *We*, was controlled by changing the polymer relaxation time keeping fixed *Re* (all simulations were conducted at $Re = 0.18$) and, consequently, the deformation rate is also constant. For the range of *We* tested ($0.1 \leq We \leq 2$), the elasticity number ranged between 0.6 and 11. The time step was set to $\tau/2000$ to obtain stable and accurate calculations. The solution was considered converged after the residuals dropped below 10^{-6}, which usually occurred after 10 τ to 50 τ of computation. Note that the whole geometry was used in these simulations, without imposing symmetry planes, in order to detect any flow asymmetry that can occur at high *We*.

2.3 – Brownian dynamics simulations of DNA

2.3.1 – Model description

Aiming to evaluate the performance of the optimized devices in stretching DNA molecules, Brownian dynamics simulations were performed. At the coarse-grain scale, bead-spring and bead-rod models are widely used for this purpose (Larson, 2005). In the present work, a bead-spring model was implemented. The governing equations are described in detail elsewhere (Huang *et al.*, 2014; Jendrejack *et al.*, 2002; Kim & Doyle, 2006; Larson, 2005).

In a bead-spring model, a DNA molecule is represented by N_b beads, which are interconnected through N_s springs ($N_s = N_b$-1), Figure 2.5.

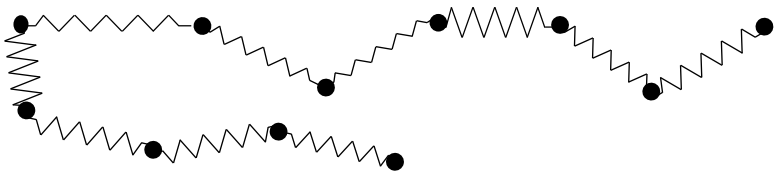

Figure 2.5 – DNA molecule represented by a bead-spring model (N_b = 11, N_s =10).

The behavior of a DNA molecule in a flow can be simulated through the balance between five forces: drag force ($\mathbf{F}_i^D$), spring force ($\mathbf{F}_i^S$), Brownian force ($\mathbf{F}_i^B$), exclusion volume interactions ($\mathbf{F}_i^{EV}$) and hydrodynamic interactions ($\mathbf{F}_i^{HI}$). Then, a force balance should be applied to each bead (neglecting bead inertia):

$$\mathbf{F}_i^D + \mathbf{F}_i^S + \mathbf{F}_i^B + \mathbf{F}_i^{EV} + \mathbf{F}_i^{HI} = 0 \tag{2.8}$$

The drag force, $\mathbf{F}_i^D$, acts on each bead by the surrounding fluid, depending on the relative velocity between the fluid and the bead:

$$\mathbf{F}_i^D = -\zeta\left(\frac{d\mathbf{x}_i}{dt} - \mathbf{u}(\mathbf{x}_i)\right) \tag{2.9}$$

where $\mathbf{x}_i$ is a 3D vector representing the bead i position, $\mathbf{u}(\mathbf{x}_i)$ is the fluid velocity at that position and ζ is the drag coefficient (in the simplest case, Stokes-law may be applied, $\zeta = 6\pi\mu r_b$, with μ being the fluid viscosity and r_b the bead radius). It follows from Eqs. (2.8) and (2.9) that the position of bead i at time t is such that:

$$\frac{d\mathbf{x}_i}{dt} = \mathbf{u}(\mathbf{x}_i) + \frac{1}{\zeta}\left(\mathbf{F}_i^S + \mathbf{F}_i^B + \mathbf{F}_i^{EV} + \mathbf{F}_i^{HI}\right) \tag{2.10}$$

For the spring force, the Marko–Siggia model (Marko & Siggia 1995) was adopted, since it limits the length of a spring to a maximum value, avoiding the infinite extension allowed by the simple Hookean model. The spring force is given as:

$$\mathbf{f}_{ij}^S = \frac{k_B T}{\lambda_p}\left[\frac{|\mathbf{X}_{ij}|}{L_S} - \frac{1}{4} + \frac{1}{4}\left(1 - \frac{|\mathbf{X}_{ij}|}{L_S}\right)^{-2}\right]\frac{\mathbf{X}_{ij}}{|\mathbf{X}_{ij}|} \tag{2.11}$$

where k_B is the Boltzmann's constant, T is the absolute temperature of the system, λ_p is the persistence length of a spring, which is equivalent to half a Kuhn step, L_S is the maximum extension of a spring and $\mathbf{X}_{ij}$ is the connection vector between consecutive beads i and j ($\mathbf{X}_{ij} = \mathbf{x}_j$-$\mathbf{x}_i$). Note that the L_S parameter is defined as the contour length of the molecule divided by the

number of springs ($L_S = L_C/N_s$). Since each bead, except at the borders, is connected to two other beads, the term $\mathbf{F}_i^S$ in Eq. (2.10) is a branched function:

$$\mathbf{F}_i^S = \begin{cases} \mathbf{f}_{i,i+1}^S, i = 1 \\ \mathbf{f}_{i,i+1}^S + \mathbf{f}_{i,i-1}^S, 1 < i < N_b \\ \mathbf{f}_{i,i-1}^S, i = N_b \end{cases} \tag{2.12}$$

The Brownian force term represents the thermal agitation and it is a random force, although subjected to restrictions in its first and second moments (Kim & Doyle, 2006). This term can be expressed as:

$$\mathbf{F}_i^B = k_B T \sqrt{\frac{6\zeta}{\Delta t\, k_B T}}\, \mathbf{S} \tag{2.13}$$

where $\mathbf{S}$ is a 3D vector whose components are uniformly distributed numbers in the range [-1,1] and Δt is the discrete time-step.

Exclusion volume forces impose a repulsion between beads, which would theoretically avoid the crossover between springs. In this work, the soft repulsion potential proposed by Jendrejack *et al*. (2002) was used:

$$\mathbf{F}_i^{EV} = -\frac{k_B T}{L_s} \sum_{j=1}^{Nb} \frac{9}{2} \frac{v}{L_S^3} \left(\frac{3}{4\sqrt{\pi}} \right)^3 \left(\frac{L_S}{\lambda_p} \right)^{\frac{9}{2}} \exp\left(-\frac{9}{4} \frac{\left|\mathbf{X}_{ij}\right|^2}{\lambda_p L_S} \right) \frac{\mathbf{X}_{ij}}{\left|\mathbf{X}_{ij}\right|} \tag{2.14}$$

where v is the excluded volume potential parameter. Notwithstanding the repulsion potential between beads, springs can in practice cross each other (Jendrejack *et al*., 2002).

The last force term in Eq. (2.8) refers to hydrodynamic interactions that account for the velocity disturbance originated by the molecule itself. This occurs when the presence of a bead (representing a fraction of the molecule) changes locally the velocity field of the flow, such that the remaining beads of the chain will experience a different velocity when traversing that position. In addition, the disturbance depends on the stretched state of the molecule. These forces are particularly important for long flexible molecules (Larson, 2005), since in those cases coiled states are likely to exist and blinding effects inside the coil are not negligible. However, the free-draining hypothesis (omission of hydrodynamic interactions) has shown to predict the stretch when the drag coefficient is adjusted such that the model is able to reproduce the molecule equilibrium state (Jendrejack *et al*., 2002; Larson, 2005). In this work, the free-draining hypothesis was adopted, although this approximation should be considered as a topic of further investigation.

As opposed to other authors (e.g. Huang *et al*., 2014; Kim & Doyle, 2006), the wall-bead repulsion force was not necessary to implement in the present work, since the flow is not confined (the bead-wall repulsion is weak) and the molecules had no tendency to cross the walls.

2.3.2 – Parameters

Simulations were accomplished for λ-DNA, a molecule with 48.5 kbp and a contour length of 21 μm when intercalated with the YOYO-1 fluorescent dye (Larson, 2005). This molecule is widely used in single-molecule studies and its behavior in extensional flows was already reported in a number of experimental studies (e.g. Perkins *et al*., 1997, Smith & Chu, 1998). Furthermore, its relative small length decreases the contribution of hydrodynamic interactions.

In the bead-spring model described there are four adjustable parameters: N_b, λ_p, v and ζ. For λ-DNA, the number of beads should be in the range 10–20 and each spring should represent 10 or more Kuhn steps for accurate results (Larson, 2005). The other two parameters are set such that the relaxation time (τ[s] = 0.1μ_s, in a solvent of viscosity μ_s expressed in cP, Larson, 2005), molecular diffusivity ($D = k_bT/\zeta$ = 0.0115 μm^2/s for YOYO stained λ-DNA at 23 ºC in a 43 cP solvent, Jendrejack *et al*., 2002) and equilibrium length (1.7-1.8 μm for stained DNA, Larson, 2005) are well predicted by the model. This prediction is verified by adjusting an exponential function, Eq. (2.15), to the stretch *vs.* time data of a molecule allowed to relax in the absence of flow, after being stretched up to 70 % of its contour length.

$$\left\langle L^2(t)\right\rangle = L_0^2 + A\exp\left(-\frac{t}{\tau}\right) \tag{2.15}$$

In Eq. (2.15), $L(t)$ is the time-dependent length of the molecule, defined as the maximum inter-bead distance in the molecule, L_0 is the length of a molecule at equilibrium and A is a fitting parameter. The exponential function was only adjusted to data after the length of the molecule has been reduced to below 30 % of its contour length, in order to avoid the initial phase of fast relaxation. Results were averaged for 300 molecules (Figure A.2).

In the present work, the following parameters proved to reproduce accurately the equilibrium state of λ-DNA: N_b = 11, λ_p = 0.076 μm, v = 0.0004 μm^3, ζ = 3.8x10^{-8} kg/s (with an equivalent coil diffusivity of 0.01 μm^2/s), in a solvent with a viscosity of 43 cP, hence a DNA relaxation time of 4.3 s. Note that the coil diffusivity could be also approximated by the Rouse formula for the relaxation time, giving a value of 0.0109 μm^2/s (Larson, 2005).

2.3.3 – Numerical scheme

The motion equation, Eq. (2.10), can be evolved in time using several time-stepping schemes. The explicit Euler scheme is straightforward to implement, but the time-step should be low enough for stability reasons. Indeed, for large time-steps, springs are allowed to exceed its maximum length (L_S), leading to unphysical results (Kim & Doyle, 2006; Somasi *et al.*, 2002). Low time-steps are allowed, but the computational time becomes an issue of concern. Somasi *et al.* (2002) proposed a predictor-corrector method to solve this problem and Kim & Doyle (2006) implemented a hybrid method (Euler-Newton) as an alternative. In the present work, the hybrid method was used. Briefly, the motion equation is decomposed and firstly computed without the spring force term, using an explicit first-order Euler scheme:

$$\mathbf{x}_i^* = \mathbf{x}_{i,t} + \Delta t\left[\mathbf{u}(\mathbf{x}_{i,t}) + \frac{1}{\zeta}\left(\mathbf{F}_{i,t}^B + \mathbf{F}_{i,t}^{EV}\right)\right] \tag{2.16}$$

The intermediate bead position ($\mathbf{x}_i^*$) is then used to add the spring force term:

$$\mathbf{x}_i^{**} = \mathbf{x}_i^* + \frac{\Delta t}{\zeta}\left(\mathbf{F}_{i,t}^S\right) \tag{2.17}$$

If the resulting bead positions of a molecule ($\mathbf{x}_i^{**}$) are such that any spring exceeds its maximum length, the new positions are set to the computed value: $\mathbf{x}_{i,t+\Delta t} = \mathbf{x}_i^{**}$. However, when this condition is not verified, position vectors are implicitly equated as follows:

$$\mathbf{x}_{i,t+\Delta t} = \mathbf{x}_i^* + \frac{\Delta t}{\zeta}\left(\mathbf{F}_{i,t+\Delta t}^S\right) \tag{2.18}$$

Equation (2.16) is then linearized and iteratively solved using Newton's method, until residuals (the absolute difference between position vectors components from consecutive iterations) dropped below a threshold value, here defined as 0.001 μm.

Notwithstanding the stability of the described method, accuracy should also be ensured, which limits the maximum time-step allowable. Several criteria were used in Brownian dynamics simulations (Hsieh *et al.*, 2003; Jendrejack *et al.*, 2002; Kim & Doyle, 2006; Trahan & Doyle, 2009) and there is not a general rule that holds for all geometries/flow strengths. In the present work, the same approach of Hsieh *et al.* (2003) was undertaken: the maximum time-step was established such that the model still predicted the equilibrium state of DNA molecules. The following rule proved to be conservative for the tested cases: Δt [s] = 0.04/*We*.

2.3.4 – OpenFOAM implementation

The numerical scheme was implemented in OpenFOAM, since this software already has an efficient and robust Lagrangian particle-tracking algorithm (Macpherson *et al*., 2009). Both classes *solidParticle* and *solidParticleCloud* were modified accordingly to handle the physical model that was described. Briefly, the flow is solved uncoupled from molecular simulations and the converged velocity is interpolated from cell centers to faces centers (cubic scheme interpolation). Due to this important feature, two beads at different locations within the same mesh cell will have different velocities and a quasi-continuous velocity field is created over all the geometry. Without cell-to-face interpolation, the flow would have to be solved in a very fine mesh and the algorithm would be significantly slower. After the molecule has been placed at a given initial position in the mesh, an overall search is performed over all the geometry until the cell that contains each bead is located. The motion of each bead starts at that moment. For a given Eulerian time-step (Δt), the field velocity at the bead position is interpolated every time a bead crosses a face of a cell. Thus, each Eulerian time-step is actually split on n Lagrangian time-steps. However, the spring, Brownian and exclusion volume forces are only computed at the end of each Eulerian time-step. The interpolation of the field velocity at bead positions followed a simple linear scheme, weighted by the inverse of the bead-to-faces distance.

2.3.5 – Simulation conditions

Before molecules are introduced in the flow, they are allowed to equilibrate at no-flow conditions – the drag force is switched-off in the motion equation, remaining only active Brownian, spring and exclusion volume forces. This process starts with a molecule in a random configuration and has a duration of 10 τ (43 s, in this work).

The 3D geometry 3D_AR1_7w was selected to test the performance of the optimized FFD in Brownian dynamics simulations. In order to test the molecular relaxation of highly stretched molecules, an inverted FFD was placed at the outlet of the first FFD, resulting in a double FFD that imposes a forced extension-relaxation flow. The ensemble of molecules was uniformly distributed along a vertical line that crosses the fixed point f_{p4} (Figure 2.2), which delimitates the optimized region in the upstream corner. This line is located at half-depth of the device ($z = h/2$). When placing the molecules in their (random) equilibrium conformation at that position, it is assumed that the shear stress experienced by molecules since they enter the device until they reach the line has no significant effects on its state. This is a good

approximation for molecules travelling near the centerline, where the shear stress is negligible. For simulation purposes, the characteristic dimension of the optimized channels was set to w = 100 μm.

Unless otherwise stated, all results were averaged for an ensemble of 300 molecules, generated for each flow condition, since little variation was observed in the computed average for samples with this size (Figure A.3). In addition, the average stretch and other relevant results that are presented were sampled at 33 fixed positions in the device, equally spaced from each other along the controlled region.

2.4 – Experimental validation

Simulation results were experimentally validated to assess *VR* and *Re* effects on the velocity profile at the centerline for three selected geometries: 3D_AR1_5w, 3D_AR1_7w and 3D_AR1_exp. For fabrication purposes, the channels characteristic dimension was set to w = 100 μm.

2.4.1 – Fabrication of microfluidic devices

The channels were fabricated in PDMS (Sylgard 184, Dow Corning) from an SU-8 photoresist mold obtained from a chromium mask. The height of the channels was inspected through the visualization of a cross-sectional slice of the channels in an inverted microscope (Olympus IX83) and a value 5 μm higher than the projected one (100 μm) was found. The actual depth of the fabricated channels (h = 105 μm) was considered to compute the average velocity for normalization of the experimental velocity profiles.

2.4.2 – Working fluids and μ-PIV

The validation was performed with distilled water, at a temperature of 296 K. The working fluid was seeded with 1 μm diameter fluorescent particles (Fluo-Sphere carboxylate-modified, nile red, Ex/Em = 535/575 nm), diluted to 400 ppm, for μ-PIV experiments. A small amount of surfactant (sodium dodecyl sulfate, at approximately 100 ppm) was also included in the working fluid in order to minimize the particle adhesion to the walls.

The flow was driven using three neMESYS low pressure syringe pumps (Cetoni GmbH), each one independently connected to a channel inlet. The outlet was left open to the atmosphere. Depending on the flow rates, which ranged from 0.0002 μL/s to 2.5 μL/s, different Hamilton syringes (5 μL, 25 μL and 2.5 ml) were used to cover the wide range of *VR* and *Re*

tested. It should be noted that the flow in a FFD is particularly challenging at low *Re* and high *VR*, since very low flow rates are imposed in the central inlet channel at such conditions.

A CMOS camera (Phantom Miro M340, Vision Research) was used in μ-PIV experiments to collect images from the inverted microscope with a 10x objective (numerical aperture: 0.30). The illumination was provided by a double-pulsed Nd:YLF laser operating at a wavelength of 526.5 nm. For each flow condition, 50 pairs of images were collected and the time step between consecutive frames was adjusted depending on the flow conditions. Post-processing was performed with the DynamicStudio software (version 2.30.47, Dantec Dynamics).

3 – Results and discussion

3.1 – Optimized geometries

3.1.1 – 2D configurations

The optimized 2D geometries are presented in Figure 3.1 together with the standard FFD from which they were originated. The performance of each device can be evaluated in Figure 3.2, analyzing the respective velocity and deformation rate profiles at the centerline, for different *VR* and *Re* (there is a direct correspondence between legend letters of Figure 3.1 and Figure 3.2). In order to facilitate the comparison between different flow conditions, both velocity and deformation rate profiles are presented in a dimensionless form in the remainder of this work: $U = u_x/(K|\bar{\mathbf{u}}_{out}|)$ and $E = \dot{\varepsilon}/(K|\bar{\mathbf{u}}_{out}|/l)$, respectively. Note that $K|\bar{\mathbf{u}}_{out}|/l$ is not the theoretical deformation rate at the centerline ($\dot{\varepsilon}_{the} = 2K|\mathbf{u}_{in,\ side}|/l$), but it is preferred for simplicity of use because it is independent of the *VR*, for constant *Re*.

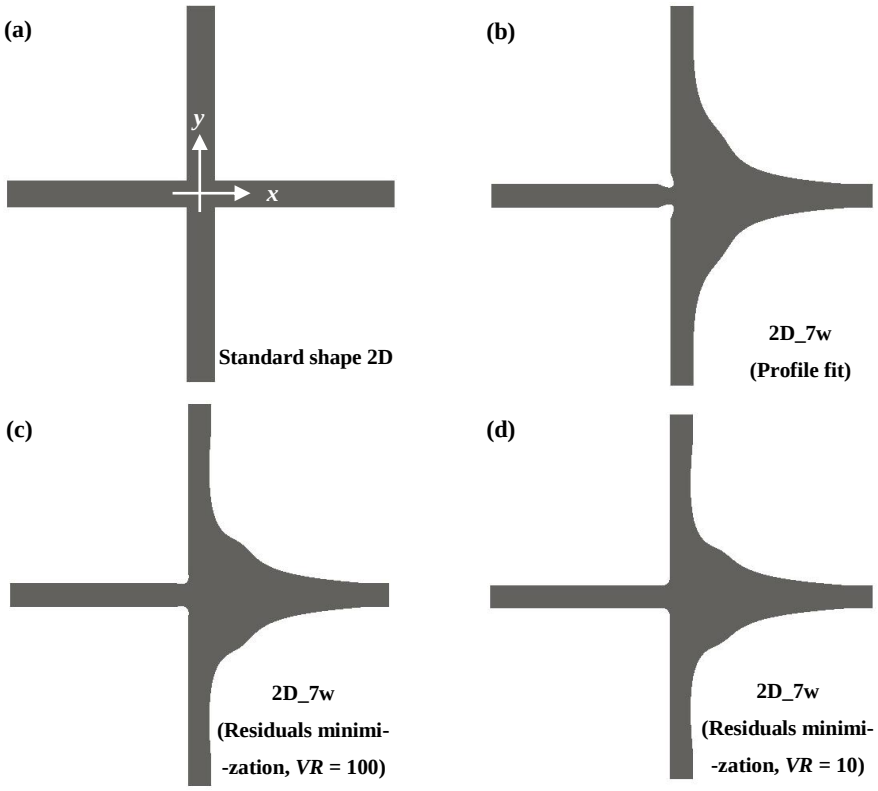

Figure 3.1 – Top view of the 2D standard and optimized geometries. Each arm of the FFD represented measures 8*w* from the origin (the Cartesian system illustrated in (a) is also valid for the other geometries). Figure (b) refers to the geometry optimized through a cost function that minimizes the deviation of the velocity profile at the centerline to an imposed profile (Eq. 2.4). Figures (c) and (d) represent the optimized geometries for a cost function that minimizes the residuals sum of the velocity profile fitted to a linear model (Eq. 2.3), at *VR* = 100 and 10, respectively. See Materials and methods section for references about the cost function and Table 2.1 for legend definition.

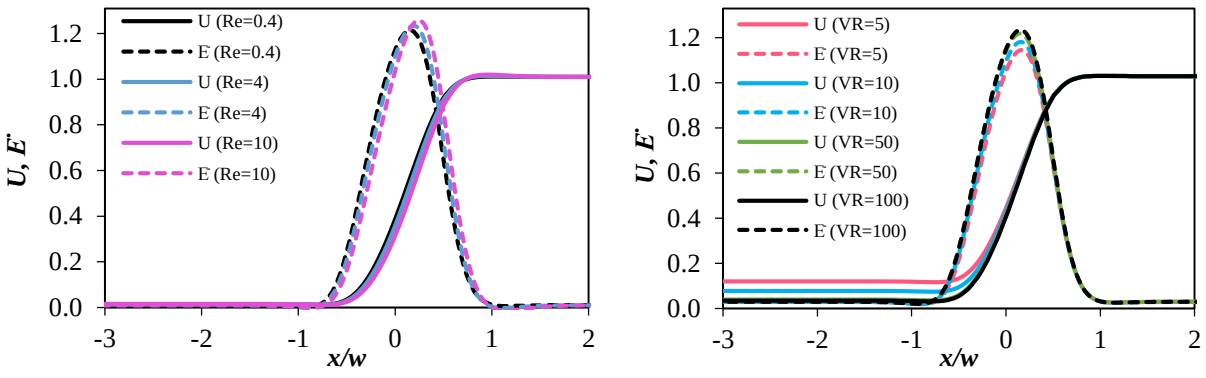

(a) Standard shape (2D)

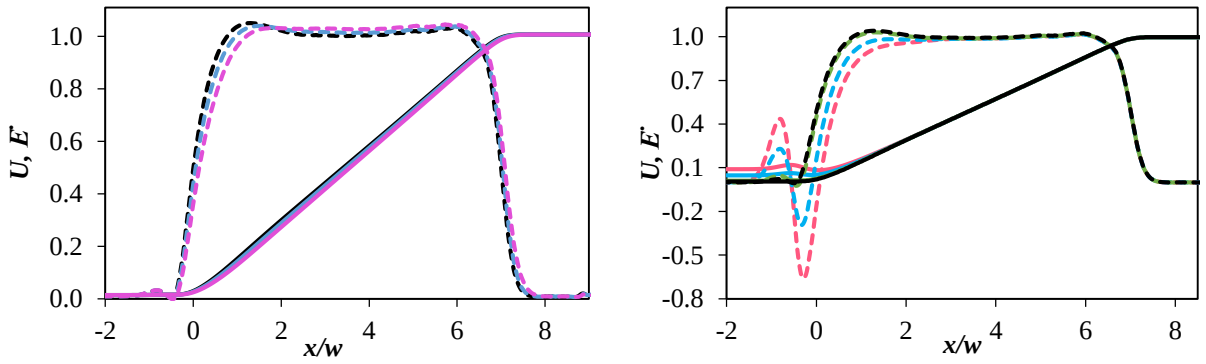

(b) 2D_7w (Profile fit)

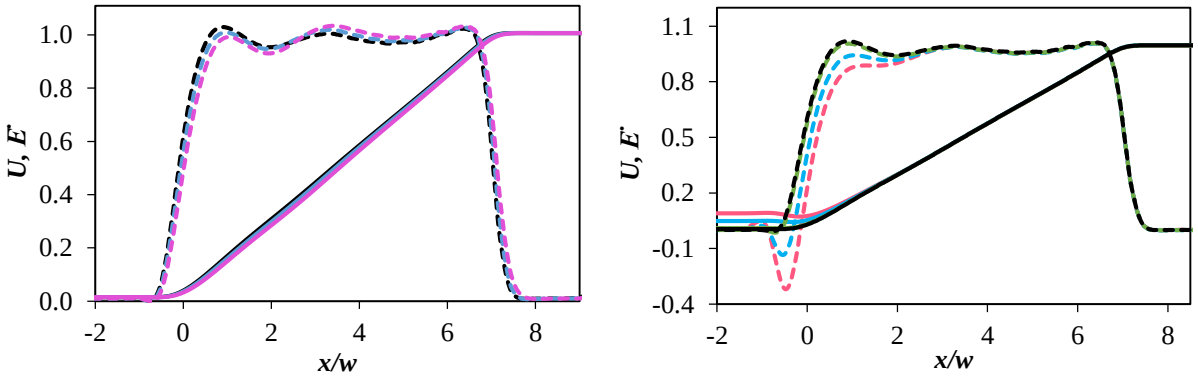

(c) 2D_7w (Residuals minimization, optimized at *VR* = 100)

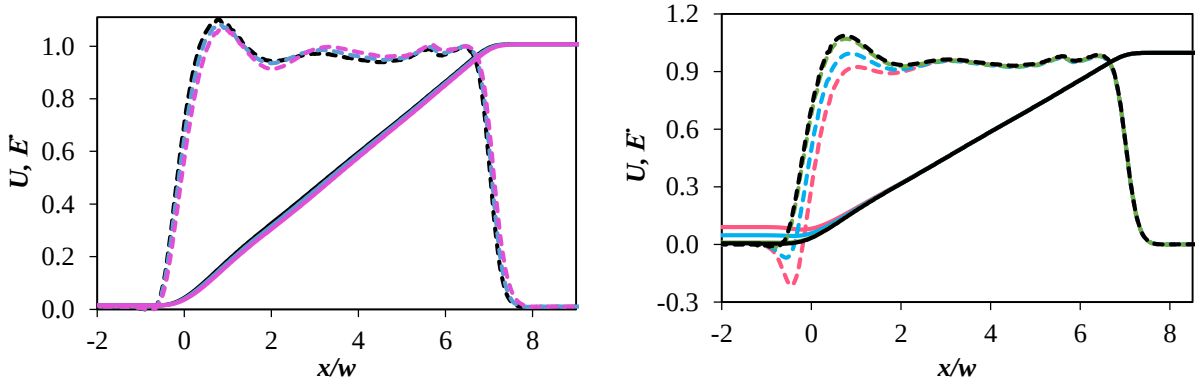

(d) 2D_7w (Residuals minimization, optimized at *VR* = 10)

Figure 3.2 – Normalized velocity and deformation rate along the centerline of the FFD (y = 0) for different flow conditions: in the left plots, *VR* = 100 and *Re* was the variable parameter; in the right plots, *Re* = 0.4 and *VR* was the variable parameter. The legend presented in (a) is also valid for the other plots.

In the standard FFD, the deformation rate profile does not effectively reach a plateau, taking the form of a bell-shaped curve, Figure 3.2(a). For this reason, the extensional region is not homogeneous and it is not possible to assume that *We* is constant in this device, which creates difficulties in the characterization of the extensional flow. Those problems are circumvented in the optimized FFD, since there is effectively an extended region of quasi-constant deformation rate, Figure 3.2(b)-(d). Furthermore, due to the increased distance of the walls to the centerline after the optimization procedure, the homogeneous extensional flow field is generated in the vicinity of this region, with reduced shear effects, Figure 3.3(a). Interestingly, the optimized shapes present a small concavity in the parameterized edge that has also been observed by Alves (2008) in the optimization of a 2D cross-slot for similar purposes and that presumably has a lubrication effect. As can be observed in Figure 3.3(b), the streamlines take a hyperbolic form in the extensional region of the optimized FFD, away from the walls.

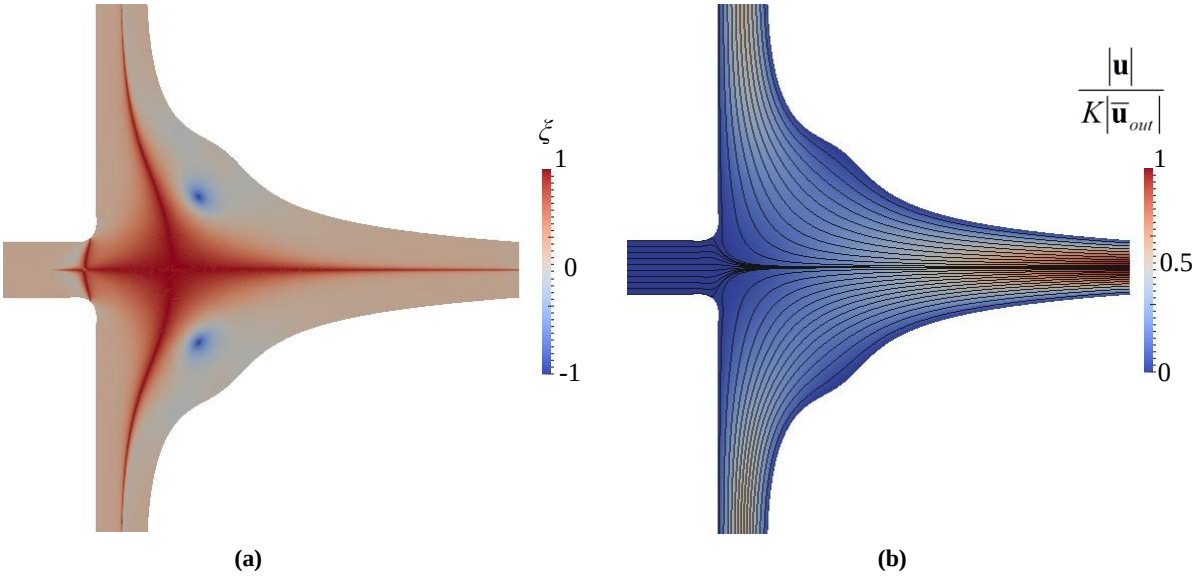

Figure 3.3 – (a) Flow type parameter contour plot and (b) velocity map with superimposed streamlines for the 2D_7w geometry (residuals minimization, optimized at *VR* = 100) at *Re* = 0.4 and *VR* = 100.

The two different cost functions tested yielded different optimized geometries, notwithstanding the similarity between both functions. Although the geometry optimized through the profile fit has a more homogeneous deformation rate profile along the centerline at high *VR* than the optimized geometry resulting from residuals minimization, a considerable overshot-undershoot sequence is observed at the entrance to the flow-focusing region for this geometry (Figure 3.2(b)-(c)). This is due to the more pronounced contraction in the central channel at the inlet to the flow-focusing region, which reduces locally the cross-sectional area (Figure 3.1(b)-(c)). This oscillation in the deformation rate profile may be amplified in viscoelastic flows, possibly leading to local elastic-driven flow instabilities. Thus, 3D

geometries were optimized using the residuals minimization as the cost function, based on this criterion.

The optimization for different *VR* also conducted to distinct shapes, although with only minor differences between them (Figure 3.1(c)-(d) and Figure 3.2(c)-(d)). The behavior for different *Re* is the same in both cases. However, the resulting profile is slightly more homogeneous at the same *VR* used in the optimization and worsens for different *VR* values, suggesting a compromise in what respects this parameter. Since a higher *VR* corresponds to a higher Hencky strain, the 3D geometries were optimized for $VR = 100$, keeping in mind practical applications that require large Hencky strains.

The increase of the velocity undershoot at the entry to the flow-focusing region for decreasing values of *VR* (Figure 3.2) is due to the higher penetration length of the central stream in the flow-focusing region, since lateral streams have a less intense compression effect when *VR* decreases. Thus, the central stream still experiences a velocity reduction, originated by the expansion effect, before increasing its velocity when squeezed by the lateral streams. However, this has no further effects in the remainder of the velocity profile (Figure 3.2), since the dimensionless velocity profile downstream of the entry length is independent of the *VR*, being only dependent on *Re* (which is fixed when changing the *VR*). The entry length can be easily identified in Figure 3.2 as the region where the profiles do not overlap for different *VR*. As expected, the entry length increases when *VR* decreases.

Overall, the optimized shapes present a wide region of constant deformation rate for $Re < 10$ (see Figure A.4 for results at $Re = 50$) and $VR > 5$ (decreasing the *VR* will increase the entry length, but the velocity profile will not change downstream of it). For very high *VR*, a recirculation forms at the entry to the flow-focusing region – a similar effect is discussed in detail in Oliveira *et al.* (2012) –, but the velocity profile remains unchanged when compared to that at $VR = 100$, since at $VR = 100$ the contribution of the central stream to the total flow rate is already low (see Figure A.5 for an example at $VR = 2400$). In the limit of increasingly higher *VR*, a stagnation point would result at the merging location of the lateral streams.

An important detail worth to be mentioned about the optimization routine is that similar geometrical shapes were obtained for different sets of design parameters. For instance, when two adjacent points moved toward opposite directions with the same displacement, only minor changes occurred in the shape of the Bézier curve. This feature leads to an increased search space of the design variables and it is in part due to the global control property of Bézier curves.

3.1.2 – 3D configurations

The optimized 3D geometries are presented in Figure 3.4 and the corresponding dimensionless velocity and deformation rate profiles are shown in Figure 3.5. When *AR* increases, the shape of the devices (for $l = 7w$) approaches those obtained for 2D configurations, with the salient concavity.

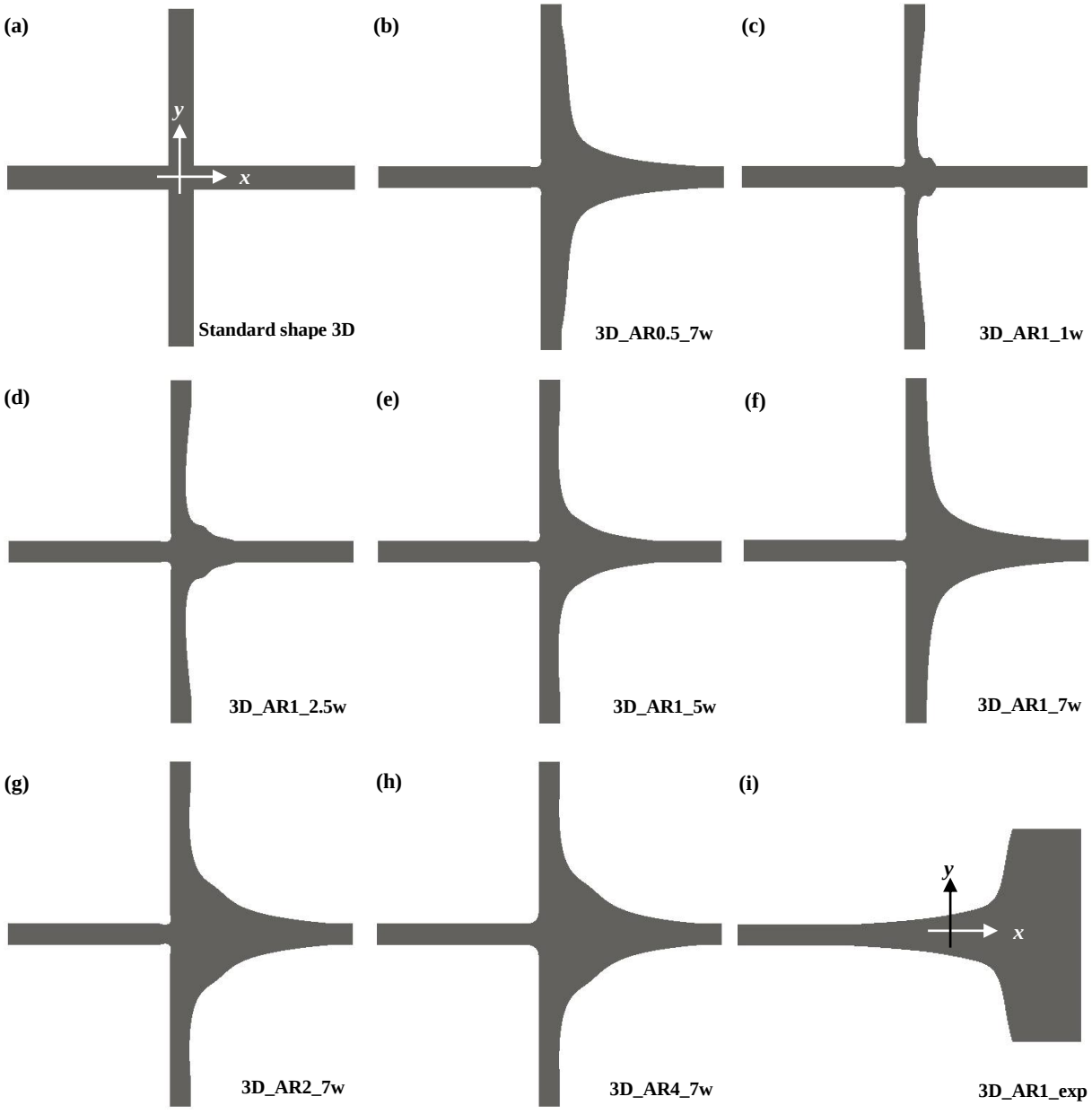

Figure 3.4 – Top view of the 3D standard and optimized geometries. Each arm of the FFD represented measures 8*w* from the origin (the Cartesian system illustrated in (a) is also valid for geometries (b)-(h)). The expansion (i) is represented with a streamwise length of $15w_c$ in the *x*-direction. See Table 2.1 for legend definition.

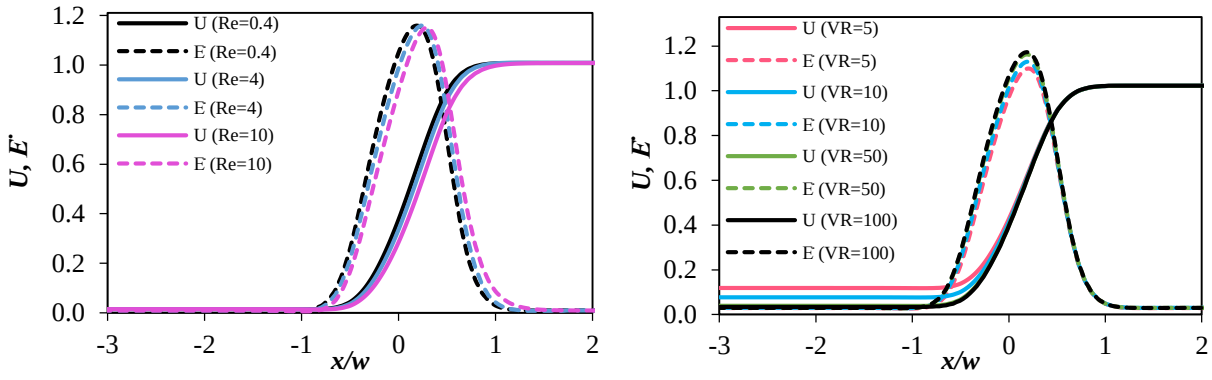

(a) Standard shape (3D)

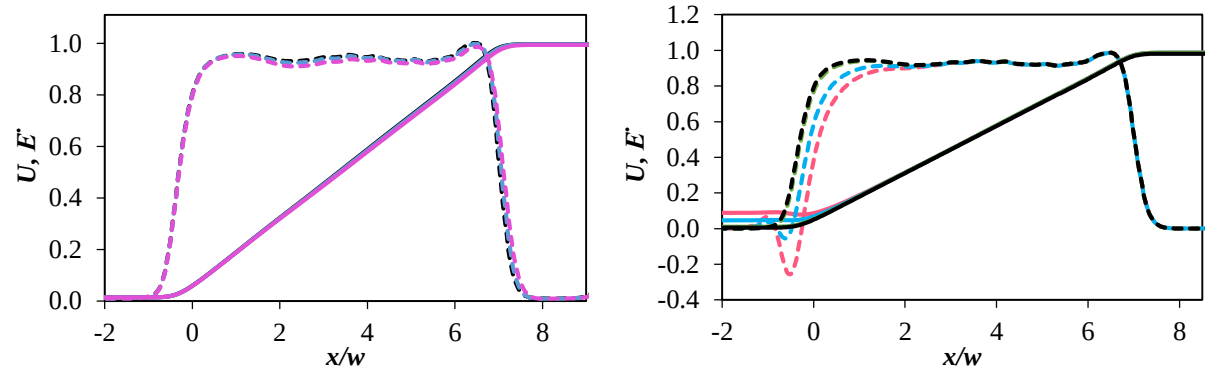

(b) 3D_AR0.5_7w

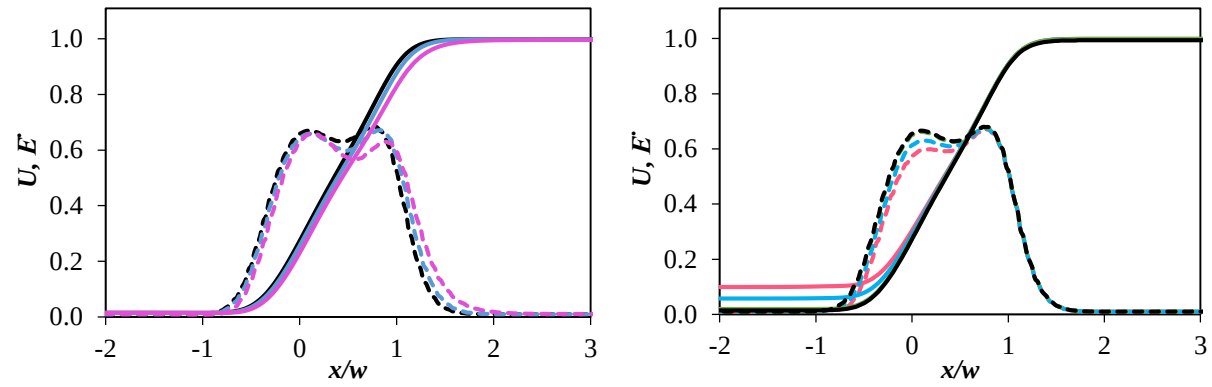

(c) 3D_AR1_1w

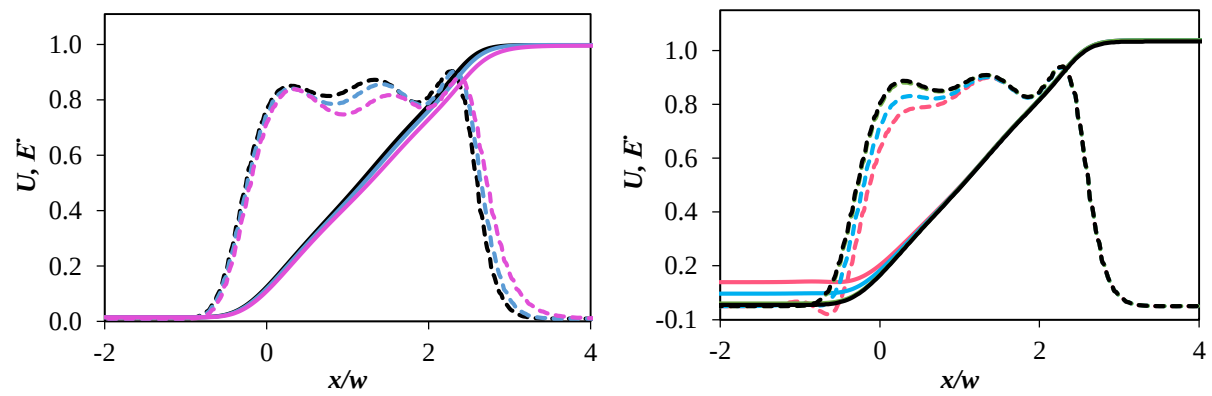

(d) 3D_AR1_2.5w

Figure 3.5 – Normalized velocity and deformation rate along the centerline of the FFD ($y = 0$, $z = h/2$) for different flow conditions: in the left plots, $VR = 100$ and Re was the variable parameter; in the right plots, $Re = 0.4$ and VR was the variable parameter. The legend presented in plots (a) is also valid for the other plots.

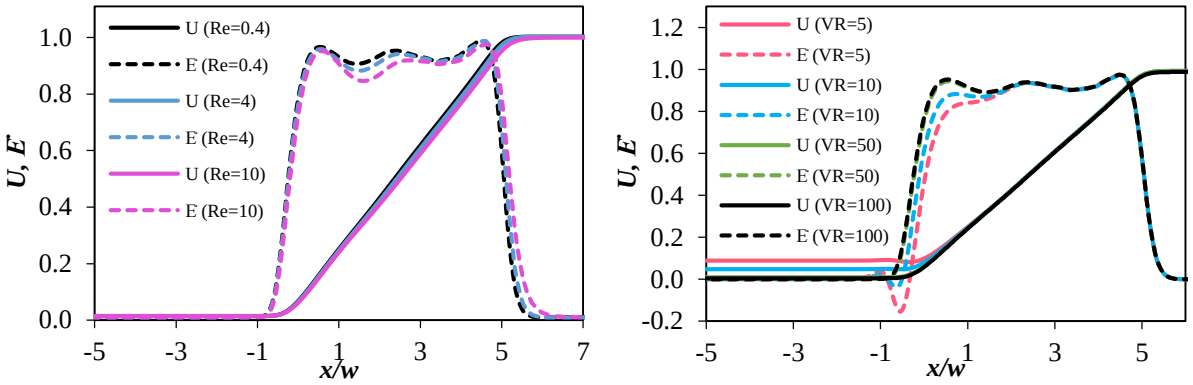

(e) 3D_AR1_5w

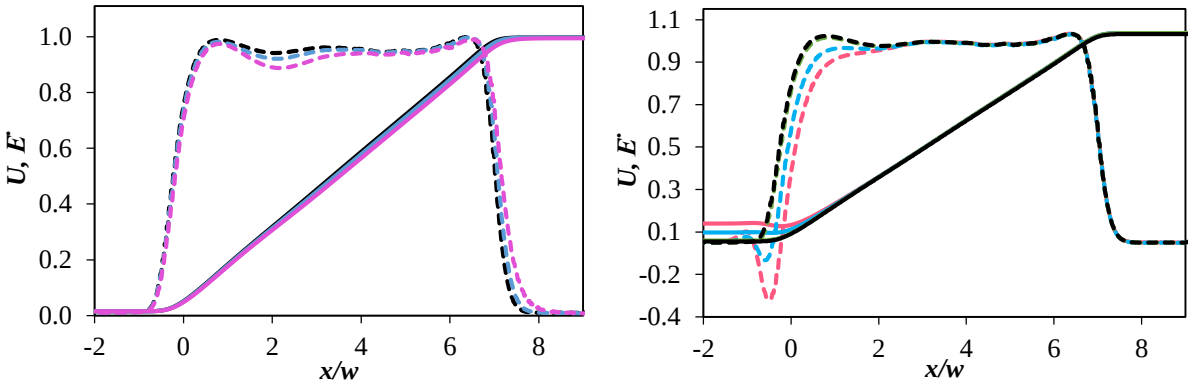

(f) 3D_AR1_7w

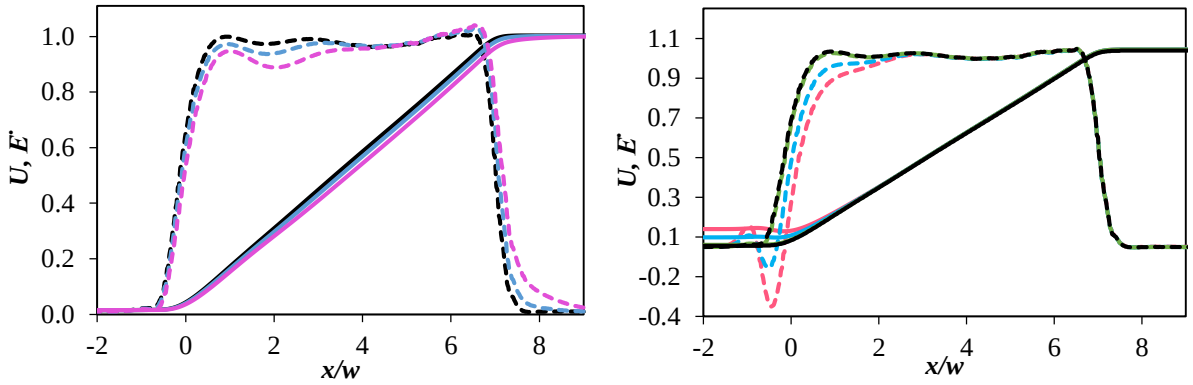

(g) 3D_AR2_7w

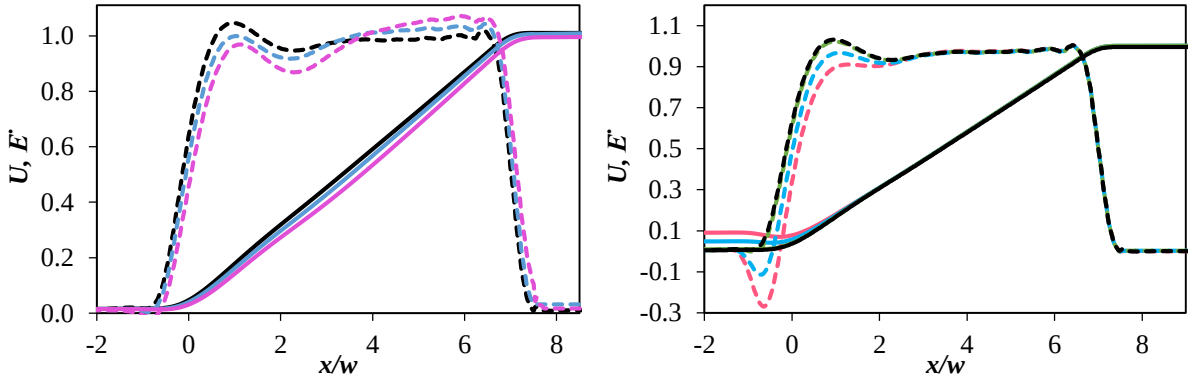

(h) 3D_AR4_7w

(Figure 3.5 continuation)

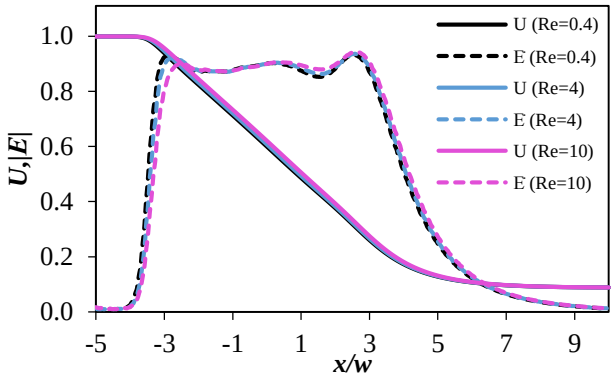

(i) 3D_AR1_exp

(Figure 3.5 conclusion)

A common feature to all the optimized geometries obtained in this work (both 2D and 3D configurations) is a velocity overshoot at the entry/exit to/from the extensional flow region. Furthermore, when the prescribed length of the FFD decreases, the homogeneity of the deformation rate profile also decreases, since the optimized length is closer to the length required by the velocity profile to start its rise and achieve fully-developed conditions. Thus, imposing a linear velocity profile in a short region leads to poorer results, although a quasi-linear velocity profile is still observable (Figure 3.5(c)-(f)). A device with a short extensional region has two main advantages: higher magnifications are possible in shorter areas, which is useful for optical methods; lower velocities (*Re*) are required to achieve the same deformation rate when compared with a longer channel (or higher deformation rates are possible for the same flow rates).

As found for the 2D geometries, the range for acceptable results is also fixed at $Re < 10$ (see Figure A.4 for results at $Re = 50$) and $VR > 5$. The sensitivity to both *Re* and *VR* seems to increase for higher *AR*.

The shape of the optimized expansion geometry, Figure 3.4(i), approximates a hyperbola. In this case, the transition of the velocity profile at the exit of the expansion is very smooth (Figure 3.5(i)). This is a direct consequence of the cost function that was used. Indeed, the residuals minimization only ensures that the deformation rate has a constant value in the region: $-3.5 < x/w < 3.5$ ($l = 7w$), previously defined. Beyond these limits, the velocity profile is not controlled by the cost function. However, since the channel keeps a constant cross-sectional area outside the optimized region, the transition from/to a constant velocity is ensured. However, the length along which that transition occurs is not under the control of the cost function and depends essentially on the channel width, leading to smoother transitions for larger channels. From this point of view, fitting the velocity profile to a target profile both inside and

outside the optimized region may minimize these problems, although the linearity of the velocity profile in the optimized region may be compromised to reduce the error outside that region.

Since optical techniques usually have a limited depth of field (in the *z*-direction in our case) and other techniques are simply unable to perform a differential sampling on that direction (as birefringence measurements in its most basic form), it is important to assess the velocity and deformation rate variation along this direction. This was performed for the geometries with $l = 7w$, for three distinct aspect ratios, Figure 3.6.

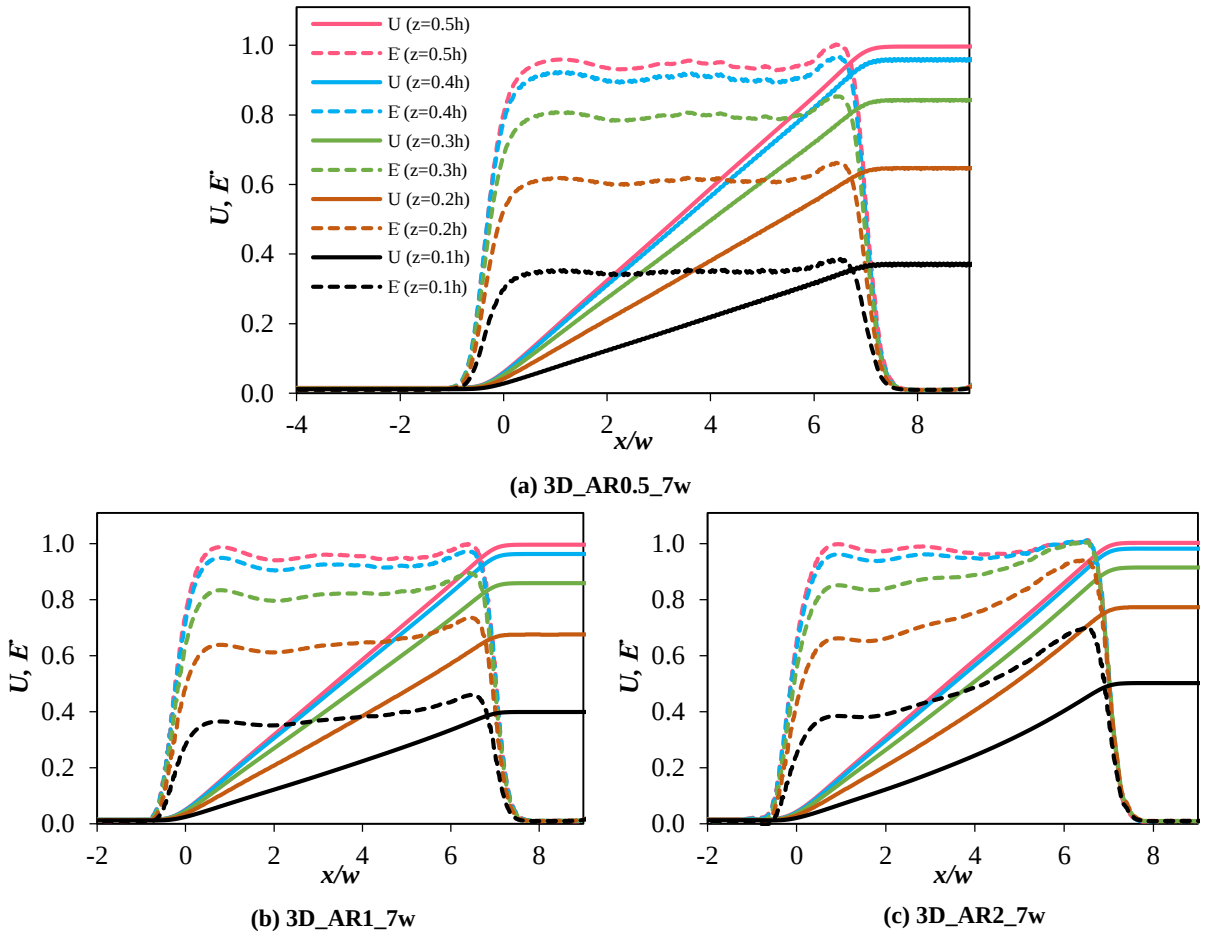

Figure 3.6 – Normalized velocity and deformation rate along the centerlines at $y = 0$ and different z positions for three different aspect ratios (devices): (a) $AR = 0.5$, (b) $AR = 1$ and (c) $AR = 2$. The legend presented in plot (a) is also valid for the other plots.

Two major conclusions arise from the analysis of Figure 3.6. Firstly, an acceptable variation of less than 10 % is observed in the deformation rate plateau when sampling at no more than $\pm 0.1h$ from the center plane, for all the AR tested. For instance, this is equivalent to a slice of 10, 20 and 40 μm, at $AR = 0.5$, 1 and 2, respectively, for a typical microchannel with 100 μm width arms. Although it depends on the specific application, the values of the previous example would be appropriate for μ-PIV measurements. Secondly, the velocity and

deformation rate profiles are distorted when *AR* increases. This seems to be a direct consequence of the plug flow orientation along the FFD. In the entry to the flow-focusing region, the local aspect ratio is low, even when the general *AR* (measured at the inlet of the central channel) is 2, since the width of the channel is locally large. Thus, the velocity profile has a small gradient in the cross-stream direction (direction of the larger dimension). Moving to the exit of the FFD, at $x/w = 7$, for $AR = 0.5$ the larger dimension is still the channel width. However, for $AR = 2$, the larger dimension becomes the depth and, consequently, the velocity gradient decreases in the *z*-direction. In this way, when moving from $x/w = 0$ to $x/w = 7$ the local aspect ratio increases and, at the same *z*- position, the relative difference of the local velocity to the mid-plane velocity decreases. For this reason, the deformation rate (derivative of the velocity) at a given *z*-position must increase (along the *x*-position) faster than at the centerline. This effect is less pronounced for $AR < 1$, as shown in Figure 3.6.

When formulating the problem addressed in this work (see section 1.4), it was argued that an analytical solution to the optimal shape of the FFD would probably be influenced by entry and exit effects. This was confirmed, after the derivation of an analytical solution for the channel width as a function of the *x*-position, computed from the expression for the fully-developed velocity in a channel with rectangular cross-section (see Appendix B). The upstream corner of the geometry resulting from the analytical solution has been made the same as for the numerical solution, at a given VR.

As can be seen in Figure 3.7, the analytical solution performs worse than the numerical solution for all *AR*. The simple analytical expression is not able to predict adequately the velocity profile close to entry to the flow-focusing region ($x/w = 0$) and at the exit region of the device ($x/w = 7$). At the inlet to the flow-focusing region, the *y*-velocity component and wall effects by the side arms seem to explain the discrepancy, while, at the outlet, the high velocity gradients could be the major cause. However, as a first approach, the simple equation that was derived would be a reasonable solution to the problem, especially for devices with high *AR* and high l/w.

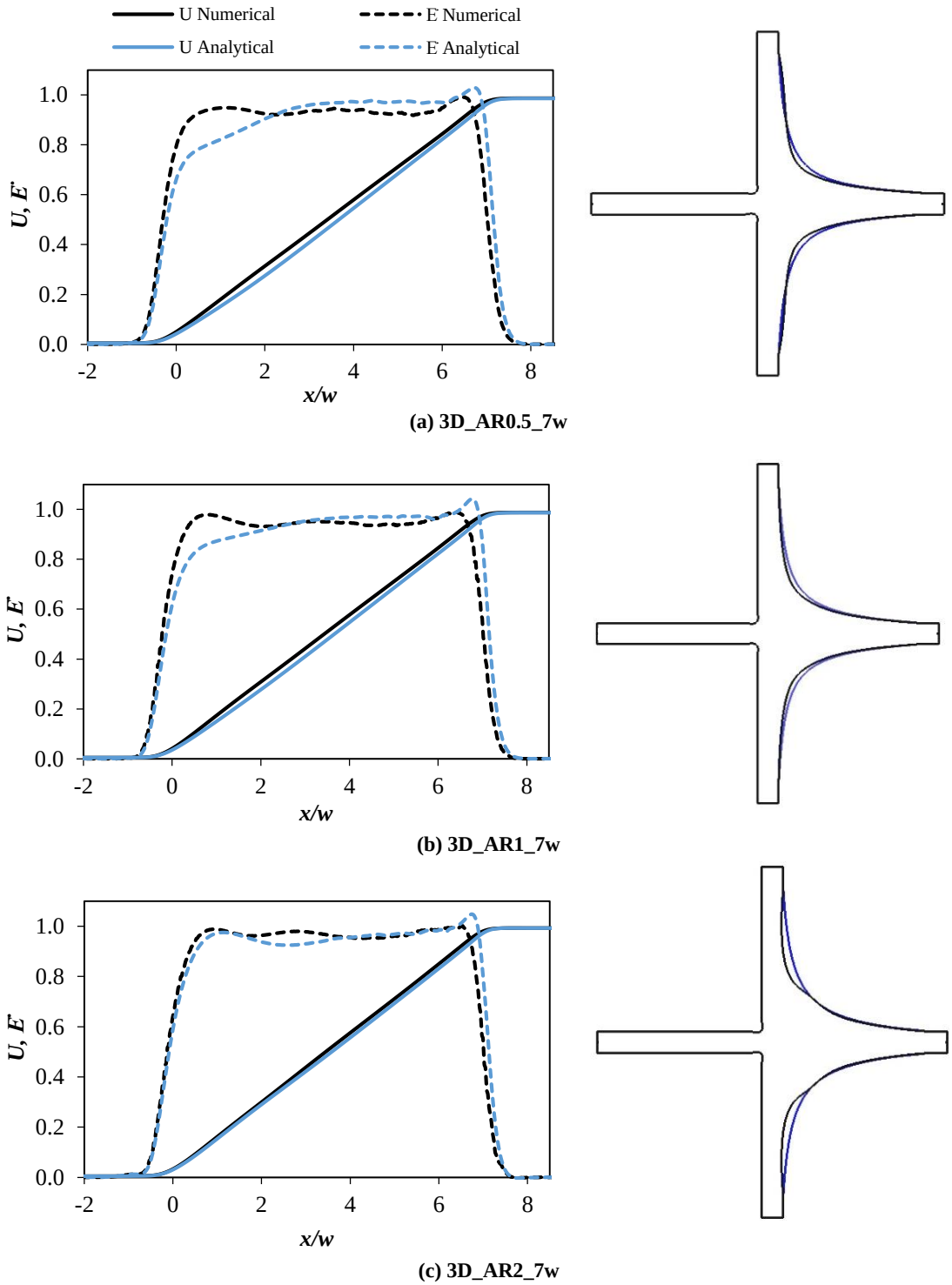

Figure 3.7 – Normalized velocity and deformation rate along the centerline, at *VR* = 100 and *Re* = 0.4 for the numerical and analytical solution at different aspect ratios: (a) *AR* = 0.5, (b) *AR* = 1 and (c) *AR* = 2. The corresponding shapes are depicted next to the profiles (black line – numerical solution; blue line – analytical solution). The legend presented in (a) is also valid for the other plots.

3.2 –Experimental validation

Simulation results at different *Re* and *VR* conditions were successfully validated through μ-PIV experiments, for the selected geometries, as shown in Figure 3.8. For example,

the change of the dimensionless velocity profiles for increasing *Re* is clearly observed in Figure 3.8(b), both for simulation and experimental results. Thus, the performance of the optimized devices was also demonstrated experimentally in this work.

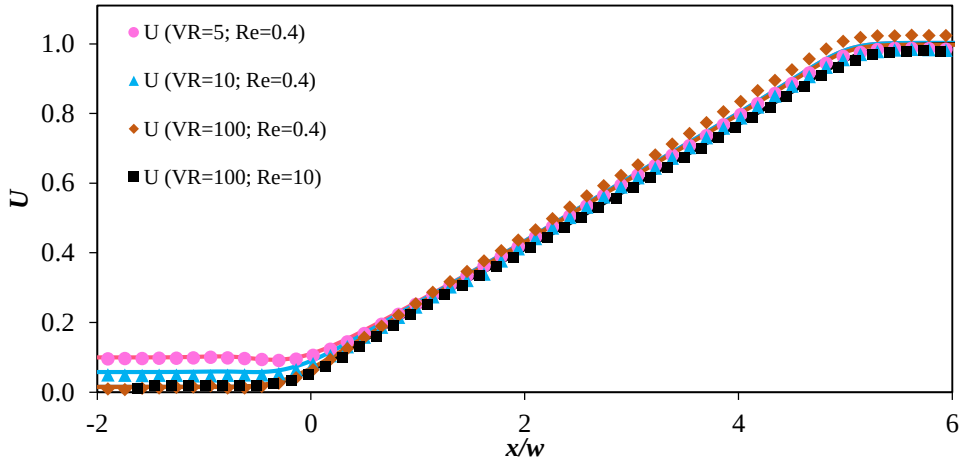

(a) 3D_AR1_5w

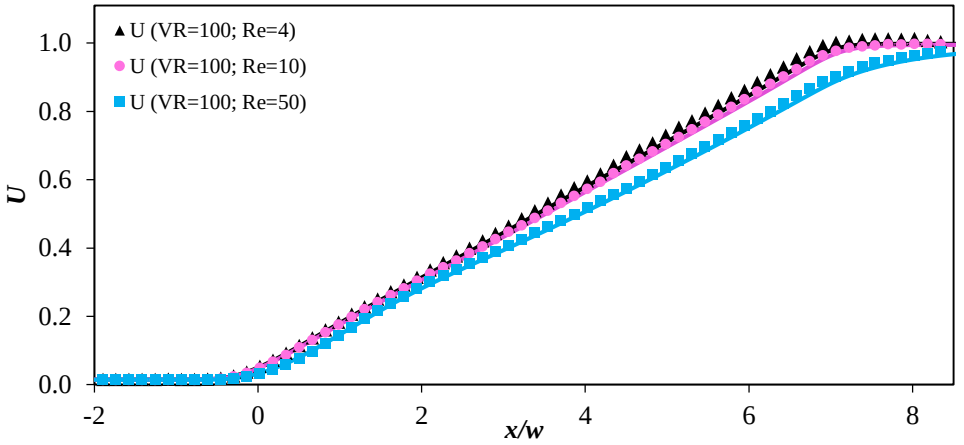

(b) 3D_AR1_7w

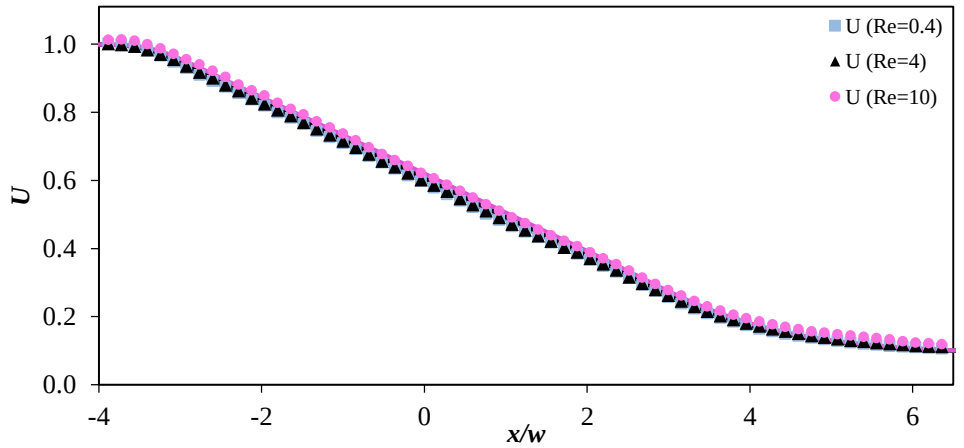

(c) 3D_AR1_exp

Figure 3.8 – Experimental (points) and predicted (continuous lines) dimensionless velocity along the centerline in three different geometries: (a) 3D_AR1_5w, (b) 3D_AR1_7w and (c) 3D_AR1_exp.

3.3 –Viscoelastic flow simulations

The simulation of viscoelastic flows was performed for the 2D geometry optimized at *VR* = 100 through the residuals minimization cost function (Eq. 2.3). The region of constant deformation rate in the FFD is of particular interest for the measurement of the extensional viscosity of viscoelastic fluids if it remains unchanged up to *We* = 0.5, since significant molecular extension starts at this *We*. The dimensionless velocity and first normal stress difference profiles are shown for 0.1 < *We* < 0.5, in Figure 3.9, corresponding to an Oldroyd-B model with a solvent viscosity ratio β = 8/9, which is adequate to model a dilute polymer solution.

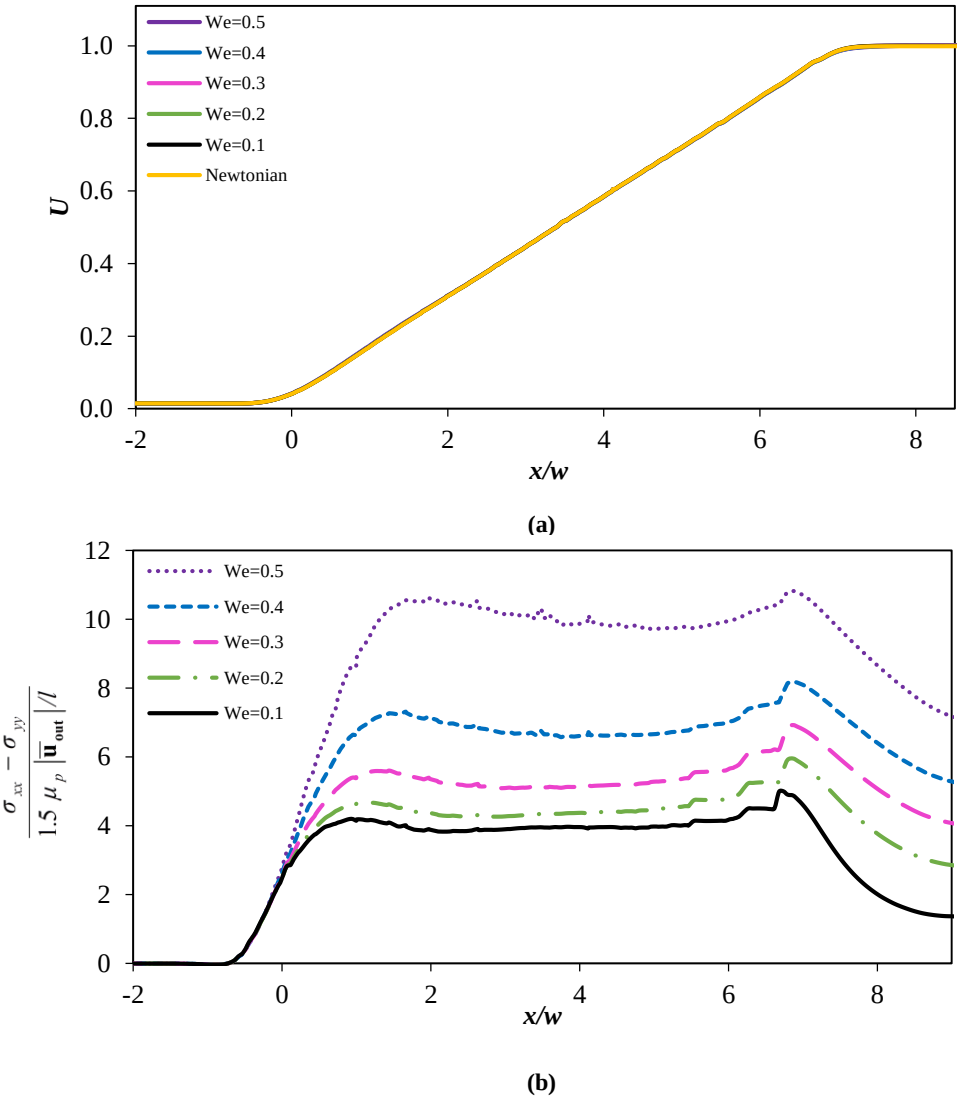

Figure 3.9 – (a) Dimensionless velocity and (b) first normal stress difference profiles, at the centerline of the optimized FFD (2D_7w geometry, optimized at *VR* = 100 through the residuals minimization), for different *We* (Oldroyd-B, *VR* = 100, *Re* = 0.18, β = 8/9). The high frequency oscillations in the first normal stress difference profiles are due to the poor mesh quality at the centerline when the whole geometry is meshed.

The linear velocity profile observed for the Newtonian case remained essentially unchanged in the viscoelastic conditions that were tested. Only a minor increase in the deformation rate overshoot at $x/w \approx 1$ is detectable when *We* increases. A consistent increase in the first normal stress difference is observed when *We* increases, which is due to the significant increase of the normal stress in the flow direction and simultaneous decrease of the normal stress in the normal direction to the flow. The plateau of the first normal stress difference profile is attained further downstream for higher *We* (Figure 3.9(b)), since the polymer time response is slower when the coil-stretch transition is approached. The same effect may be observed at the exit of the FFD, when the polymer molecules relax. At the experimental level, an excess pressure drop would be measurable and, as the deformation rate is well-defined and known in the plateau, an apparent extensional viscosity would be easily computed as: $\mu_e = (\sigma_{xx} - \sigma_{yy})/ \dot{\varepsilon}$ (Haward *et al.*, 2012b), which renders the optimized FFD a promising micro-rheometer. Additionally, birefringence measurements may instead be employed to measure the first normal stress difference and estimate the extensional viscosity, due to the expected birefringence strand that is developed at the centerline of the device (see the first normal stress difference contour plot at $We = 1.7$ in Figure A.6). However, it should be reminded that the Hencky strain in a FFD is limited and it is not possible to measure the steady-state extensional viscosity of some polymer solutions with a high relaxation time – the normal stress difference plateau may not be reached. Macroscopic rheometers may be more suitable in those cases, although the major challenge is on handling polymer solutions with low relaxation time, for which a micro-scale FFD is a good solution.

Since there is no stagnation point along the centerline of a FFD, the normal stresses are bounded and the Oldroyd-B constitutive equation is numerically stable even for $We > 0.5$ (the upstream edge rounding in the device also contributed to the numerical stability of the simulations). The onset of a steady bifurcation asymmetry was observed at $We = 1.7$, Figure 3.10. A similar trend was observed by Oliveira *et al.* (2009) in a standard flow-focusing device, at $We = 0.3$-0.4, for the Upper-convected Maxwell (UCM) model. The authors argued that the symmetry breaking could arise due to the increase in the energy dissipation, leading to the stabilization of the system. However, it should be noted that in the referred study, a different constitutive model was used (the solvent viscosity was not included) and inertial effects were switched-off. Thus, the instabilities depicted in Figure 3.10 may have a small inertia contribution, which should be considered as a topic of future investigation.

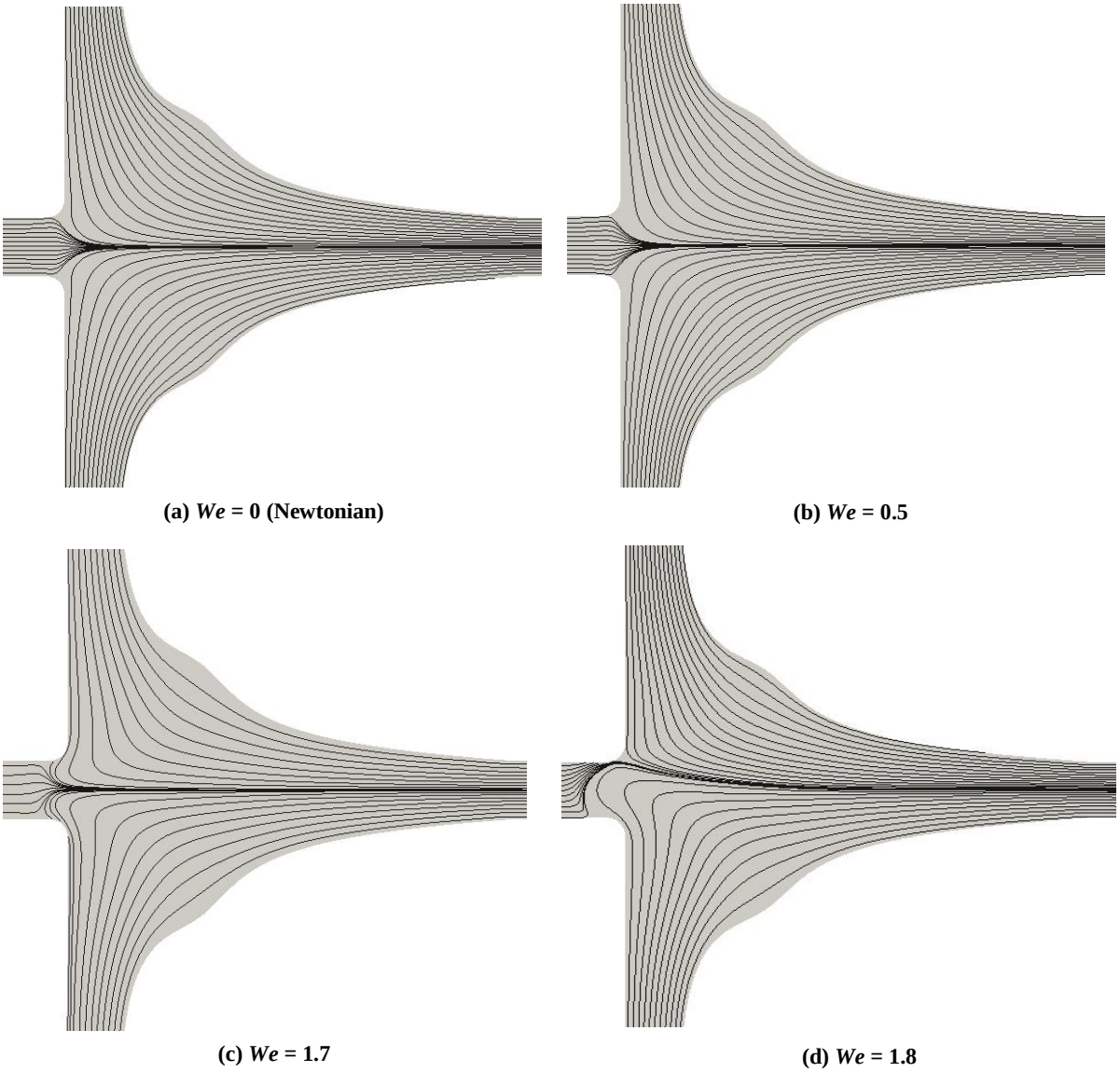

(a) *We* = 0 (Newtonian) **(b) *We* = 0.5**

(c) *We* = 1.7 **(d) *We* = 1.8**

Figure 3.10 – Streamlines in the 2D optimized FFD device (2D_7w geometry, optimized at *VR* = 100 through the residuals minimization) at different *We* (Oldroyd-B, *VR* = 100, *Re* = 0.18, β = 8/9). A steady symmetry breaking flow instability is observed in cases (c) and (d).

3.4 –Brownian dynamics simulations

The results of Brownian dynamics simulations for λ-DNA are presented in this section for the 3D_AR1_7w FFD geometry with a symmetric expansion at the outlet (herein named as double 3D_AR1_7w).

As previously mentioned, a FFD is only conditionally able to impose a steady stretching state on molecules. When a macromolecule travels along the centerline, the accumulated strain increases until it reaches a maximum value at the exit of the contraction zone, Figure 3.11. The Hencky strain evolution along the *x*-direction follows a logarithmic function: it presents an initial region of fast variation (where the velocity is low) and

progressively slows down (the rate of change is inversely proportional to the distance from the starting position). The maximum accumulated strain at the centerline depends theoretically only on the *VR* parameter in a FFD whose arms have the same width. In this way, *We* can be easily changed at a same Hencky strain by simply varying the total inflow in the device, keeping constant the *VR*. This represents a major advantage of FFD over microcontractions, since the latter are only able to impose a fixed (geometry-dependent) Hencky strain. Furthermore, controlling the Hencky strain is more rigorous and easy in a FFD than, for example, in a cross-slot device, where limiting the residence time of a molecule at the stagnation point is not a straightforward task. However, it should be noted that the accumulated strain actually depends on the specific trajectory of the molecule, particularly in the terminal zone of the expansion region of the FFD, where a molecule may follow several paths (three outlets are theoretically available).

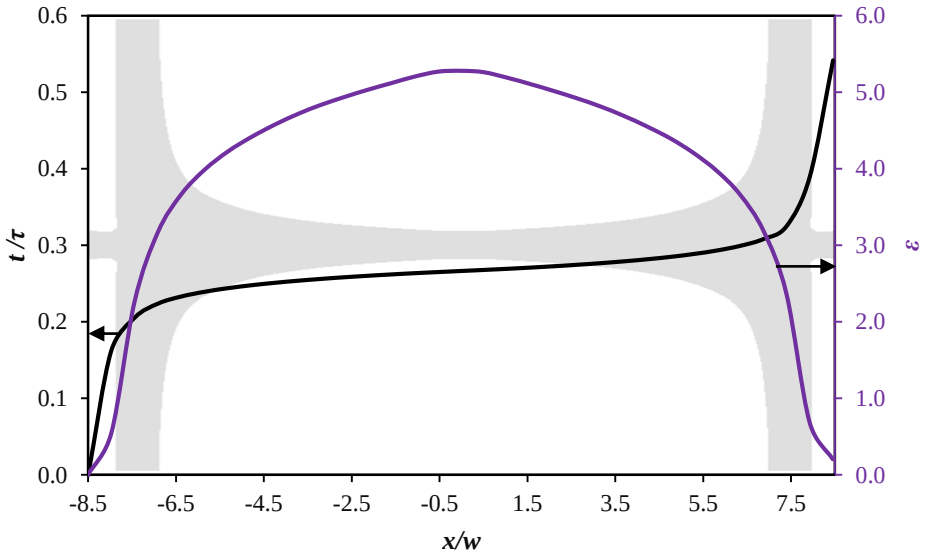

Figure 3.11 – Accumulated strain $\left(\varepsilon(x/w) = \sum_{s=-8.5}^{x/w} \dot{\varepsilon}_{xx}(s)\,\Delta t \right)$ and travelling time of a molecule advected along the centerline of the device (double 3D_AR1_7w geometry, *VR* = 100, *We* = 50). Both profiles were numerically computed.

In order to evaluate the capability of the optimized FFD to stretch λ-DNA molecules close to their contour length, two tests were performed at different accumulated strains: *VR* = 10 (ε = 3.0 at the centerline, for -8.5 < *x/w* < -0.5) and *VR* = 100 (ε = 5.3 at the centerline, for -8.5 < *x/w* < -0.5), Figure 3.12. In addition, for each *VR* different flow strengths were tested by changing *We* from 0.2 to 150. This was achieved by multiplying the velocity field simulated at *Re* < 1 (and for the given *VR*) by the factor required to scale the nominal deformation rate at the

centerline to We/τ. This is a good approximation provided that the assumption of creeping flow remains valid.

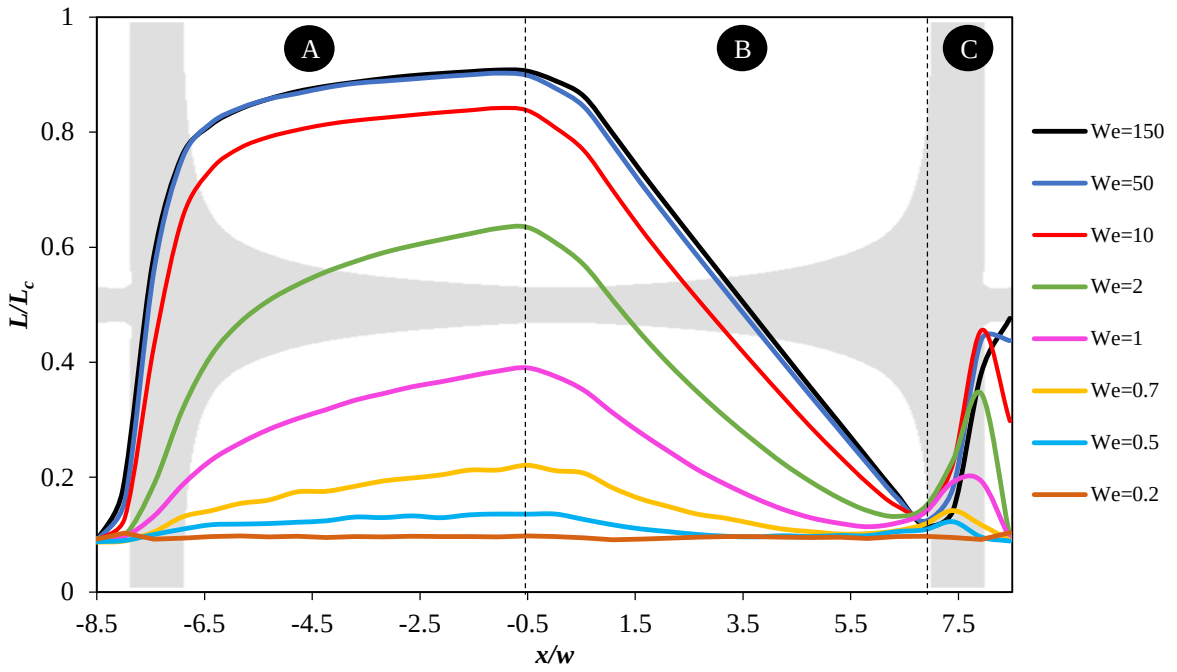

(a) *VR* = 100

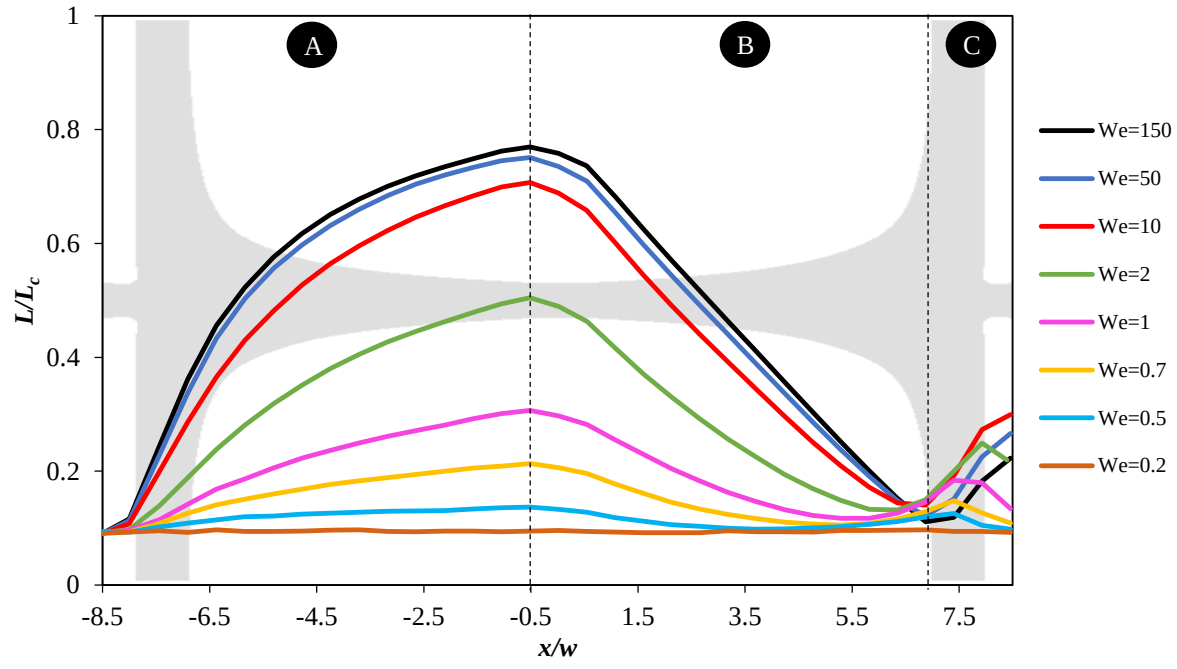

(b) *VR* = 10

Figure 3.12 – Average fractional length of λ-DNA computed in the double 3D_AR1_7w geometry for two different velocity ratios/Hencky strains: (a) *VR* = 100 and (b) *VR* = 10. Note that the two symmetric FFD are linked by a straight channel located between x/w = -0.5 and x/w = 0.5 (this was required to allow the flow to develop in the transition region, in order to have a symmetric velocity profile with relation to x/w = 0). Three regions may be identified based on the molecular length evolution: region A (-8.5 < x/w < -0.5), region B (-0.5 < x/w < 7) and region C (7 < x/w < 8.5). See an example of individual results in Figure A.7.

Three different regions are distinguishable in Figure 3.12: a first zone of stretching (region A: -8.5 < *x/w* < -0.5); a relaxation zone (region B: -0.5 < *x/w* < 7); a second zone of stretching (region C: 7 < *x/w* < 8.5). Starting the analysis by the first stretching region (A), the maximum fractional length increases with the increase of *We* and a higher stretch was achieved for the higher *VR* (strain) tested, as expected. However, a question remains: is the peak fractional length observed at *x/w* = -0.5 in Figure 3.12, for the several flow strengths, the maximum that could be attained at such *We*? The answer to that question requires a definition for the maximum expected stretch. In a first approach, a DNA molecule may be considered as an element of fluid, thus being exponentially deformed as that element (from the definition of Hencky strain): $L = L_0 \exp(\varepsilon)$. In this case, the molecule is said to be under an "affine" deformation (Larson & Hu, 1999) and would be extended until its contour length, independently of *We* (which is not physically admissible). In a second approach, a simple dumbbell model is considered. The governing equation may be derived from Eq. (2.10) by considering the balance of only two forces: the drag and the spring force. The resulting equation may then be presented in a convenient form (Trahan & Doyle, 2009):

$$\frac{d}{d\varepsilon}\left(\frac{L}{L_C}\right) = \frac{L}{L_C} - \frac{1}{3We}\left[\frac{1}{4\left(1-\frac{L}{L_C}\right)^2} - \frac{1}{4} + \frac{L}{L_C}\right] \tag{3.1}$$

For a given *We*, the previous equation can predict the evolution of the dumbbell length as it accumulates strain. Its asymptotic value, for an infinite strain, corresponds to the maximum, steady length of the dumbbell. Also note that Eq. (3.1) is written in a form that clearly evidences why it is difficult to stretch a molecule at low *We*, as well the role of the spring term as an extensional break (note that if only the first right hand side term is considered, the model reduces to an affine deformation). The fractional length evolution predicted by the two previous models is plotted in Figure 3.13 together with the Brownian dynamics simulation results at *VR* = 100, for two different *We*.

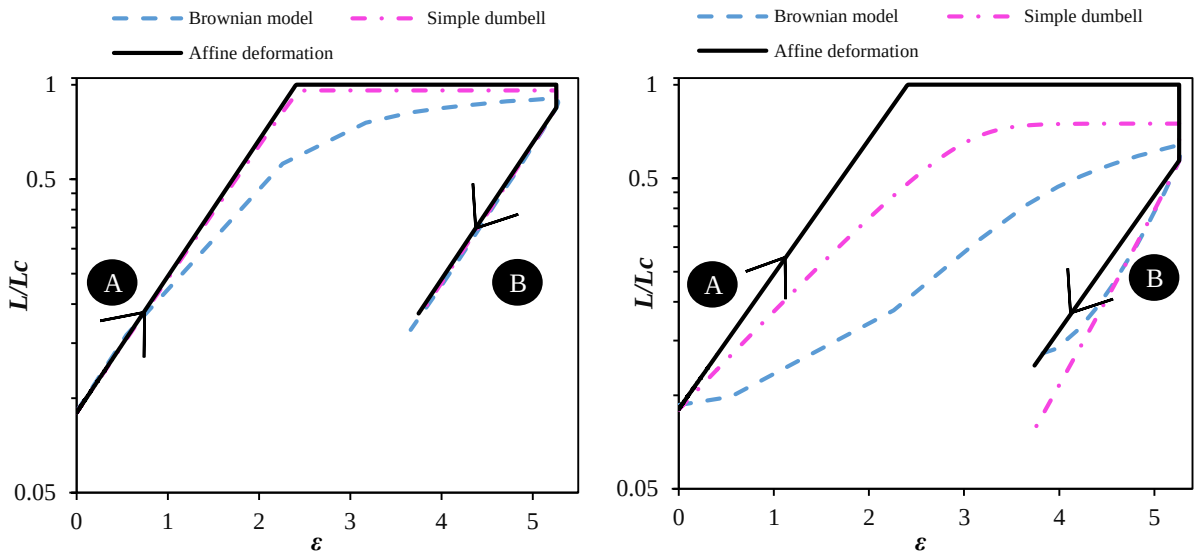

Figure 3.13 – Fractional length as a function of the accumulated strain in the double 3D_AR1_7w geometry, at *VR* = 100, predicted using different models (see the explanation in the text). The arrows point the evolution of the strain, which is related with the region in the double FFD (see the corresponding region, identified by letters, in Figure 3.12). The transition between regions A and B occurs at $\varepsilon \approx 5.3$. The affine deformation curve was shifted vertically in the transition between regions A and B in order to match the fractional length predicted by the Brownian model at the exit of the free relaxation region, which facilitates the slope comparison (this was necessary because the affine deformation equation is not able to correctly predict the free relaxation).

At *We* = 50, the simple dumbbell model predicts a quasi-affine stretching. However, for the Brownian model that was used, the quasi-affine deformation is only seen while $L/L_c <$ 0.2. For larger molecular extension, the Brownian dynamics simulation results also deviate from the dumbbell model. This is a consequence of molecular individualism: some molecular conformations are more prone to become fully stretched than others (de Gennes, 1997; Larson & Hu, 1999), which is not considered in the dumbbell model. Indeed, some molecules start the Brownian simulation in a folded or kinked state and are not able to unfold, even in strong flows (Figure A.8 and A.9). There are also intermediate cases where the stretching curve is composed of successive plateaus that clearly identify the unfolding process (Figure A.10). Thus, the maximum averaged stretch in Brownian simulations does not reach the value predicted by the dumbbell model (a difference of 6 % is observed). At *We* = 2, the stretching is never affine and the difference to the steady stretch in the dumbbell model is even higher (15 %). This reflects a higher unfolding difficulty in flows of lower strength. Similar results were obtained by Larson & Hu (1999), who observed that at *We* > 10, the deformation is affine while *L/Lc* < 1/3 and that the initial molecular conformation is the main responsible for this behavior.

From these results, it seems that the strain imposed at *VR* = 100 is not enough to reach the steady extension of λ-DNA. However, only a minor elongation would result at a higher *VR*,

due to molecular individualism. Furthermore, increasing the *VR* at a constant *Re* leads to an undesirable throughput reduction. The same conclusions may be extended to the simulations at *VR* = 10, with the only difference that the molecular length remains even further away from the contour length. It is worth to note that the theoretical homogeneous extensional flow field analytically reproduced in single-molecule studies (defined through a constant deformation rate, both in the *x* and *y*-directions) is nearly observed at the centerline of the optimized FFD, which shows the potential of the device for the experimental validation of simulated results, under controlled and tunable conditions.

Proceeding on the analysis of Figure 3.12, the molecular relaxation (region B) is composed of two phases: a free relaxation ($-0.5 < x/w < 0.5$) where there is no velocity gradient in the streamwise direction (at the straight channel connector) and a forced relaxation ($0.5 < x/w < 7$) where the velocity gradient takes negative values. More rigorously, the end of region B is not fixed, but rather dependent on *We*, ending earlier at a lower *We*. As can be seen in Figure 3.13, the relaxation does not follows back the extension curve. This is because the spring force term does not opposes the velocity gradient, but, instead, enhances its action. From the moment the molecules are subjected to a forced relaxation, the length reduction is exactly affine (for both the Brownian dynamics and simple dumbbell models) at *We* = 50. Indeed, molecular individualism does not seem to play its role when molecules are compressed. However, since the Brownian model used allows the crossover between springs and because the drag coefficient is assumed to be independent of the stretching state of molecules, some degree of inaccuracy exists. At *We* = 2, the Brownian model predicted a higher than affine compression, which is due to the spring force term, whose importance is weighted by $1/We$ (*We* is negative in a forced relaxation). The same holds for the simple dumbbell model. Note that the dumbbell model starts to deviate from the Brownian model at a low molecular length (Figure 3.13), since equilibrium events (exclusion volume and Brownian forces) become more important.

Region C of Figure 3.12 is of more complex analysis due to the existence of multiple concurrent phenomena. Indeed, in this region the streamlines diverge to the three outlets and this event is able itself to elongate molecules until some extent (Figure A.11), while there is also a non-homogeneous velocity gradient in the streamlines' direction. It was observed that at a low *We* ($We < 10$), a high number of molecules exited the device in a coiled state through the side arms, while at a higher *We* the molecules showed a tendency to be stretched (and oriented) in the *y*-direction and exited the device through the central arm (results not presented for conciseness). A possible explanation may be that, at a low *We*, the flow is not strong enough to

perfectly align molecules at the centerline. In association with the Brownian motion, any minor displacement in the *y*-direction is able to entrain the molecules to the lateral arms. On the other hand, at a higher *We*, the molecules are kept at the centerline, since the bends that result from the molecule compression develop symmetrically above and below the centerline, at least until the point where the streamlines only direct to the central arm (even if there is displacement in the *y*-direction). Still, it is possible that this observation was an algorithm artifact originated by the small velocity field asymmetry arising from the unstructured mesh that was used, from the accuracy of the interpolation scheme (cell-to-faces velocity field interpolation) or/and from the OpenFOAM limited accuracy when solving for the flow. This point needs further analysis to be done in the future.

The maximal fractional length attained in the optimized FFD (at the exit of the contraction region) is depicted in Figure 3.14, as a function of the flow strength (*We*), for the two *VR* conditions that were tested. λ-DNA molecules were stretched from 9 % of its contour length to 84 % for *VR* = 100 and 71 % for *VR* = 10, when *We* increased from 0.2 to 10. However, only an additional increase of 6 % in the fractional length was achieved after further increasing *We* up to *We* = 150. Those results are in qualitative agreement with other works on DNA stretching in extensional flows (Huang *et al.*, 2014; Jendrejack *et al.*, 2002) and the deviation from the dumbbell model is due to the above-mentioned molecular individualism.

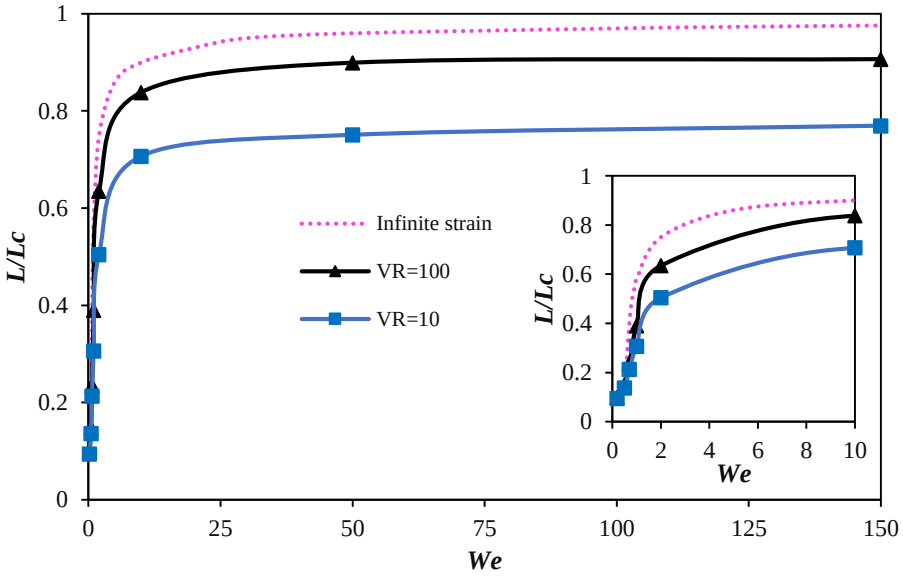

Figure 3.14 – DNA maximum averaged fractional length in the double 3D_AR1_7w geometry as a function of *We*, at different *VR*. The values were probed at the exit of the contraction region (*x/w* = -0.5), where the molecular elongation is maximum. The dotted line represents the stretch for an *infinite* Hencky strain (50 strain units), according to the simple dumbbell model (Eq. 3.1). The symbols represent the *We* at which simulations were performed (the connecting lines are only a guide to the eye). The inset is a zoomed view of the main plot at low *We*.

An efficient way to assess the extent of molecular individualism is through the analysis of the length distribution of stretched molecules, Figure 3.15. The simple dumbbell model would predict a single peak fixed at a given length, which is dependent on *We*. For Brownian dynamics simulations, the individual molecular lengths are distributed around an average value and several populations can be distinguished. It is clear from Figure 3.15 that the distribution becomes narrower as *We* is increased, but a single population is never attained. The delivery of homogeneous populations of DNA molecules is a fundamental requirement if the device is intended to be used, for instance, in a DLA (Chan *et al.*, 2004), since the reproducibility and accuracy of the method depend on it. However, care should be taken when interpreting simulation results, since in some cases only a qualitative agreement with experimental data was observed (Huang *et al.*, 2014; Trahan & Doyle, 2009).

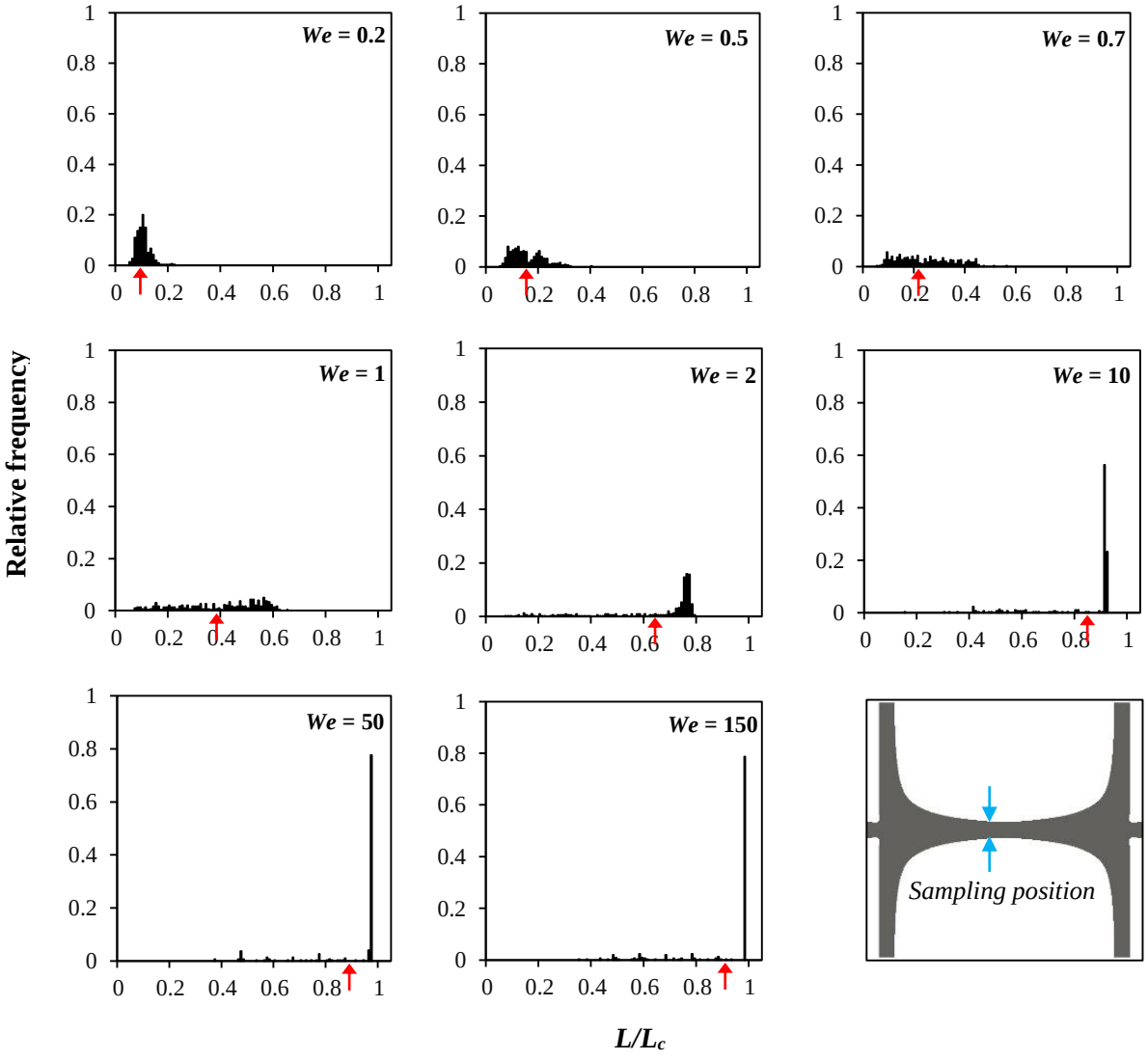

Figure 3.15 – Histogram of the fractional length at the exit of the contraction region of the double 3D_AR1_7w geometry (*x/w* = -0.5, as pointed out by the arrows in the scheme) for different *We*, at *VR* = 100. The arrows mark the averaged value, based on the simulation of 300 individual λ-DNA molecules.

In the previous sections, it was argued that in a standard FFD the flow can not be characterized by a unique *We* because the deformation rate is note homogeneous. This fact was confirmed in Brownian dynamics simulations and highlights the relative advantage of the optimized FFD. Indeed, in Figure 3.16 the fractional length is represented, both in a standard (also with 6 arms, Figure A.12) and in the optimized double FFD, at the same *We* (simulation results at *We* = 2 and *We* = 50) and for the same accumulated strain (*VR* = 100). The *We* was computed based on the deformation rate peak/plateau in each device (Figure 3.5(a) and (f)). In such conditions, the residence time of molecules in the extensional region of each device is nearly the same in both cases (the standard FFD has a shorter extensional region, but has also a proportionally lower velocity than the optimized device, in order to generate the same deformation rate).

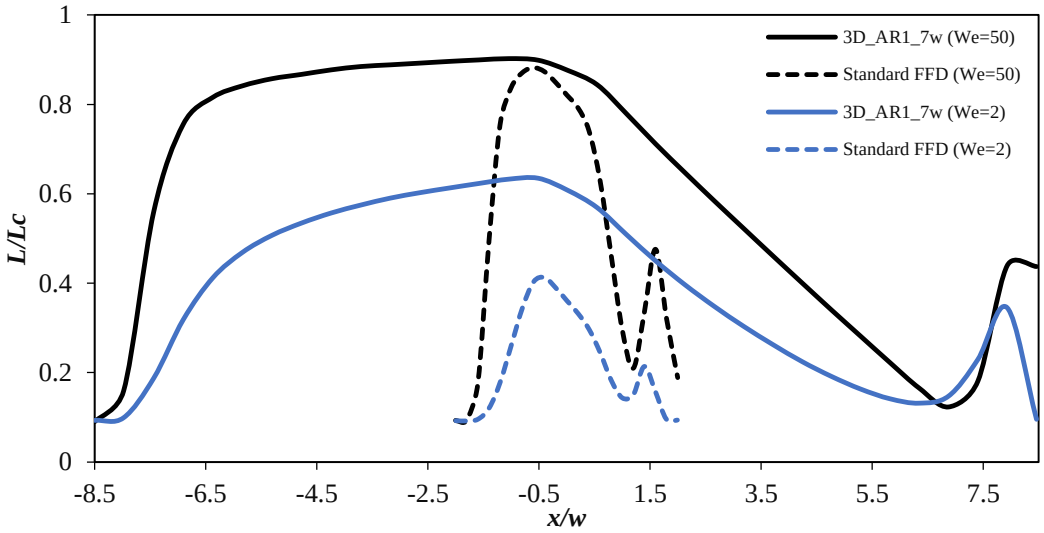

Figure 3.16 – Average fractional length in the optimized double 3D_AR1_7w FFD and in a standard double FFD, at *VR* = 100, for *We* = 2 and 50.

At *We* = 50, the maximum stretch is only 1 % higher in the optimized FFD, than in the standard FFD. However, at *We* = 2 the difference increases to 38 %. Those results are a direct consequence of the deformation rate profile of each device (Figure 3.5(a) and (f)): when performing the integration of the deformation rate along the *x*-axis and dividing the result by the length of the extensional region, an average deformation rate 55 % and 6 % lower than the peak deformation rate is observed for the standard and optimized devices, respectively. Thus, it could be stated that a peak *We* = 2 (50) in the standard device is nearly equivalent to a plateau *We* of 1.2 (29) in the optimized device (which is only 6 % higher than the average *We* value). This equivalence could be anticipated from Figure 3.12 and 3.14, where a maximum fractional length of 41 % (the value observed in the standard FFD, at *We* = 2) was nearly achieved at *We*

= 1 in the optimized FFD. The difference between the two devices was less noticeable at *We* = 50, because in that case the average *We* in the standard device (<*We*> = 29) was still sufficiently high to impose nearly the same molecular stretch, since the fractional length increase is small when changing from *We* = 29 to *We* = 50 (Figure 3.14). In summary, two main conclusions emerge: (1) an higher *We* is required in the standard FFD in comparison with the optimized FFD to achieve the same average fractional length and (2) the extensional deformation experienced by molecules in the standard FFD is considerably more heterogeneous than in the optimized FFD, making the analysis of the extensional deformation of molecules easier for the flow-focusing devices optimized in this work.

4 – Concluding remarks and suggestions for future work

The main goal of this work was to optimize the shape of a FFD in order to increase the length and the homogeneity of the resulting extensional flow. This goal was successfully achieved using exclusively open-source tools. Several devices were numerically optimized, in both 2D and 3D configurations, with different aspect ratios and different lengths of the extensional flow region. The optimized FFD are able to generate a homogeneous extensional flow for $Re < 10$ and $VR > 5$, although some specific geometries also performed acceptably well beyond those limits. The simulated velocity profiles at the centerline were confirmed experimentally through μ-PIV measurements, for a selected set of microfluidic devices.

The superior performance of the numerically optimized geometries over the shapes arising from an analytical equation derived from the expression for the fully-developed velocity profile in a rectangular duct was also demonstrated. However, this superiority becomes less relevant for devices with large aspect ratios. Several improvements or alternatives could also be implemented. For example, the same channel width was considered for all the arms of the device, but several combinations could have been tested. The velocity overshoot observed at the entrance to the flow-focusing region may eventually be minimized by changing the width of the arms and performing a new optimization. Note that changing the width of the side channels will affect qualitatively the velocity profile at the centerline, even if the velocity is adjusted to keep the same flow rate ratio between the central and side arms. The use of a different optimization approach, such as topological optimization, should also be considered, as well as changing the type of curve used to parameterize the edge of the device (using B-splines, for example).

A limited number of viscoelastic flow simulations were made with a 2D optimized geometry, for different flow strengths. The linearity of the velocity profile remained nearly unchanged for $We \leq 0.5$. A symmetry breaking steady flow bifurcation was also observed, but only for $We \geq 1.7$, using the Oldroyd-B model. Those results illustrate the great potential of the optimized shapes to be used as micro-rheometers. Testing the performance and stability of the optimized 3D geometries in viscoelastic flows, as well the influence of the *AR* and *VR*, is left to future work on this subject.

The application of the optimized shapes in the controlled stretching of DNA molecules was also demonstrated through Brownian dynamics simulations, using λ-DNA as the model polymer. The maximum stretch attained at $VR = 100$ ($\varepsilon = 5.3$) was close to the value predicted for an infinite amount of strain and the difference (6 %) was attributed to molecular

individualism. Furthermore, the connection of two symmetrical FFD allowed to study the forced relaxation of DNA molecules. An interesting molecular orientation change was observed in this double FFD, which was attributed to the stream separation at the exit of the device. In addition, the arm selected by the molecules to exit the double device was shown to be dependent on *We*. However, future experimental studies are needed to validate the simulated results and the approximations that were assumed in the model as, for instance, the omission of hydrodynamic interactions.

References

Alves M.A. (2008) Design of a cross-slot flow channel for extensional viscosity measurements. In: *The XVth International Congress on Rheology, The Society of Rheology 80th Annual Meeting*. Editors: Leal L.G., Colby R.H., Giacomin A.J. (American Institute of Physics, Monterey).

Arratia P.E., Gollub J.P., Durian D.J. (2008) Polymeric filament thinning and breakup in microchannels. *Physical Review E* 77: 036309.

Audet C., Le Digabel S., Tribes C. (2009) NOMAD user guide. Technical Report G-2009-37, Les cahiers du GERAD.

Auhl D., Hoyle D.M., Hassell D., Lord T.D., Harlen O.G. (2011) Cross-slot extensional rheometry and the steady-state extensional response of long chain branched polymer melts. *Journal of Rheology* 55: 875.

Binding D.M., Walters K. (1988) On the use of flow through a contraction in estimating the extensional viscosity of mobile polymer solutions. *Journal of Non-Newtonian Fluid Mechanics* 30: 233–250. In: Ober T.J., Haward S.J., Pipe C.J., Soulages J., McKinley G.H. (2013) Microfluidic extensional rheometry using a hyperbolic contraction geometry. *Rheologica Acta* 52: 529–546.

Campo-Deaño L., Galindo-Rosales F.J., Pinho F.T., Alves M.A., Oliveira M.S.N. (2011) Flow of low viscosity Boger fluids through a microfluidic hyperbolic contraction. *Journal of Non-Newtonian Fluid Mechanics* 166: 1286–1296.

Chae S.K., Lee C.H., Lee S.H., Kim T.S., Kang J.Y. (2009) Oil droplet generation in PDMS microchannel using an amphiphilic continuous phase. *Lab on a Chip* 9: 1957–1961.

Chan E.Y., Gonçalves N.M., Haeusler R.A., Hatch A.J., Larson J.W., *et al.* (2004) DNA mapping using microfluidic stretching and single-molecule detection of fluorescent site-specific tags. *Genome Research* 14: 1137–1146.

Chuncheng Z., Feng J., Qianqian C. (2009) Electrophoretical stretching of DNA in a hybrid microchannel. *Polymer* 505: 5326–5332.

de Gennes P.G. (1997) Molecular individualism. *Science* 276: 1999–2000.

Dubash N., Cheunga P., Shen A.Q. (2012) Elastic instabilities in a microfluidic cross-slot flow of wormlike micellar solutions. *Soft Matter* 8: 5847–5856.

Dylla-Spears R., Townsend J.E., Jen-Jacobson L., Sohn L.L., Muller S.J. (2009) Single-molecule sequence detection via microfluidic planar extensional flow at a stagnation point. *Lab on a Chip* 10: 1543–1549.

Favero J.L., Secchi A.R., Cardozo N.S.M., Jasak H. (2010) Viscoelastic flow analysis using the software OpenFOAM and differential constitutive equations. *Journal of Non-Newtonian Fluid Mechanics* 165: 1625–1636.

Ferree S., Blanch H.W. (2003) Electrokinetic stretching of tethered DNA. *Biophysical Journal* 85: 2539–2546.

Galindo-Rosales F.J., Alves M.A., Oliveira M.S.N. (2013) Microdevices for extensional rheometry of low viscosity elastic liquids: a review. *Microfluidics and Nanofluidics* 14: 1–19.

Galindo-Rosales F.J., Oliveira M.S.N., Alves M.A. (2014) Optimized cross-slot microdevices for homogeneous extension. *RSC Advances* 4: 7799–7804.

Gossett D.R., Tse H.T.K., Lee S.A., Ying Y., Lindgren Y.G., *et al*. (2012) Hydrodynamic stretching of single cells for large population mechanical phenotyping. *Proceedings of the National Academy of Sciences of the United States of America* 109: 7630–7635.

Haward S.J., Jaishankar A., Oliveira M.S.N., Alves M.A., McKinley G.H. (2013a) Extensional flow of hyaluronic acid solutions in an optimized microfluidic cross-slot device. *Biomicrofluidics* 7: 044108.

Haward S.J., McKinley G.H. (2013b) Instabilities in stagnation point flows of polymer solutions. *Physics of Fluids* 25: 083104.

Haward S.J., Ober T.J., Oliveira M.S.N., Alves M.A., McKinley G.H. (2012a) Extensional rheology and elastic instabilities of a wormlike micellar solution in a microfluidic cross-slot device. *Soft Matter* 8: 536.

Haward S.J., Oliveira M.S., Alves M.A., McKinley G.H. (2012b) Optimized cross-slot flow geometry for microfluidic extensional rheometry. *Physical Review Letters* 109: 128301.

Hoath S.D., Vadillo D.C., Harlen O.G., McIlroy C., Morrison N.F., *et al*. (2014) Inkjet printing of weakly elastic polymer solutions. *Journal of Non-Newtonian Fluid Mechanics* 205: 1–10.

Hsieh C.C., Li L., Larson R.G. (2003) Modeling hydrodynamic interaction in Brownian dynamics: simulations of extensional flows of dilute solutions of DNA and polystyrene. *Journal of Non-Newtonian Fluid Mechanics* 113: 147–191.

Hsieh C.C., Lin T.H. (2011) Simulation of conformational preconditioning strategies for electrophoretic stretching of DNA in a microcontraction. *Biomicrofluidics* 5: 044106.

Hsieh S.S., Chen J.H., Tsai C.F. (2013) DNA molecule stretching through thermo-electrophoresis and thermal convection in a heated converging-diverging microchannel. *Nanoscale Research Letters* 8: 87.

Hsieh S.S., Liu C.H., Liou J.H. (2007) Dynamics of DNA molecules in a cross-slot microchannel. *Measurement Science and Technology* 18: 2907.

Huang C.D., Kang D.Y., Hsieh C.C. (2014) Simulations of DNA stretching by flow field in microchannels with complex geometry. *Biomicrofluidics* 8: 014106.

Ivorra B., Hertzog D.E., Mohammadi B., Santiago J.G. (2006) Semi-deterministic and genetic algorithms for global optimization of microfluidic protein-folding devices. *International Journal for Numerical Methods in Engineering* 66: 319–333.

Jendrejack R.M., de Pablo J.J., Graham M.D. (2002) Stochastic simulations of DNA in flow: dynamics and the effects of hydrodynamic interactions. *The Journal of Chemical Physics* 116: 7752–7759.

Jensen K.E., Szabo P., Okkels F. (2012) Topology optimization of viscoelastic rectifiers. *Applied Physics Letters* 100: 243102.

Jo K., Chen Y.L., de Pablo J.J., Schwartz D.C. (2009) Elongation and migration of single DNA molecules in microchannels using oscillatory shear flows. *Lab on a Chip* 9: 2348–2355.

Kim J.M., Doyle P.S. (2006) A Brownian dynamics-finite element method for simulating DNA electrophoresis in nonhomogeneous electric fields. *The Journal of Chemical Physics* 125: 074906.

Kramer O., Ciaurri D.E., Koziel S. (2011) Derivative-free optimization. *Computational Optimization, Methods and Algorithms Studies in Computational Intelligence* 356: 61–83.

Krogmeier J.R., Schaefer I., Seward G., Yantz G.R., Larson J.W. (2007) An integrated optics microfluidic device for detecting single DNA molecules. *Lab on a Chip* 7: 1767–1774.

Larson R.G., Hu H. (1999) Brownian dynamics simulations of a DNA molecule in an extensional flow field. *Journal of Rheology* 43: 267.

Larson J.W., Yantz G.R., Zhong Q., Charnas R., D'Antoni C.M., *et al.* (2006) Single DNA molecule stretching in sudden mixed shear and elongational microflows. *Lab on a Chip* 6: 1187–1199.

Larson R.G. (2005) The rheology of dilute solutions of flexible polymers: progress and problems. *Journal of Rheology* 49: 1–70.

Le Digabel S. (2011) Algorithm 909: NOMAD: Nonlinear optimization with the MADS algorithm. *ACM Transactions on Mathematical Software* 37: 44:1–44:15.

Lee J.S., Dylla-Spears R., Teclemariam N.P., Muller S.J. (2007) Microfluidic four-roll mill for all flow types. *Applied Physics Letters* 90: 074103.

Liu R., Wong T.S., Lau P.P.Z., Tomczak N. (2014) Stretching and imaging of single DNA chains on a hydrophobic polymer surface made of amphiphilic alternating comb-copolymer. *ACS Applied Materials & Interfaces* 6: 2479–2485.

Macpherson G.B., Nordin N., Weller H.G. (2009) Particle tracking in unstructured, arbitrary polyhedral meshes for use in CFD and molecular dynamics. *Communications in Numerical Methods in Engineering* 25: 263–273.

Marko J.F., Siggia E.D. (1995) Stretching DNA. *Macromolecules* 28: 8759–8770.

Minoshima W., White J.L. (1986) Instability phenomena in tubular film and melt spinning of rheologically characterised high density, low density and linear low density polyethylenes. *Journal of Non-Newtonian Fluid Mechanics* 19: 275–302. In: Auhl D., Hoyle D.M., Hassell D., Lord T.D., Harlen O.G (2011) Cross-slot extensional rheometry and the steady-state extensional response of long chain branched polymer melts. *Journal of Rheology* 55: 875.

Moré J., Wild S. (2009) Benchmarking derivative-free optimization algorithms. *SIAM Journal on Optimization* 20: 172–191.

Muyl F., Dumas L., Herbert V. (2004) Hybrid method for aerodynamic shape optimization in automotive industry. *Computers and Fluids* 33: 849−858.

Ober T.J., Haward S.J., Pipe C.J., Soulages J., McKinley G.H. (2013) Microfluidic extensional rheometry using a hyperbolic contraction geometry. *Rheologica Acta* 52: 529–546.

Oliveira M.S.N., Pinho F.T., Poole R.J., Oliveira P.J., Alves M.A. (2009) Purely elastic flow asymmetries in flow-focusing devices. *Journal of Non-Newtonian Fluid Mechanics* 160: 31–39.

Oliveira M.S.N., Rodd L.E., McKinley G.H., Alves M.A. (2008) Simulations of extensional flow in microrheometric devices. *Microfluidics and Nanofluidics* 5: 809–826.

Oliveira M.S.N., Pinho F.T., Alves M.A. (2012) Divergent streamlines and free vortices in Newtonian fluid flows in microfluidic flow-focusing devices. *Journal of fluid Mechanics* 711: 171–191.

Perkins T.T, Smith D.E, Chu S. (1997) Single polymer dynamics in an elongational flow. *Science* 27: 2016–2021.

Pipe C.J., McKinley G.H. (2009) Microfluidic rheometry. *Mechanics Research Communications* 36: 110–120.

Puangkird B., Belblidia F., Webster M.F. (2009) Numerical simulation of viscoelastic fluids in cross-slot devices. *Journal of Non-Newtonian Fluid Mechanics* 162: 1–20.

Randall G.C., Doyle P.S. (2005) DNA deformation in electric fields: DNA driven past a cylindrical obstruction. *Macromolecules* 38: 2410–2418.

Randall G.C., Schultz K.M., Doyle P.S. (2006) Methods to electrophoretically stretch DNA: microcontractions, gels, and hybrid gel-microcontraction devices. *Lab on a Chip* 6: 516–525.

Ribes A., Caremoli C. (2007) Salome platform component model for numerical simulation. In: *COMPSAC 07: Proceeding of the 31st Annual International Computer Software and Applications Conference*, 553-564 (IEEE Computer Society, Washington).

Rios L.M., Sahinidis N.V. (2013) Derivative-free optimization: a review of algorithms and comparison of software implementations. *Journal of Global Optimization* 56: 1247–1293.

Roberts C.C., Rao R.R., Loewenberg M., Brooks C.F., Galambos P., *et al.* (2012) Comparison of monodisperse droplet generation in flow-focusing devices with hydrophilic and hydrophobic surfaces. *Lab on a Chip* 12: 1540.

Rocha G.N., Poole R.J., Alves M.A., Oliveira P.J. (2009) On extensibility effects in the cross-slot flow bifurcation. *Journal of Non-Newtonian Fluid Mechanics* 156: 58–69.

Schoonen J.F., Swartjes F.H., Peters G.W., Baaijens F.P., Meijer H.H. (1998) A 3D numerical/experimental study on a stagnation flow of a polyisobutylene solution. *Journal of Non-Newtonian Fluid Mechanics* 79: 529–562.

Schroeder C.M., Babcock H.P., Shaqfeh E.S.G., Chu S. (2003) Observation of polymer conformation hysteresis in extensional flow. *Science* 301: 1515–1519.

Shuttleworth R.R., Elman H.C., Long K.R., Templeton J.A. (2011) Fast solvers for models of ICEO microfluidic flows. *International Journal for Numerical Methods in Fluids* 65: 383–404.

Smith D.E., Chu S. (1998) Response of flexible polymers to a sudden elongational flow. *Science* 281: 1335–1340.

Somasi M., Khomami B., Woo N.J., Hur J.S., Shaqfeh E.S.G. (2002) Brownian dynamics simulations of bead-rod and bead-spring chains: numerical algorithms and coarse-graining issues. *Journal of Non-Newtonian Fluid Mechanics* 108: 227–255.

Song K.S., Kang S.O., Jun S.O., Park H.I., Kee J.D., *et al*. (2012) Aerodynamic design optimization of rear body shapes of a sedan for drag reduction. *International Journal of Automotive Technology* 13: 905−914.

Sousa P.C., Pinho F.T., Oliveira M.S.N., Alves M.A. (2011) Extensional flow of blood analog solutions in microfluidic devices. *Biomicrofluidics* 5: 014108.

Tang J., Doyle P.S. (2007) Electrophoretic stretching of DNA molecules using microscale T-junctions. *Applied Physics Letters* 90: 224103.

Teclemariam N.P., Beck V.A., Shaqfeh E.S.G., Muller S.J. (2007) Dynamics of DNA polymers in post arrays: comparison of single molecule experiments and simulations. *Macromolecules* 40: 3848–3859.

Teh S.Y., Lin R., Hung L.H, Lee A.P. (2008) Droplet microfluidics. *Lab on a Chip* 8: 198–220.

Tovar-Lopez F.J., Rosengarten G., Westein E., Khoshmanesh K., Jackson S.P., *et al.* (2010) A microfluidics device to monitor platelet aggregation dynamics in response to strain rate micro-gradients in flowing blood. *Lab on a Chip* 10: 291–302.

Trahan D.W., Doyle P.S. (2009) Simulation of electrophoretic stretching of DNA in a microcontraction using an obstacle array for conformational preconditioning. *Biomicrofluidics* 3: 012803.

Wang M.D., Yin H., Landick L., Gelles J., Block S.M. (1997) Stretching DNA with optical tweezers. *Biophysical Journal* 72: 1335–1346.

White F.M. (2006) Viscous fluid flow. 3rd edition. McGraw-Hill.

Wong P.K., Lee H.K., Ho C.M. (2003) Deformation of DNA molecules by hydrodynamic focusing. *Journal of Fluid Mechanics* 497: 55–65.

Yaginuma T., Oliveira M.S.N., Lima R., Ishikawa T., Yamaguchi T. (2013) Human red blood cell behavior under homogeneous extensional flow in a hyperbolic-shaped microchannel. *Biomicrofluidics* 7: 054110.

Appendices

Appendix A – Additional figures

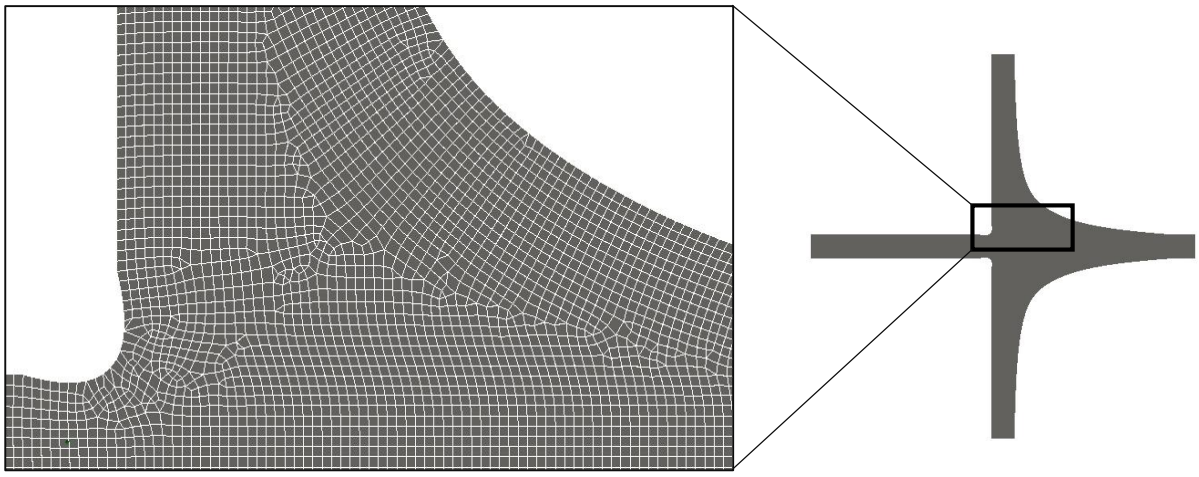

Figure A.1 – Typical mesh used in the optimization routine (2D detailed view of the optimized geometry 3D_AR1_7w).

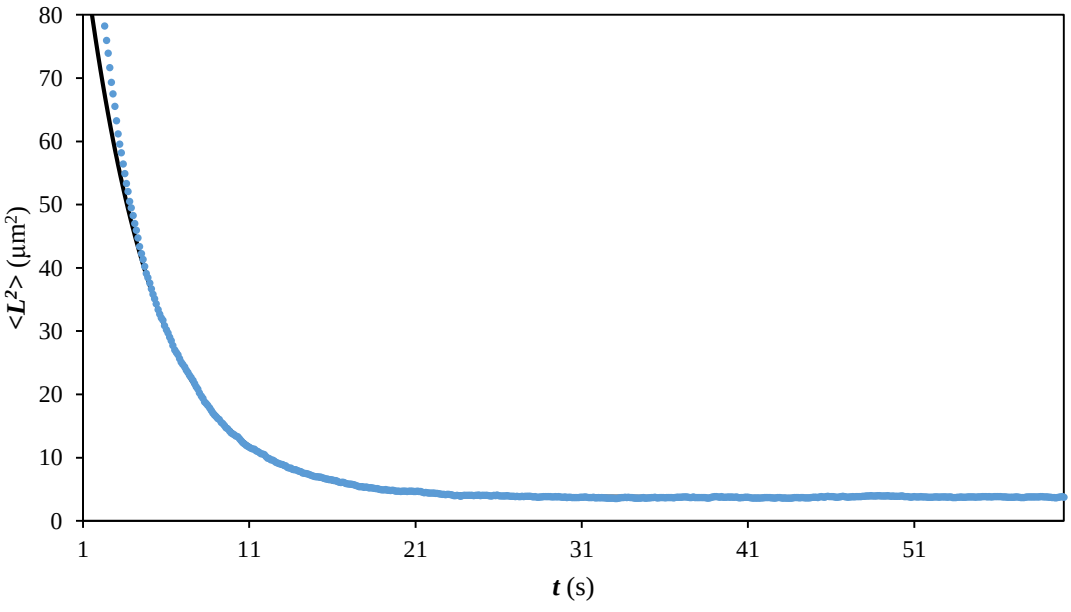

Figure A.2 – Relaxation curve of λ-DNA. The continuous line represents the exponential equation fitted to simulation data (points): $\langle L^2(t) \rangle = 1.94^2 + 110\exp(-t/4.2)$. Only points in the region $L(t) < 6.3$ μm ($0.3L_c$) were considered in the fitting.

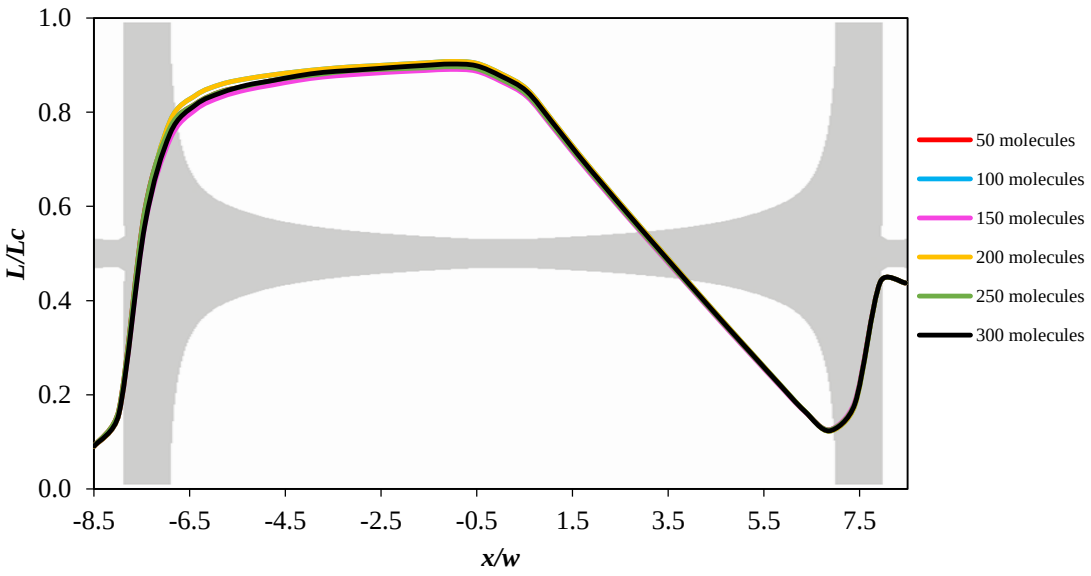

Figure A.3 – Effect of the dimension of the sampled population in the average fractional length of λ-DNA (double 3D_AR1_7w geometry, *We* = 50, *VR* = 100).

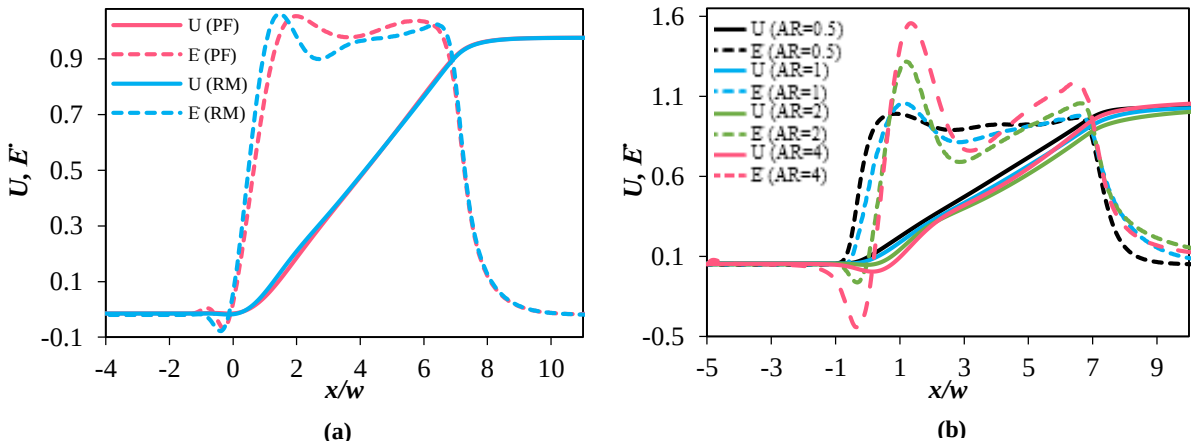

Figure A.4 – Normalized velocity and deformation rate along the centerline of the FFD ($y = 0$, $z = h/2$) for *Re* = 50 and *VR* = 100: (a) 2D geometries (PF – profile fit solution; RM – residuals minimization solution, optimized at *VR* = 100), (b) 3D geometries ($l = 7w$ in all cases, only the aspect ratio changes).

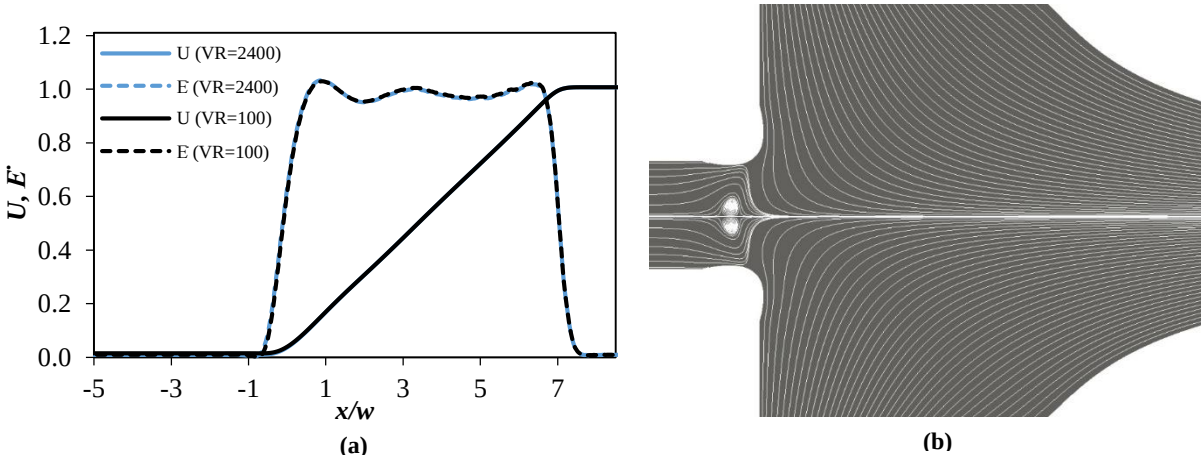

Figure A.5 – (a) Normalized velocity and deformation rate along the centerline of the FFD ($y = 0$, $z = h/2$) at *Re* = 0.4 for different *VR* and (b) corresponding streamlines at *VR* = 2400 (2D_7w geometry optimized at *VR* = 100 through the residuals minimization).

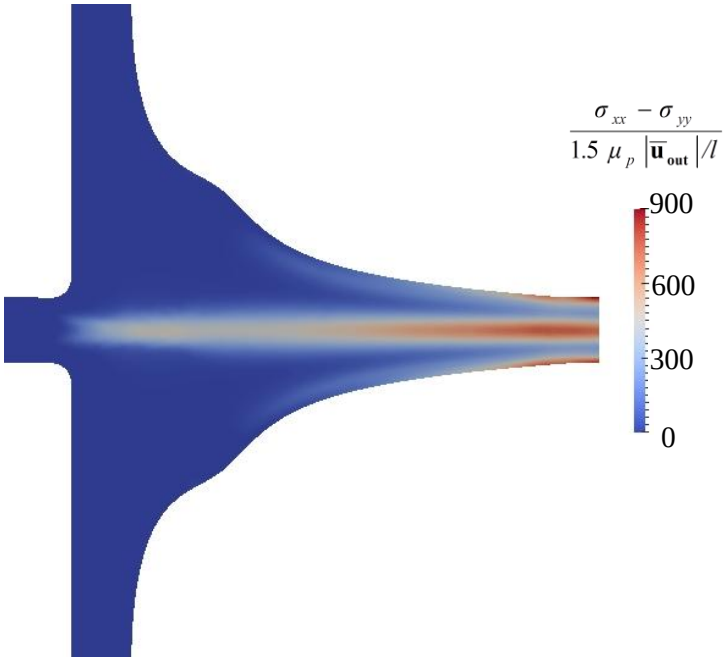

Figure A.6 – Contour plot of the normalized first normal stress difference in the 2D_7w optimized FFD, at *Re* = 0.18, *VR* = 100 and *We* =1.7 for the Oldroyd-B model with β = 8/9.

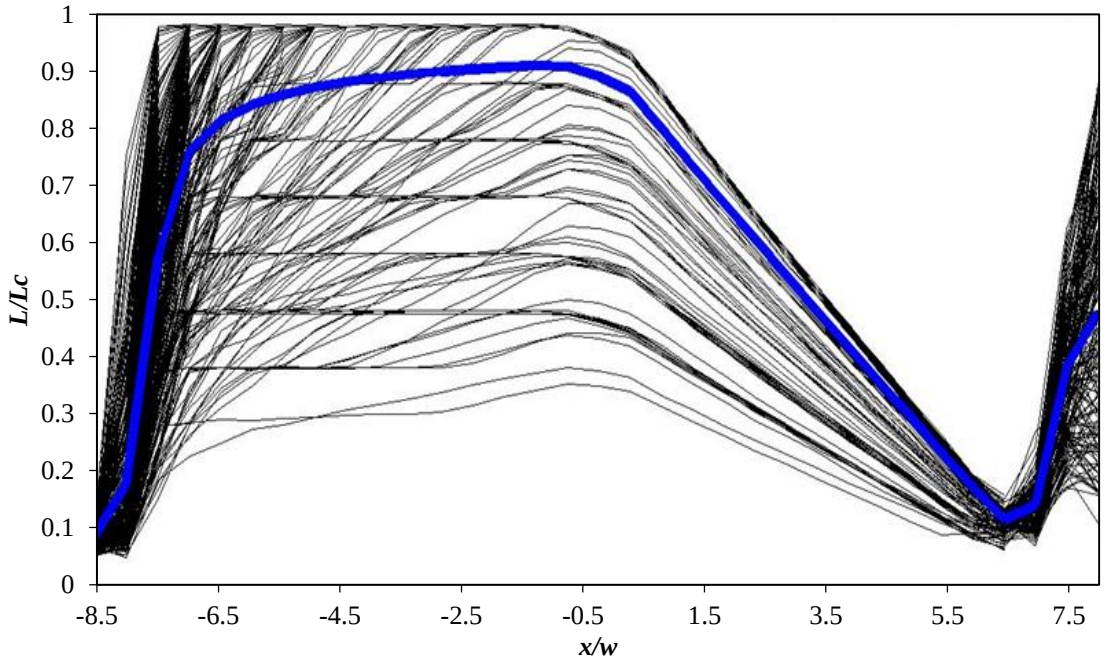

Figure A.7 – Individual (black lines) and averaged fractional length (blue line) of λ-DNA (double 3D_AR1_7w geometry, *We* = 150, *VR* = 100).

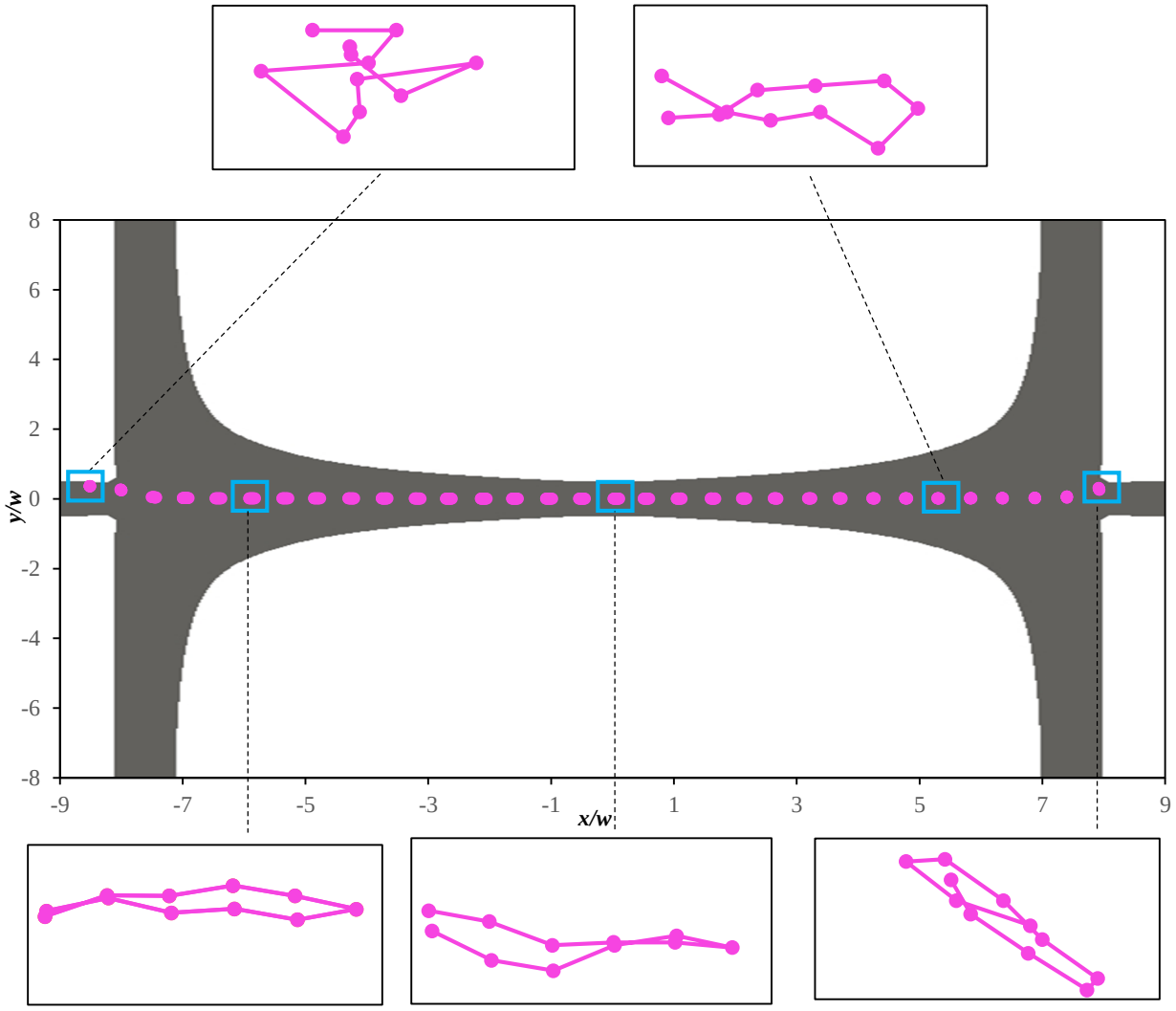

Figure A.8 – Molecular configurations of λ-DNA when the simulation starts from a folded initial configuration (double 3D_AR1_7w geometry, *We* = 50, *VR* = 100). Note that the five molecular conformations illustrated are not drawn to scale with respect to each other.

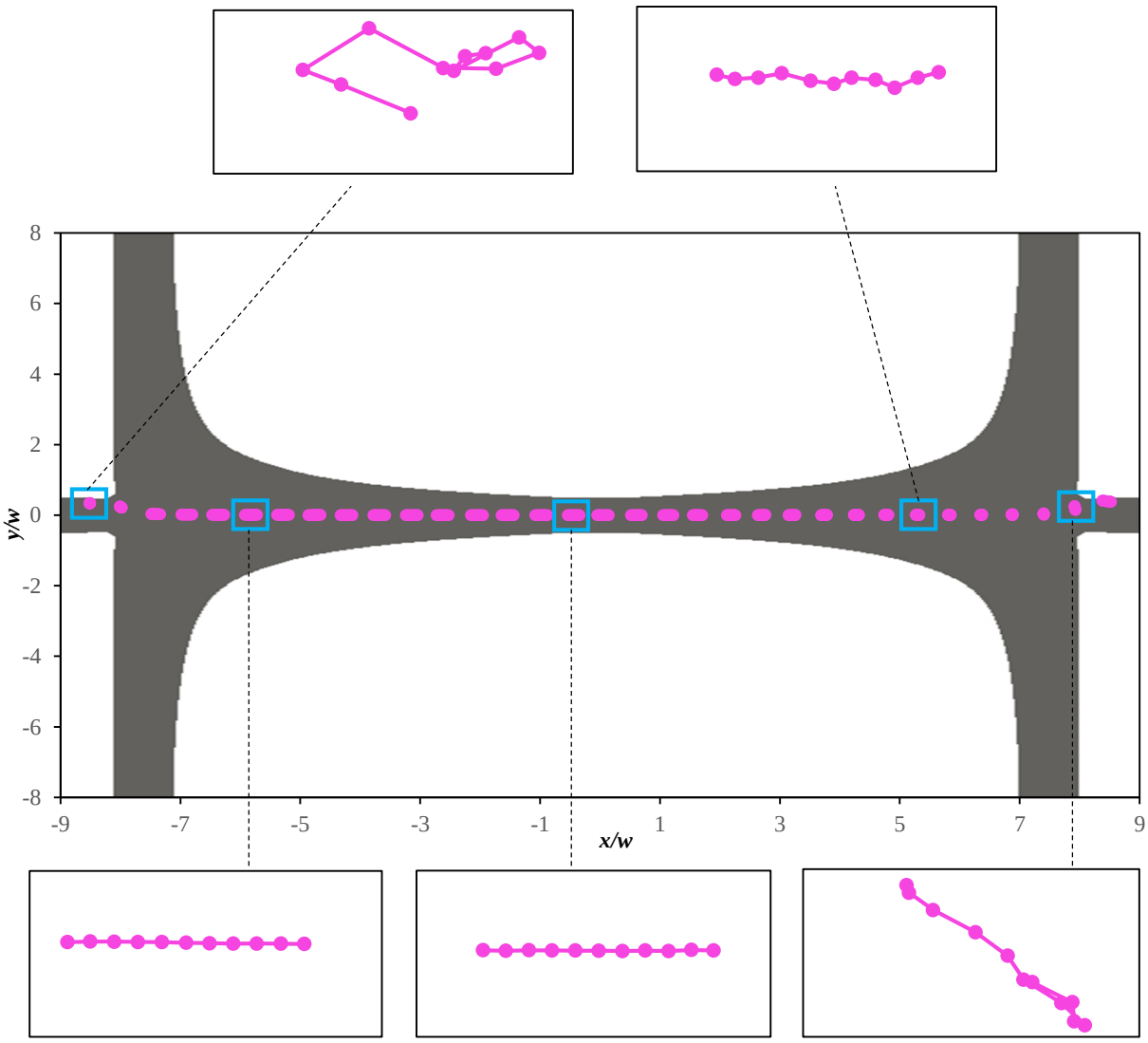

Figure A.9 – Molecular configurations of λ-DNA when the simulation starts from a dumbbell-prone initial configuration (double 3D_AR1_7w geometry, *We* = 50, *VR* = 100). Note that the five molecular conformations illustrated are not drawn to scale with respect to each other.

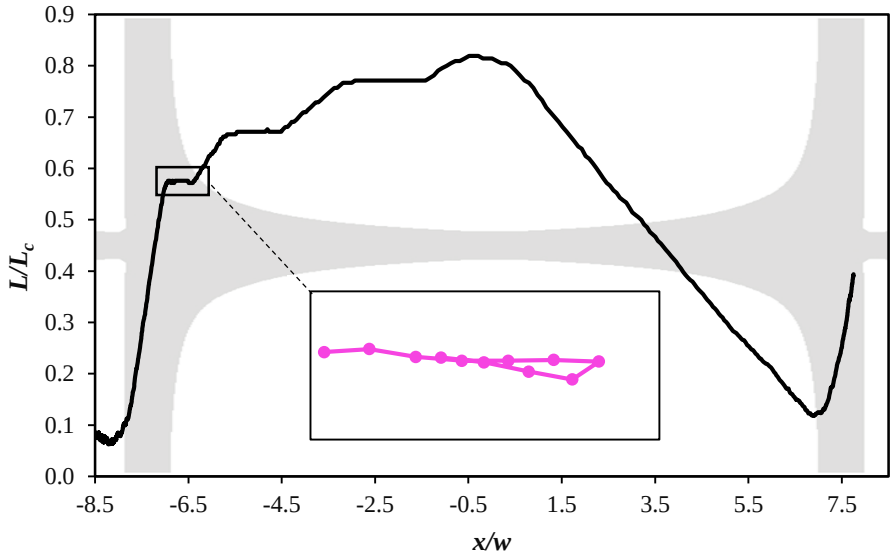

Figure A.10 – Evolution of the fractional length of a λ-DNA molecule in a starting folded configuration being visible three intermediate plateaus that correspond to the unfolding process (double 3D_AR1_7w geometry, *We* = 50, *VR* = 100). The inset shows the molecule conformation in its folded state.

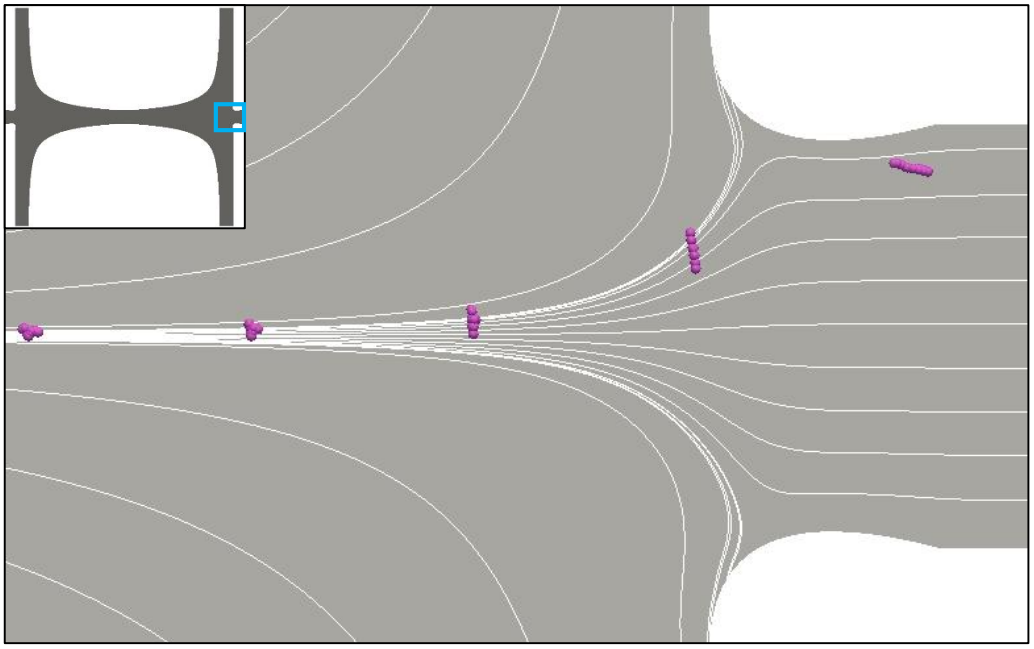

Figure A.11 – Orientation inversion and stretching in the *y*-direction (double 3D_AR1_7w geometry, *We* = 50, *VR* = 100). The position in the device to which the zoomed view refers is identified in the top-left inset.

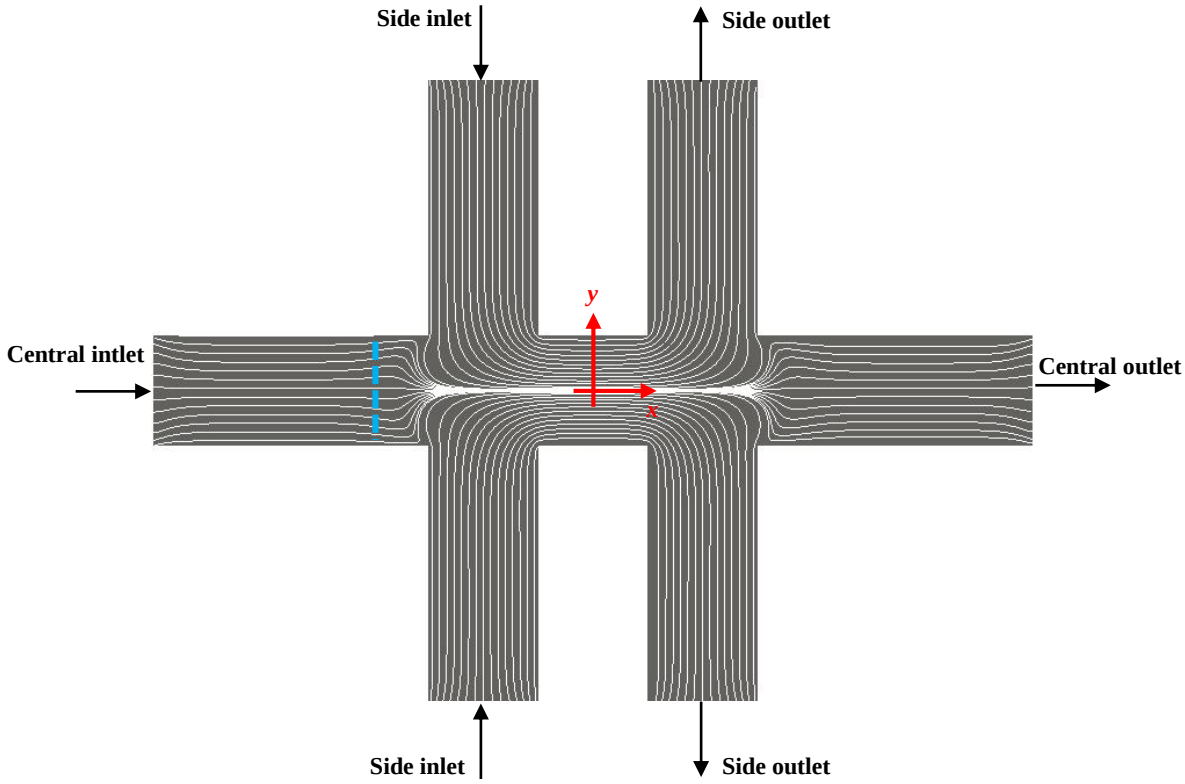

Figure A.12 – Top view of the standard double FFD used in Brownian dynamics simulations (for comparison purposes) and flow streamlines computed in OpenFOAM. The blue dashed line is located at $x/w = -2$ and represents the departure position of molecules. All the arms of the device have the same width, which was made equal to the value used in the optimized FFD.

Appendix B – Analytical solution for estimating the optimal shape of the FFD

In this section, an analytical equation for the channel shape (width) is derived keeping as objective the establishment of a region of constant deformation rate, in a FFD.

If a constant deformation rate is desired at the centerline of the channel – between the upstream position $x_0 = w/2$ and the downstream position $x_l = l$ (see Figure 2.2) –, then it follows from the definition of the deformation rate:

$$\dot{\varepsilon}_{xx} = \frac{du_{x,cl}}{dx} = m \Rightarrow u_{x,cl} = m\left(x - x_0\right) + u_{x0,cl} \tag{B.1}$$

where m is here defined as a fixed value imposed by the channel geometry and by flow conditions (it corresponds to the slope of the velocity profile in the linear region):

$$m = \frac{2K(x = l)\left|\mathbf{u}_{in,side}\right|}{l} \tag{B.2}$$

In the previous equation, K is a constant (evaluated at $x = l$; for the simplicity of notation, $K(x = l) = K_l$) that correlates the average channel velocity with the velocity at the centerline (it varies between $K = 3/2$ for a two-dimensional channel and $K \approx 2.096$ for a duct with square cross-section) and that could be derived from the Navier-Stokes equations. Indeed, the fully-developed velocity profile in a rectangular duct for an incompressible flow is (White, 2006):

$$u_x(y,z) = \frac{4h^2\Delta p}{\pi^3 \mu l} \sum_{n=1,3,5,\ldots}^{\infty} \frac{1}{n^3}\left[1 - \frac{\cosh\left(n\pi\frac{y}{h}\right)}{\cosh\left(n\pi\frac{w}{2h}\right)}\right]\sin\left(n\pi\frac{z}{h}\right) \tag{B.3}$$

Integrating Eq. (B.3) over the rectangular cross-section of a channel, an expression for the flow rate is obtained:

$$Q = \int_0^w \int_0^h u_x dy dz = \frac{h^4 \Delta p}{12\mu l \frac{h}{w}}\left[1 - \sum_{n=1,3,5,\ldots}^{\infty} \frac{192}{(n\pi)^5}\frac{h}{w}\tanh\left(n\pi\frac{w}{2h}\right)\right] \tag{B.4}$$

The ratio between the velocity at the centerline and the average velocity, K, is:

$$K(x) = \frac{u_x(0, h/2)}{\bar{u}_x} = \frac{48}{\pi^3} \frac{\sum_{n=1,3,5,\ldots}^{\infty} \frac{1}{n^3} \left[1 - \frac{1}{\cosh\left(n\pi \frac{1}{2AR} \right)} \right] \sin\left(\frac{n\pi}{2} \right)}{\left[1 - \sum_{n=1,3,5,\ldots}^{\infty} \frac{192}{(n\pi)^5} AR \tanh\left(n\pi \frac{1}{2AR} \right) \right]} \tag{B.5}$$

Note that the dependence of K on the x-position in Eq. (B.5) is present in the AR parameter. Returning to Eq. (B.1), the velocity at the centerline of the channel is now expressed as a function of the average velocity, which leads to an equation for the channel width:

$$u_{x,cl} = K(x)\bar{u}_x = \frac{K(x)Q}{hw(x)} = m\left(x - x_0\right) + \frac{K_0 Q}{hw_0} \Leftrightarrow w(x) = \frac{K(x)Q}{h\left(\frac{K_0 Q}{hw_0} + m\left(x - x_0\right) \right)} \tag{B.6}$$

Introducing Eq. (B.5) in Eq. (B.6) and taking into account that $|\boldsymbol{u}_{in,\,side}|$ is the average velocity in the side channels and also that the flow rate at any position $x > x_0$ is: $Q = hw_{side}\,|\boldsymbol{u}_{in,\,side}|(2 + 1/VR)$ – for a FFD whose arms have all the same width –, then the equation for the channel width as a function of the x-coordinate becomes:

$$w(x) = \frac{K(x)}{h\left(\frac{K_0}{w_0} + \frac{K_l(x - x_0)}{w_{side} l \left(1 + \frac{1}{2VR} \right)} \right)} \tag{B.7}$$

Since $K(x)$ is itself a function of the channel width (Eq. B.5), actually the previous equation is an implicit solution for the channel width and can be solved easily using an adequate iterative method.